DEFORMATION STYLES AND RATES ALONG THE NORTH ANATOLIAN FAULT ZONE IN THE SEA OF MARMARA BASED ON ONSHORE-OFFSHORE SEISMIC, GEODETIC AND GEOLOGIC DATA

by
Zeynep Coşkun
B.S., Geophysical Engineering, Sakarya University, 2006
M.S., Geophysics, Boğaziçi University, 2010

Submitted to Kandilli Observatory and Earthquake Research Institute
in partial fulfillment of the requirements for the degree of
Doctor of Philosophy

Graduate Program in Earthquake Engineering
Boğaziçi University
2021

ACKNOWLEDGEMENTS

I would like to express my deepest appreciation to my supervisor, Prof. Ali Pınar, for his invaluable encouragement, support and guidance during my doctoral studies. I would like to thank him for his understanding over these past seven years and also thank him for pushing my limits which makes me stronger. I would also like to thank the committee members: Prof. Sinan Akkar, Prof. Eşref Yalçınkaya, Prof. Şerif Barış and Assoc Prof. Gülüm Tanırcan for their insightful comments to improve my research study.

I would like to thank all faculty members in the Department of Earthquake Engineering for their support and guidance.

Of course I would like to thank my dear friends for their support and ideas. We overcome the difficulties and share great years together.

Most importantly, none of this could have happened without my family. I owe my deepest gratitude to my parents; I have no words to express how much I owe to my dad Halil Coşkun, my mom Ayten Coşkun and my dear sister İpek Coşkun. Thank you.

ABSTRACT

DEFORMATION STYLES AND RATES ALONG THE NORTH ANATOLIAN FAULT IN THE SEA OF MARMARA BASED ON ONSHORE-OFFSHORE SEISMIC, GEODETIC AND GEOLOGIC DATA

The aim of the thesis is to make a contribution on the long lasting debate on complex fault geometry along the northern branch of the NAF beneath the Sea of Marmara, using seismological, geodetic and geologic data. The focal mechanisms of: (1) small to moderate size events are obtained by CMT inversion technique of Kuge (2003), using onshore waveform data from 2002-2015, (2) micro-earthquakes are obtained using technique of Horiuchi (2015), using offshore waveform data recorded by 15 OBS stations from 2015-2016. The geodetic horizontal crustal strain rates are determined at equally spaced grid points by interpolating northing and easting components of the 112 GPS vectors from 1994-2013. The strain $\dot{\varepsilon}$ and moment rates $\dot{M}$ are calculated by Kostrov's (1974) summation method later modified by Ward (1994). The results indicate that extensional and strike-slip style dominates the region, while compression features are rare. Significant elongation is observed in Çınarcık Basin (CB) and the area between Marmara Island and Central Basin (CeB). Compressional or transpressional features is derived to the west of Marmara Island and Ganos and in the Central segment extending from CeB toward CB. The sparse seismicity beneath the Kumburgaz Basin yields the lowest $\dot{\varepsilon}$ estimated in the region, $11x10^{-8}$/y, supporting the idea that this section could be locked and accumulating strain. The $\dot{M}$ estimation results for each segment show that $\dot{M}_{\mathrm{seis}}$, calculated for instrumental period, are greatly lower than $\dot{M}_{geod}$ and $\dot{M}_{geol}$. This feature can be interpreted in two ways: (1) action of aseismic strain release (creeping), (2) strain accumulation along fault segments is underway and only small portion of the accumulated seismic energy is released by small magnitude events. $\dot{\varepsilon}_{geod}$ results point out the highest values, $24x10^{-8}$/y, in CB, while the lowest values, $11x10^{-8}$/y, are observed in Central Marmara. The highest $\dot{\varepsilon}$ in both edges of the fault segment in CB can be indicative of steadily creeping fault segment. Vice versa lower strain rates in Central Marmara region suggest that this segment of NAF is locked.

ÖZET

KUZEY ANADOLU FAYININ MARMARA DENİZİ BOYUNCA KARA VE DENİZ TABANLI SİSMİK, JEODEZİK VE JEOLOJİK VERİLERİNE DAYALI DEFORMASYON STİLLERİ VE HIZLARI

Tezin amacı Kuzey Anadolu Fayı'nın Marmara Denizi içerisindeki kuzey kolu boyunca uzanan karmaşık fay geometrisi üzerine yapılan tartışmalara sismolojik, jeodezik ve jeolojik verileri kullanarak katkı sağlamaktır. Odak mekanizmaları: (1) Küçük ve orta büyüklükteki depremler 2002-2015 arasında kara istasyonları tarafından kaydedilen veriler kullanılarak Kuge (2003) ters çözüm yöntemiyle, (2) mikrodepremler 2015-2016 arasında 15 deniz tabanı gözlem istasyonu verileri kullanılarak Horiuchi (2015) tekniği kullanılarak elde edilmiştir. Jeodezik kabuk gerinim hızları, 1994-2013 arasında 112 GPS istasyonu tarafından kaydedilen GPS vektörlerinin kuzey ve doğu bileşenlerinin enterpolasyonu ile elde edilmiştir. Gerinim $\dot{\varepsilon}$ ve moment hızları $\dot{M}$ Kostrov'un (1974) Ward, 1994 tarafından modifiye edilen bağıntısıyla hesaplanmıştır. Sonuçlar, bölgede genişleme ve doğrultu atımlı rejimin hakim olduğu, sıkışma rejiminin ise nadir olduğu, Çınarcık Baseni (CB) ve Marmara Adası ile Orta Basen (CeB) arasındaki alanda kayda değer bir uzama olduğu, Marmara Adası ve Ganos'un batısında ve CeB'den CB'ye doğru uzanan Orta segmentte sıkıştırma veya transpressyonel özellikler olduğu gözlenmiştir. Kumburgaz Baseninde gözlemlenen seyrek sismisite bölgedeki en düşük $\dot{\varepsilon}$ değerini, $11\mathrm{x}10^{-8}$/y, vermiş olup, bu segmentin kilitli olabileceği ve dolayısıyla gerinim biriktirebileceği fikrini desteklemektedir. Aletsel dönem için hesaplanan $\dot{M}_{\mathrm{seis}}$, $\dot{M}_{geod}$ ve $\dot{M}_{geol}$'e göre çok düşük değerler vermiştir. Bu sonuçlar iki şekilde yorumlanabilir: (1) asismik yüzey kayması, (2) fay boyunca gerinimin birikmeye devam ettiği, sismik enerjinin ise sadece küçük bir kısmının küçük büyüklükteki depremlerle açığa çıkması. Jeodezik gerinim hızları CB'de en yüksek değerleri, $24\mathrm{x}10^{-8}$/y, işaret etmiş olup, en düşük değerler, $11\mathrm{x}10^{-8}$/y, Orta Marmara'da görülmüştür. CB'deki fay segmentinin her iki ucundaki yüksek gerinim hızları, bu segmentin durağan bir şekilde kaymakta olduğunu, bunun tersine, Orta Marmara'daki düşük gerinim hızları, KAF'ın bu segmentinin kilitli olduğunu düşündürmektedir.

TABLE OF CONTENTS

LIST OF FIGURES

LIST OF TABLES

LIST OF SYMBOLS

d	Data vector
D_s	Smoothing spatial moment release matrix
D_t	Smoothing temporal change matrix
$G_{np,q}$	Green's function
H_s	Seismogenic thickness
L	Distance
M_0	Seismic moment
M_{pq}	Force couple
Mw	Moment magnitude
mij	Unit moment tensor
P_m	Unit vector for pressure axes
T	Catalogue duration
T_m	Unit vector for tension axes
u	Displacement
V	Volume
$\acute{\varepsilon}ij$	Strain rate
λ	Weight
μ	Rigidity
σ	Stress
τ	Duration
τ_{xy}	Shear stress in the fault plane
θ_p	Inclination angle
ϕ_p	Azimuth angle
ω_p	Rotation angle
ϕ	Strike
δ	Dip
λ	Rake

LIST OF ACRONYMS / ABBREVIATIONS

3-D	Three Dimensional
CB	Cinarcik Basin
CeB	Central Basin
CH	Central High
CMT	Centroid Moment Tensor
GPS	Global Positioning System
Hz	Hertz
JAMSTEC	Japan Agency for Marine-Earth Science and Technology
KB	Kumburgaz Basin
Km	Kilometer
KOERI	Kandilli Observatory and Earthquake Research Institute
M	Magnitude
MARDIM	Earthquake and Tsunami Disaster Mitigation in the Marmara Region and Disaster Education in Turkey
MMF	Main Marmara Fault
Ms	Surface Wave Magnitude
Mw	Moment Magnitude
NAF	North Anatolian Fault
NAFZ	North Anatolian Fault Zone
OBS	Ocean Bottom Seismographs
RETMC	Regional Earthquake-Tsunami Monitoring Center
TB	Tekirdag Basin
WH	Western High

1. INTRODUCTION

The North Anatolian Fault (NAF) is one of the largest and seismically active strike-slip faults in the world. During the 20th century NAF has produced a sequence of major devastating earthquakes that causes serious damages and loss of lives. Starting with 1912 Ganos earthquake in the west and then followed by 1939 Erzincan earthquake in the eastern Anatolia, the large events systematically propagate westward toward İstanbul-Marmara region. Especially after two catastrophic earthquakes, Mw7.4 August 1999 Kocaeli and Mw7.1 November 1999 Duzce, that caused 18.373 accounted deaths, 48.901 injuries, 16.400 heavily damaged-collapsed buildings, and 600.000 homeless people (Erdik, 2000), has led to great interest in NAF.

After Mw7.4 Kocaeli earthquake, a seismic gap, lies between the 1912 Ganos and 1999 Kocaeli ruptures, occurs along the NAF in the Sea of Marmara. The Marmara Sea region is highly populated and fast developing region of Turkey. Especially, the city of Istanbul with more than 15 million people, economic activities, Turkish industry, historical and cultural heritage is highly under a devastating earthquake threat. According to the historical data, in the period between A.D. 1500 and 1900, six M>7 earthquake in 1509, 1719, 1754, May 1766 and August 1766 have occurred within the Sea of Marmara (Ambraseys and Finkel, 1990, 1991, 1995). The reevaluation of historical data by Ambraseys and Jackson (2000) states that the northern shore of the Sea of Marmara between Tekirdağ and Silivri has not been ruptured since 1500. This interpretation is in contrast with the general opinion that 1766 events are the last ones that rupture the whole Main Marmara Fault (MMF) (Hubert-Ferrari et al., 2000, Fraser et al., 2010, Meghraoui et al., 2012, Drab et al., 2015). In any case, there is at least 100 km gap between the two ruptures (Le Pichon et al., 2003).

A great amount of geophysical, geological and geotechnical studies have been carried out in order to characterize the NAF in the Sea of Marmara (See Chapter 2). In order to identify the potential of future expected earthquake in the Sea of Marmara, fault geometry, fault segmentation and seismic activity along the MMF has been studied by several Ocean Bottom Seismograph (OBS) observations (Sato et al., 2004, Tary et al., 2011, Cros and Geli, 2013, Schmittbuhl et al., 2015, Yamamoto et al., 2015, Bohnhoff et al., 2016). However, the duration of observation periods and the extent of observation area are key factors for interpretation of the fault geometry and seismic activity beneath the Sea of Marmara.

In this study, fault geometry, fault segmentation and the seismic activity in the Sea of Marmara are investigated using two different data sets recorded by land seismic stations covering the period between 2002 and 2015, and OBS covering the period between September 2014 and June 2016. Focal mechanisms of small to moderate size events recorded by land seismic stations are determined using Centroid Moment Tensor (CMT) inversion method. For the events recorded by OBS's, the P-wave polarity data is used for the simultaneous determination of stress tensor parameters and fault plane solutions for many earthquakes.

Earthquake catalogues have great importance in seismological studies. They provide an extensive database that is useful for various studies related to seismotectonics, seismicity, earthquake physics and seismic hazard analysis. Since the national and international catalogs only cover the source mechanism solutions of important moderate to large earthquakes, the seismological study carried out in this period for Marmara region has filled a gap in terms of providing source parameters and uniform magnitude unit for all events, besides enables fault characterization in the region.

The scope of the first part of this study is the dissemination of the scientific findings on creating a very detailed moment magnitude earthquake catalog denoting the source parameters of earthquakes with magnitudes larger than 2.7 that occurred in Marmara region. Moreover, with the integration of OBS analysis, precise hypocenter locations of earthquakes are calculated during the observation period and combine the result with CMT analysis with the moment tensor inversion of earthquakes in the Sea of Marmara with an aim to understand better the fault segmentation and fault geometry of the North Anatolian Fault crossing the Sea of Marmara.

The complex fault geometry along the northern branch of the North Anatolian Fault beneath the Sea of Marmara have been under debate for the past few decades. The main aim of the thesis is to make a contribution on the long lasting debate using seismological, geodetic and geologic data. The relevant data are utilized to determine the seismic, geodetic and geologic moment rates.

This study consists of two parts. In Chapter 2, compressional and extensional features along major strike-slip faults around the world, along NAF and in Marmara are introduced.

The first part, namely Data Accumulation, consist of Chapter 3, Chapter 4 and Chapter 5. In Chapter 3, data set and methods are introduced for the estimation of focal mechanism. In subsections of Chapter 3, data processing procedure, selection of earthquakes appropriate for the analysis, theory and determination of focal mechanism prodecure are explained for both CMT and Simultaneous Inversion of First Motion Polarity Data approaches. In Chapter 4, the results of the analyses are given. The main findings for each segment of the NAF in the Sea of Marmara are given in the subsections of this chapter in detail. Chapter 5 gives a summary of the highlights of the first part and relates them to the general tectonic background.

The second part, namely Data Interpretation, consist of Chapter 6 and Chapter 7. In Chapter 6, methods are introduced for the estimation of representative moment tensors, stress tensor inversion, seismic strain rate and moment rate, geodetic strain rate and moment rate, geologic strain rate and moment rate. The results of the analysis are given in subsections. Chapter 7 give a summary of the highlights of the study, relate them to the general tectonic background and outline the final concluding remark.

1.1. Motivation of the Study

The North Anatolian Fault (NAF) extends from Karlıova triple junction to Aegean Sea for about 1500 km. It extends from Karlıova to Mudurnu Valley as a narrow fault trace. Then enters the Marmara region where it splits into branches. The northern branch crosses the Gulf of İzmit, Çınarcık Basin and follows the northern shelf of the Sea of Marmara and continues from Gulf of Saros toward Aegean and mainland Greece (Barka, 1992, Yaltirak et al., 2000, Görür et al., 1997, Tüysüz et al., 1998, Okay et al., 1999). The southern branch extends from Mudurnu Valley towards İznik, Gemlik Bay and goes along the southern coast of the Sea of Marmara, passes east of the Marmara island and then merges with the northern branch offshore Mürefte. Around İznik Lake, NAF splits again into another branch that goes EW towards Bursa, Manyas, Yenice-Gönen and then continues southwestwards to Gulf of Edremit and then again splits into branches extending in SW direction in the Aegean Sea. Although the major earthquakes taking place along NAF show predominantly strike-slip faulting, several moderate size earthquakes reveal normal faulting and reverse faulting mechanisms associated with transtensional and transpressional features developed along NAF. Noticeable examples of normal faulting are the 1935 Marmara Island (Mw=6.4), 1964 Karacabey-Manyas earthquake (Mw=6.9) and 1963 Çınarcık earthquake (Mw=6.3). Earthquake on the transpressional features are 1983 Biga earthquake (Mw=6.1), 2019 Offshore Silivri earthquake (Mw=5.7).

In this study, focal mechanisms of small size NAF earthquakes have been derived and used as a tool to identify the transtensional and transpressional features. Furthermore, GPS data has been processed to determine the style of faulting and strain rates. Then, the seismically and geodetically determined strain rates have been compared to identify the seismic potential of the transpressional and transtentional features. Furthermore, seismic moment rates for instrumental period and historical period, geodetic moment rates and geologic moment rates have been estimated which provides input for hazard and risk assessment studies.

2. COMPRESSIONAL AND EXTENSIONAL FEAUTURES ALONG MAJOR STRIKE-SLIP FAULTS

The compressional and extensional feautures along major strike-slip faults in the world and along the North Anatolian Fault are briefly introduced in this chapter.

2.1. Compressional and extensional features along major strike-slip faults

Strike-slip faults are one of the remarkable tectonic features that form as a kinematic consequence of large-scale plate motions. Strike slip faulting form both in continental and oceanic transform plate boundaries at a wide range of scales (Wilson, 1965, Cunningham and Mann, 2007). Strike slip systems are relatively narrow and more continuous rather than compression and extension systems. Ideal pure strike-slip fault zones, a perfectly planar, cause neither extension nor shortening of the crust. However long major strike-slip faults are complex domains associated with many secondary compressional and extensional structures. The secondary structures commonly form en échelon faults separated by step-overs (MIT lecture notes, 2005). The geometry of step-overs and linking faults controls restraining (compressional) and releasing (extensional) bends with respect to stepping and slip direction of en échelon fault segments (ETHZ lecture notes, 2017).

Restraining bends are sites of convergence where the material is pushed together that result in crustal thickening and surface uplift. Denali Range in Alaska, Santa Cruz Mountains in California, the Lebanon Range in Middle East, Karlik Tagh Range in China are some examples of known restraining bends in the world (Cunningham and Mann, 2007, Gudmundsdottir et al., 2013).

Releasing bends are sites of extension where the material is pulled apart that result in crustal thinning and basin formation. Pull-apart basins are produced by local deformation near releasing bends in strike-slip faults. Dead Sea, Death Valley, Gulf of

California, Gulf of Aqaba are some examples of known releasing bends in the world (Christie-Blick & Biddle 1985, Persaud et al. 2003, Cunningham and Mann, 2007).

Flower structures are another product of compressional and extensional feautures of strike-slip faults. The thrust and normal faults associated with the releasing or restraining bends merge into main strike slip fault in deep (MIT lecture notes, 2005). These structures are called flower structıres. Double restraining bends commonly define positive flower structures where rocks are faulted upward. Double releasing bends commonly define negative flower structures where rocks drop down (Cunningham and Mann, 2007). The Oca Fault in Venezuela (Rod, 1956), Mecca Hills in California (Sylvester and Smith, 1976) and South China Sea (Roberts, 1983) are some examples where positive flower structures are recognized (Harding, 1985). Andaman Sea in Southeast Asia (Harding, 1983) and Cottage Grove Fault Zone in Illinois (Nelson and Krausse, 1981) are some examples where negative flower structures are recognized (Harding, 1985).

2.2. Compressional and extensional features along NAF

The North Anatolian Fault, extending over 1600 km between Karlıova triple junction to the Gulf of Saros in the northern Aegean Sea, is one of the largest active dextral strike-slip fault forming the plate boundary between Eurasia and Anatolia. Although the NAF has mostly single geometry along its entire length, important secondary compressional and extensional structures are observed associated with major bends or step-overs along the fault trace (Hubert-Ferrari et al., 2002).

Main basins formed along the NAF related to the activity of North Anatolian Shear Zone. The Erzincan, Kazova, Suşehri, Niksar, Taşova-Erbaa, Havza-Ladik, Tosya, Çerkeş-Kurşunlu, Yeniçağa, Bolu, Düzce, Adapazarı, Gölcük-Derince, Yalova, and the Sea of Marmara basins are developed on the main strand of the NAFZ.

The Erzincan and Erbaa basins are the two main releasing step-overs in the eastern part of NAF. Erzincan Basin is the major discontinuity along NAF in the east which have complex fault geometry. Two main left stepping segments with same strike enter the NW-SE directed Erzincan pull-apart basin and they are linked by a 100 km long fault segment.

The left-lateral Ovacık Fault to the south of the basin also contributes the extension in the SW part of the basin (Hubert-Ferrari et al., 2002). The Erbaa pull-apart basin is formed by a 10 km long releasing step between same striking two linear fault segments. The 1939 M 7.6 Erzincan earthquake is diverted from the NAF system to the south from Erbaa basin to Ezinepazarı fault and continued to rupture. This secondary Ezinepazarı fault located between Esençay Fault in the north and Almus Fault in the south form together horsetail structure south of Erbaa Basin (Şengör and Barka, 1992; Tartar et al., 1995; Barka, 1996; Bozkurt and Koçyiğit, 1996).

The 50 km long mostly E-W trending Almus Fault Zone (AFZ) is one of the major splays of the NAFZ (Bozkurt and Koçyiğit, 1995; Bozkurt and Koçyiğit, 1996). AFZ have a right lateral strike-slip character having thrusting in several places. Mercimekdagi-Camdere and Tokat fault sets are the strands of the AFZ. The 0.7 – 10 km wide and 60 km long Kazova Basin, located between Mercimekdagi-Camdere and Tokat fault sets, is an example of an active negative flower structure in the region (Bozkurt and Koçyiğit, 1996). The 30 km long and 10-15 km wide Merzifon Basin located on the Hamamözü Fault Zone which is a splay fault from the main strand of the NAF, is another example of a pull-apart basin (Şengör et al., 2005).

The Suşehri Basin has a transtensional pull-apart feature. In Suşehri Basin although the dominant stress regime is strike-slip that have formed under NW-SE directed transtension, normal faults and oblique-slip faults that are formed under an extensional regime with NNE-SSW direction are also observed (Polat et al., 2012).

The Niksar basin is closely linked to the Taşova-Erbaa basin and has a narrow connection. The Niksar basin is formed at a major releasing step of between the 1939 and 1942 earthquke rupture segments of the NAFZ. The Taşova-Erbaa pull-apart basin is located at the releasing step-over formed by the rupture segments of the 1942 earthquake in the east, 1943 earthquake in the north and Esençay Fault in the south (Barka et al., 2000).

The Havza-Ladik Basin is a double basin separated by north-south striking normal faults located approximately 5 km west of Ladik. The Havza part is bounded by the main strand of the oblique-seperation right lateral strikes-slip of NAF with a minor thrusting.

The Ladik part of the basin is narrower and combitaion of a flexural basin and fault wedge basin. The normal faulting along the southern margin (Öztürk, 1980) of the basin is replaced by strike-slip faults indicating shortening across the basin (Şengör et al., 2005).

The Tosya Basin is located at the southern part of NAF. The main trace of the NAFZ changes direction north of Tosya and forms a restraining bend (Barka, 1992). The basin is bounded by two oblique thrust faults and has similar character to the Çerkeş-Kurşunlu Basin (Şengör et al., 2005).

The Çerkeş-Kurşunlu Basin is an ENE-trending obliquely shortening basin that located at the southern part of main NAF trace. The northern and southern sides of the basin is bounded by oblique-thrust faults (Bellier et al., 1997)

The Bolu Basin is a pull-apart basin formed under the influence of dextral strike-slip faults assicated with the NAFZ. The northern boundaryof the basin is controlled by a normal fault with a right-lateral strike slip component. In the northwest of the Bolu Basin, thrust faults are also observed along a short restraining bend of the boundary. The southern boundary of the basin is controlled by the main strand of NAFZ. Positive flower structures are also observed in the region formed by the restraining character of the main strand of of NAFZ (Gökten et al., 2011).

The Düzce Basin is controlled by NE-SW striking right-lateral offsets to the east and NW-SE striking normal faults to the west. The Basin is bounded by the Düzce Fault to the south and the Çilimli Fault to the north (Şengör et al., 2005).

The Adapazarı Basin is a pull-apart basin located to the north of Düzce Fault, is mainly formed by NW-SE striking normal faults and E-NE-SW striking right-lateral oblique faults (Greber, 1997). The basin is situated in a transtensional region between the Mudurnu valley and the İzmit- Adapazarı segments of the NAF (Emre et al., 1998).

The Gölcük-Derince Basin is a sedimentary basin located along the main strand of the NAF. The basin is bounded by a dominantly right-lateral strike-slip fault to the south that turns into a NW-SE striking normal fault west of Gölcük town (Akartuna 1968).

The Yalova Basin is located on the main starnd of the NAF. The basin is an E-W extended basin bounded by EW striking strike-slip fault to the south and NW-SE striking normal faults to the west (Eisenlohr 1997, Alpar and Yaltırak 2002).

2.3. Compressional and extensional features along NAF segments in Marmara

The Sea of Marmara is situated in a transition zone between the dextral strike slip NAF and the extensional Aegean Sea (Dewey & Şengör 1979; Smith et al. 1995). The western part of the NAF diplays a complex character in the Marmara region and splits into several branches before entering the Sea of Marmara.

The southern branch which extends southwest from Bolu splits again in the Pamukova Plain. The northern part extends along İznik Lake, Gemlik Bay and Bandırma Bay. The southern part extends from Bursa to Manyas along south of Ulubat Lake and Manyas Lake, creating Yenişehir pull-apart basin south of İznik Lake (Yaltırak, 2002).

The character of the northern branch of the NAF in the Sea of Marmara is still controversial. The most apparent structures formed in the Sea of Marmara are three deep marine basins, namely, Çınarcık Basin, Central Basin and Tekirdağ Basin from east to west. Numerious studies are conducted in order to understand the fault geometry and marine basin formation in the Marmara Sea. The outcomes of these studies can be classifed into three groups: 1) pull-apart model (Barka and Kadinky-Cade,1988; Barka, 1992; Ergün and Özel, 1995; Wong et al., 1995; Armijo, et al., 1999, 2002), 2) en-echelon fault segment model (Parke et al., 1999; Siyako et al.,2000; Okay et al., 2000, 2004), 3) single throughgoing dextral strike-slip fault model (Le Pichon et al., 1999, 2001, 2014; Aksu et al.,2000; Imren et al., 2001; Demirbağ et al. 2003; Seeber et al., 2004, 2006, 2010; Kurt et al., 2013; Sengor et al., 2014).

Ergün and Özel, 1995; Wong et al., 1995 modified the pull-apart model including the compressional and extensional rhombohedral blocks in order to explain the three deep marine basin formation. The E-W trending normal faults are identified by Smith et al. (1995) proposing that the southern part of Marmara Sea is a half graben. Okay et al. (1999) interpreted that Ganos Mountain is formed by elastic bending associated with NE-SW thrust fault to the east of the Tekirdağ Basin. Parke et al. (1999) suggested that the E-W trending normal faults are responsible for the evolution of the Marmara Sea more than NAFZ in the Marmara region. Le Pichon et al. (1999) interpreted that a buried master fault, namely, the Great Marmara Fault, passes from the southern part of the Çınarcık Basin, along the Central Basin, and extending along the southern part of the Tekirdağ Basin, causing the formation of the basins and highs due to right-lateral shearing forces. Aksu et al. (2000) interpreted that the Marmara Sea can be evolved as a negative flower structure, bounded by two sidewall faults that are linked to a single near-vertical south-dipping master fault. Siyako et al. (2000) proposed that three en-echelon fault segments cross the basins, which are bounded by shallowly dipping normal faults, forming a negative flower structure (Yaltırak, 2002).

3. DATA ACCUMULATION-DATA AND METHODS

The first part of the study is carried out using two different data sets recorded by onshore stations and Ocean Bottom Seismographs (OBS). The former one is obtained from stations operated by Boğaziçi University Kandilli Observatory and Earthquake Research Institute Regional Earthquake-Tsunami Monitoring Center (KOERI-RETMC) covering the period between 2002 and 2015. The latter one is obtained from free-fall pop-up 15 OBS stations deployed by Japan Agency for Marine-Earth Science and Technology (JAMSTEC) along the northern branch of the North Anatolian Fault (NAF) crossing the Marmara Sea covering the period between September 2015 and June 2016.

The data is elaborated using two different data processing software; zSacWin for land data and WIN system for OBS data. Focal mechanisms of events recorded by land seismic stations are determined using Centroid Moment Tensor (CMT) inversion method, where the mechanisms are retrieved individually. For the events recorded by OBS's, the method developed by Horiuchi et al. (1995) is used, where the P-wave polarity data is used for the simultaneous determination of stress tensor parameters and fault plane solutions for many earthquakes.

The detailed information about the data sets, data processing softwares and methods are explained in the subsections of this chapter.

3.1. General - Overview of Determination of Source Mechanism

Elastic waves are generated by an elastic disturbance within or on the surface of an elastic medium. Almost every excitations or sudden deformations in an elastic medium may result in detectible sources. Earthquake faulting, buried explosions, mine bursts, wind, cultural noise, meteorite impacts, volcanic eruptions and landslides are some common seismic sources which are of interest to Seismologist.

Understanding the source mechanisms of earthquakes helps us to better understand the fracturing behavior of reservoirs, determine faults and evolving stress field in earthquake prone regions (Eyre and Van der Baan, 2015) Focal mechanism solutions indicate the geometry of faulting during an earthquake by using seismograms recorded at different distances and azimuth (Stein and Wysession, 2003). There are several methods used to obtain focal mechanism. Using polarity of P-wave first motion and waveform inversion are two common methods used for the calculation of focal mechanisms of earthquakes.

3.1.1. The First Arrival Polarity Method

In this method the focal mechanisms are derived from observing the pattern of first arriving P waves. In different directions, different polarity of first motion P waves are observed as fault slips and both sides of the fault plane moves in opposite directions (Havskov and Ottemoller, 2010) Figure 3.1 illustrates the concept for a strike-slip event on a vertical fault. When the material near the fault moves towards the station the first motion observed in the station is upward first motion corresponding to compression, when the motion is away from the station the first motion observed in the station is downward motion corresponding to dilation.

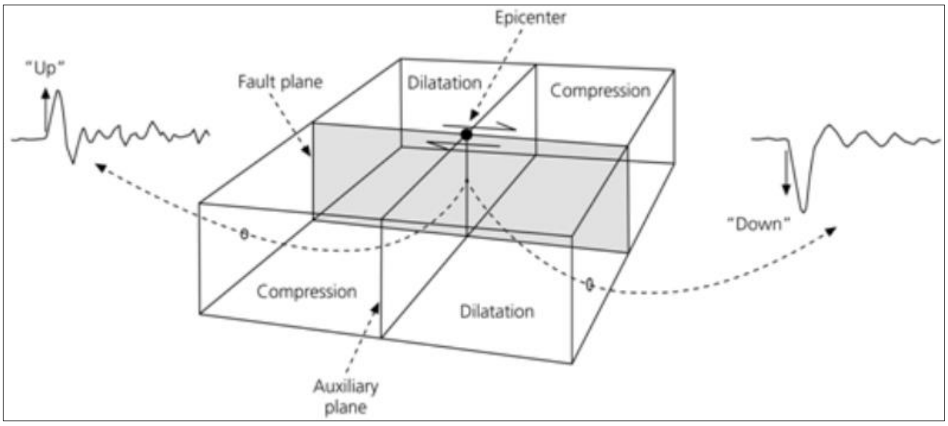

Figure 3.1. Representation of the relation between first motion polarity and fault orientation (Stein and Wysession, 2003).

As shown in Figure 3.1 the division between two compressional and two dilational quadrants occurs along a fault plane and an auxiliary plane which are called nodal planes.

Since the first motions from slip on the actual fault plane and the auxiliary plane would be the same, it is not possible to distinguish the actual fault plane only determining first motions. Additional information such as field observation, smaller aftershocks following an earthquake, and if the earthquake is large enough, directivity effects indicate actual fault planes (Stein and Wysession, 2003).

3.1.2. The Waveform Inversion Method

In waveform inversion method, individual components of earthquake moment tensors are obtained directly from the recorded seismograms. In this method, synthetic seismograms are computed for each component of the moment tensor and the solution is determined by the best-fit between observed and synthetic seismograms. This technique eliminates the difficulty of picking a first motion polarity under noisy conditions (Okal, A., 2011). Information about earthquake depths and rupture process are also obtained from waveform analysis that cannot be extracted from first motions (Kikuchi and Kanamori, 1991).

The recorded waveform data are the combination of both seismic source process and propagation effects. The propagation effects are removed by producing Green's functions. In Green's functions calculations, the velocity structure should accurately be modeled. Green's functions are produced by modelling the propagation of seismic waves between source and receiver locations. Green's functions are described as the displacement responses recorded at the receivers when an impulse force is applied at the source in a viscoelastic earth. The *n*th component of the displacement *u*, recorded at point x and time *t*, can be expressed as,

$$u_n(\mathrm{x}, t) = \mathrm{M}_{pq}(t) * \mathrm{G}_{np,q}(\mathrm{x}, t), \quad n, p, q = x, y, z \tag{3.1}$$

where $\mathrm{M}pq$ is the force couple in *pq* direction, asterisk sign indicates the convolution operation. $\mathrm{G}np,q$ is the spatial derivatives of the nth components of the Green's functions generated by the moment $\mathrm{M}pq$ (Eyre and Baan, 2015).

Since the convolution operation in equation 3.1 becomes a simple multiplication in the frequency domain, the inversion is generally performed in the frequency domain.

The quality of the inversion results is identified by the misfit between observed and calculated data. Moment tensors can also be decomposed into their principal components by the singular value decomposition of the six time-dependent moment-tensor components. In this approach a common source-time function and also its contribution to each component can be estimated. So that it's possible to obtain a source-time history of the source process and its mechanism. The source mechanism is given by the eigenvalues of the scalar moment tensor, and the orientation of the principal axes is given by the eigenvectors (Eyre and Baan, 2015).

3.2. Centroid Moment Tensor Inversion Method

Centroid Moment Tensor (CMT) inversion is a non-linear least squares process that centroid locations and the six components of the moment tensor determined. CMT inversion algorithm was first carried out using long period body and surface waves from worldwide broad-band records of global digital networks. As the number of seismic stations increase at earthquake prone regions, CMT inversion is now also carried out using broad-band data from regional or local seismic networks (Mulargia, F. and Geller, R. J., 2003).

With the improvement of digital broad-band instrumentation, full-wave CMT inversions can be done using regional broad-band waveform data for earthquakes with local magnitude greater than 3.0. In the waveform inversion technique, the best CMT solution is found by minimum waveform misfit between observed and synthetic seismograms. Inversion can be done in time domain or frequency domain (Lee et al., 2011).

In general, focal depth is assumed to be constant in moment tensor inversion approaches. The inversion is performed for a range of focal depths and the optimal solution is selected with the lowest misfit (Bock, G., 2012).

In this study, the faulting parameters of earthquakes occurred in the Sea of Marmara and surroundings are calculated using the technique developed by Kuge (2003). The method consists of three steps. In the first step, point-source moment tensor solution, in the second step, aligned point sources, fault plane and its length, and in the third step moment release distribution on finite fault is determined.

In this method three component displacement waveforms derived from the original acceleration or velocity records are used. The Green's functions are calculated following the method of Koketsu (1985) for a horizontally layered structure.

3.2.1. Data

One of the primary goals of the study is to create an earthquake catalogue of focal mechanisms for Marmara region. For this purpose, a very detailed seismological study is carried out using OBS and broadband land stations in order to derive faulting characteristics in and around the Sea of Marmara and calculate uniform magnitude unit for all events.

Since the lack of mechanism solutions of small events in earthquake catalogues, events with magnitudes larger than 3.0 occured in the study region are analyzed. The coordinates of the study area is selected as Latitude: 40.0 - 41.5˚ N, Longitude: 25.45 – 32.0 E˚.

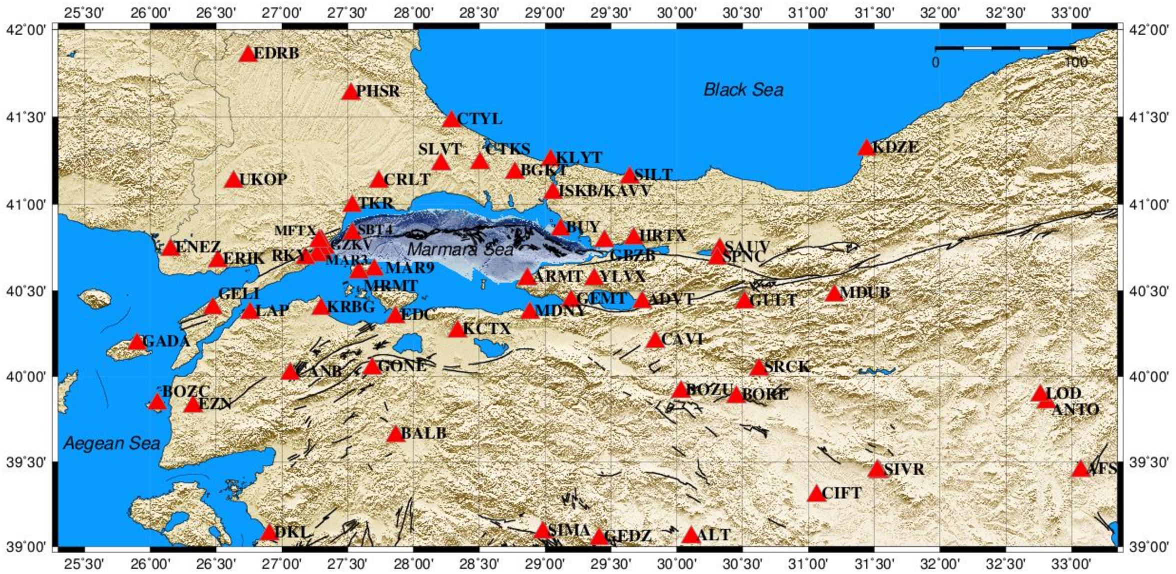

Figure 3.2. Location of broadband stations operated by KOERI-RETMC.

The records of the earthquakes are obtained from the broadband seismic stations operated by KOERI covering the period between 2002 and 2015 (Figure 3.2). The catalog is searched for earthquakes with magnitude equal and larger than 3.0 occurred in and around the Marmara region (Figure 3.3). The histogram in Figure 3.4 shows the number of earthquakes versus magnitude occured in the observation period.

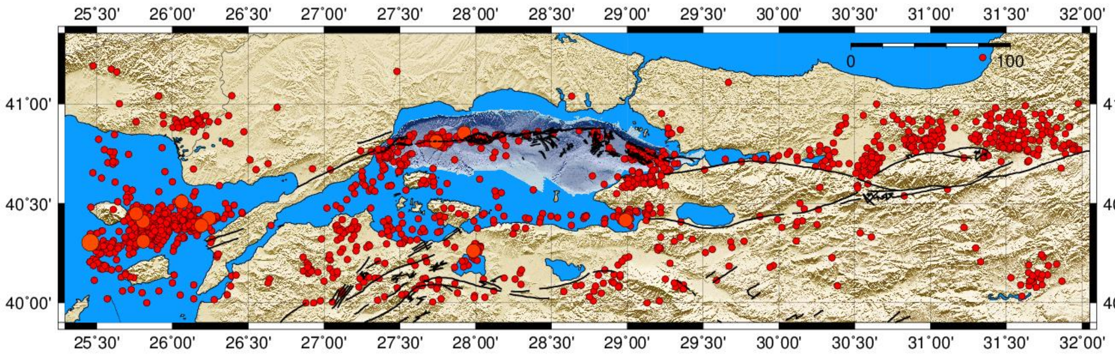

Figure 3.3. Location of events with magnitude between 3.0 and 6.8 in the observation period. Symbol sizes are proportional to magnitudes.

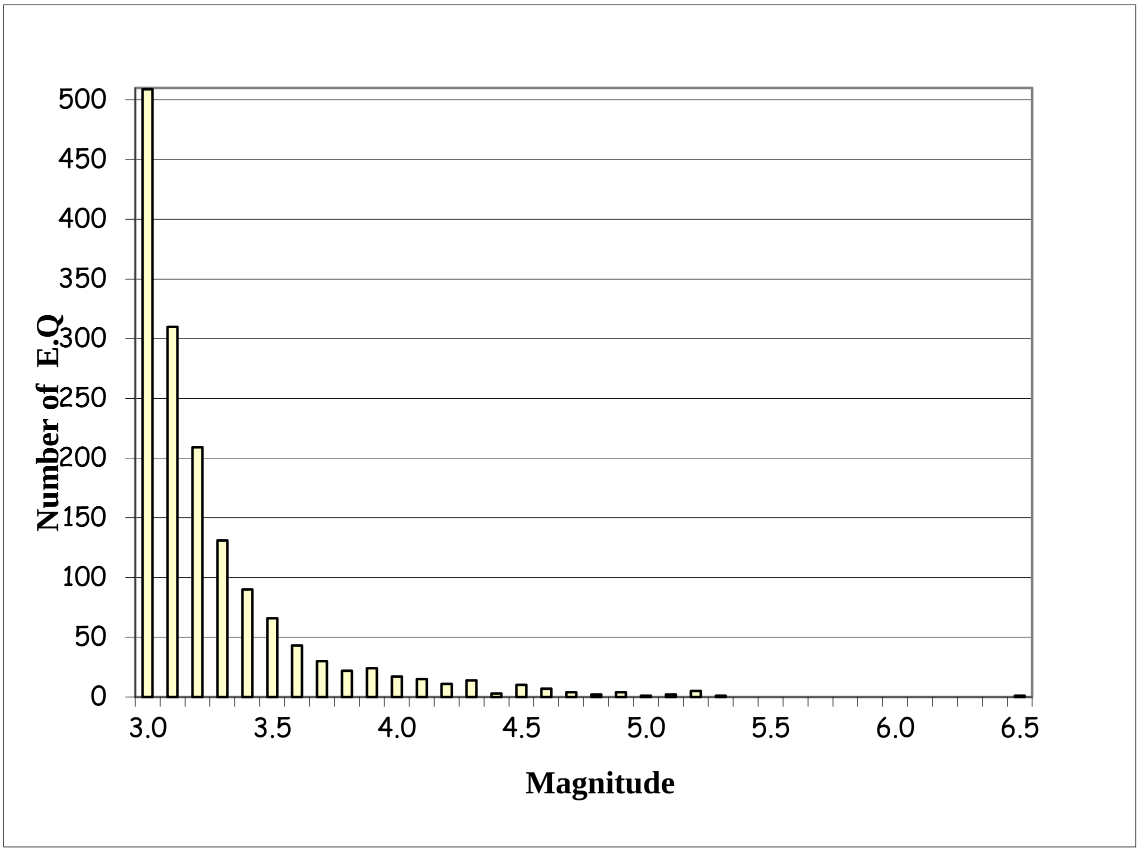

Figure 3.4. The histogram of the number of earthquake with respect to their magnitude in the observation period.

The pre-processing of the data should carefully be done before performing moment tensor inversion analysis. The success and reliability of moment tensor inversion solutions depend on the quality of the seismic records. For this purpose, seismograms are monitored using zSacWin data processing software (Figure 3.5) developed by KOERI-RETMC in order to detect signals which are clipped, have gaps, spikes, and sorted out from the database (Figure 3.6). Moreover, seismograms which have good signal to noise ratio and azimuthal coverage are chosen for inversion analysis.

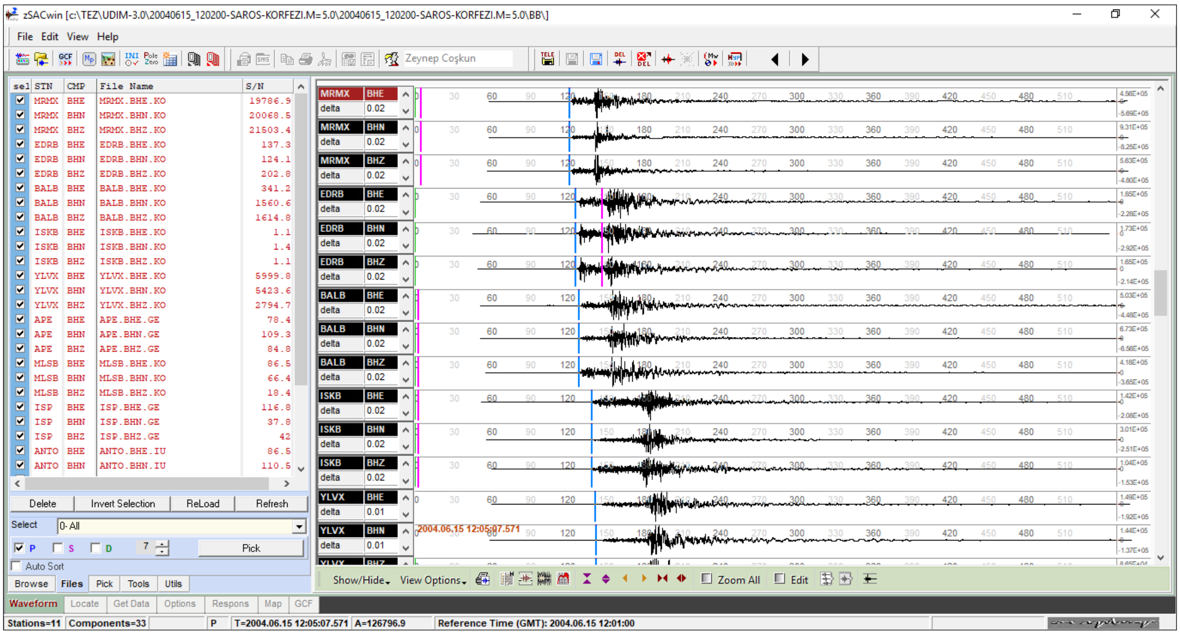

Figure 3.5. Main zSacWin screen showing an example of waveforms recorded at various broadband land seismic stations.

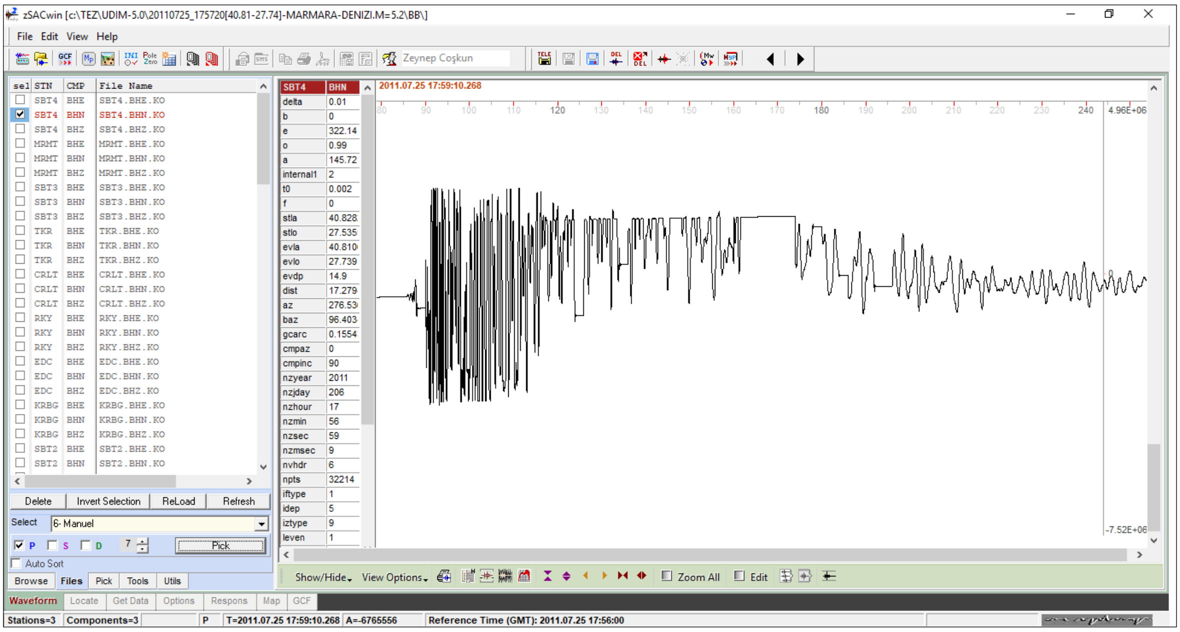

Figure 3.6. Main zSacWin screen showing an example of a clipped waveform recorded at a sea bottom station.

One of the difficulties faced with the analysis is the poor number of seismic stations close to earthquakes occur in the offshore of Aegean Sea. The large number of stations and seismograms is a primary reason for the stable solutions, but for poorly recorded events the solutions are not reasonable. A great majority of the catalogue consists of M<3.5 events where the station coverage is poor. Therefore those events are neglected from database. After removing bad quality data and M<3.5 events from the database, 187 out of 1531 events are selected for CMT analysis. The histogram in Figure 3.7 shows the number of events versus magnitude, and Figure 3.8 shows the location of events selected for CMT analysis.

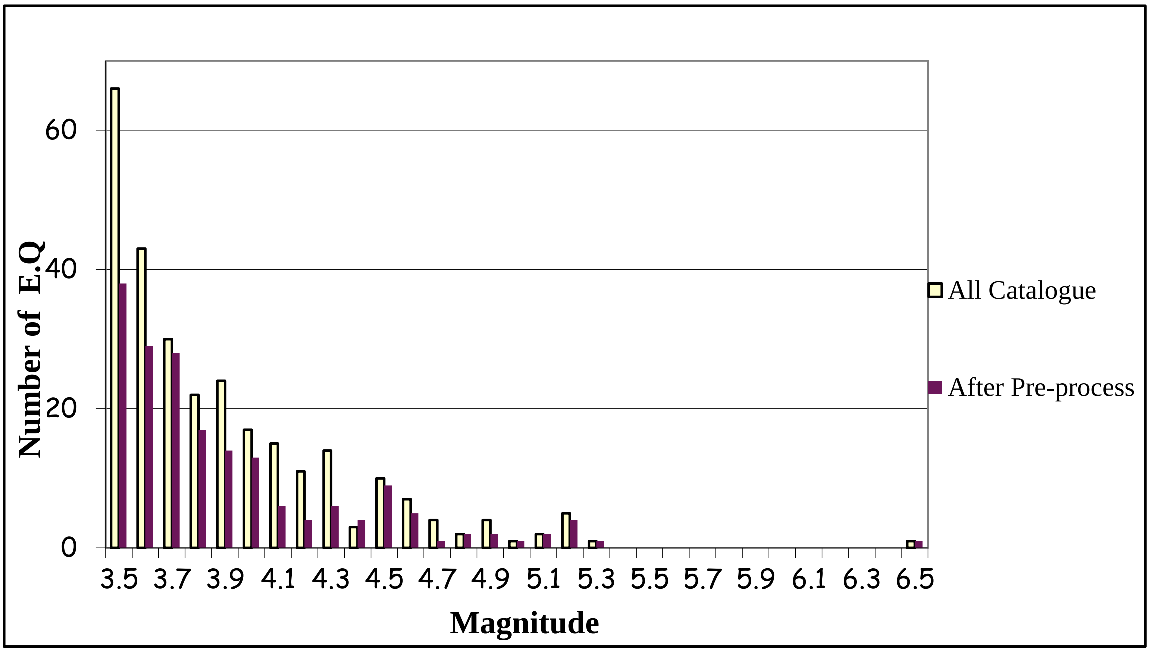

Figure 3.7. The histogram showing the number of events versus magnitude after removing bad quality data and M<3.5 events from the database.

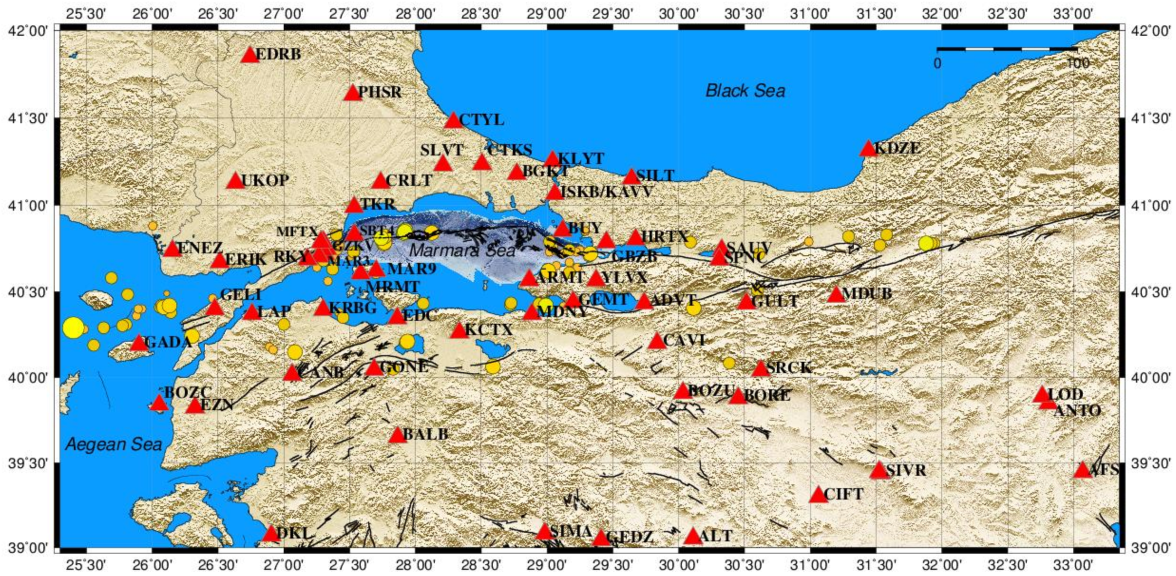

Figure 3.8. Location of events after removing bad quality data selected for CMT analysis. Yellow circles indicate earthquakes in the data base. Symbol sizes are proportional to magnitudes. Red triangles indicate broadband seismic stations operated by KOERI-RETMC.

3.2.2. CMT Inversion Procedure

The reliability and evaluation of the moment tensor inversion depend on both the amount of data and additional key factors that should be taken into account during data processing procedure. This procedure can be divided into three steps (Bock, G., 2012).

- *The first step deals with the collection and pre-processing of seismic data* The seismograms which have unclipped signals, good signal-to-noise ratio and azimuthal coverage should be used in the analysis. Mean values and linear trends should be removed in order to check if the signal has gaps or not. After this procedure, the good quality data then corrected for instrument response.

In general, the data were bandpass filtered between 0.04–0.1 Hz. For smaller events high frequencies are also used. Figure 3.9 shows the displacement spectra of a M3.5, M4.0, M4.5, and M5.0 event recorded at the same station-ISKB.

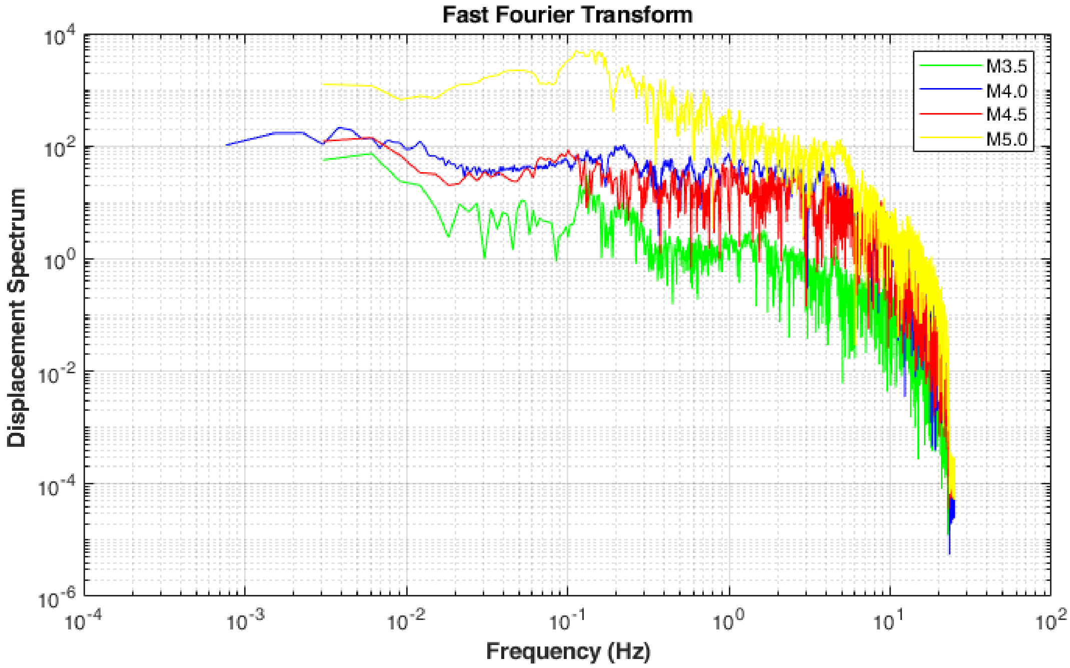

Figure 3.9. Displacement spectra of the vertical component of a M3.5, M4.0, M4.5, and M5.0 event recorded at ISKB station.

- *The second step is the calculation of accurate synthetic Green functions for specific earth model, location of the source and the position of the receiver* The synthetics are calculated following the reflectivity method of Kohketsu (1985). Although several crustal structure velocity models are examined for Marmara region, the model of Kalafat et al. (1987) is used since the observed P and S travel times fits best when compared to other models.

- *The third step is the inversion and interpretation of the inversion result and it covers the decomposition of the moment tensor using inversion algorithm* As mentioned in the previous section, in order to obtain the faulting parameters of earthquakes occurred in and around the Sea of Marmara, inversion algortihm developed by Kuge (2003) is used.

3.2.3. Data Analysis

Cygwin, a Unix-like command line interface environment designed for Microsoft Windows, is used to run CMT analysis. Input file preparation, format conversion, filtering, moment tensor inversion, plotting process is carried out using Cygwin interface. Graphics are displayed using GSview, a graphical interface for Ghostscript under Microsoft Windows. CMT analysis of 187 events occured in the study region is carried out following the steps for each event, as illustrated below.

Input file-1

- for each event, preparing event id file

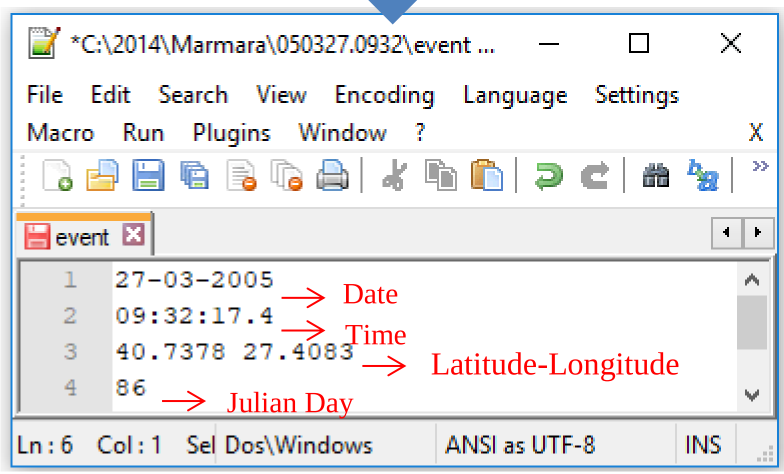

Input file-2

- for each event, preparing list of seismic stations that the records are used in CMT analysis

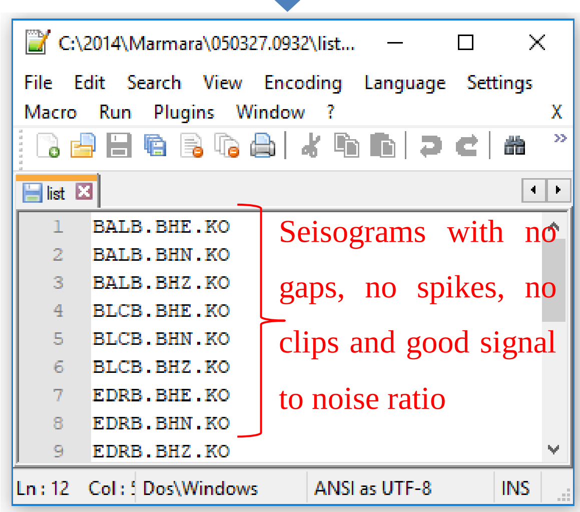

Format conversion
- convert Sac files-PC to Unix

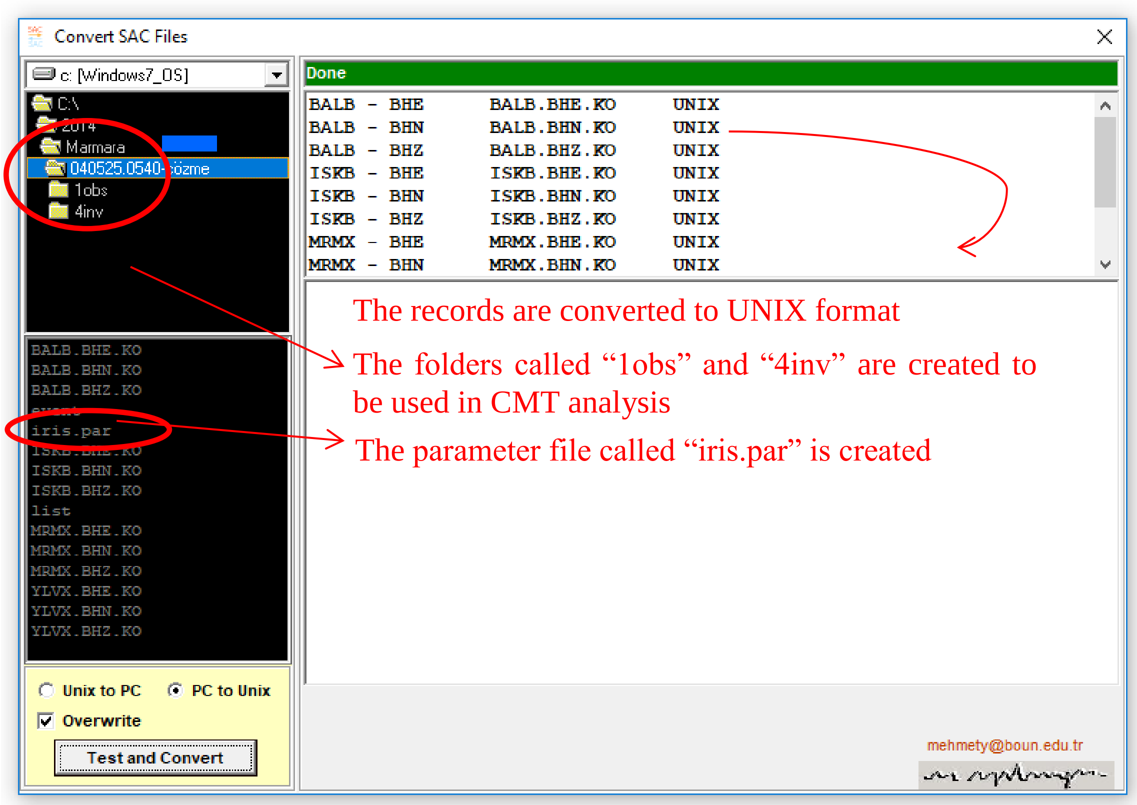

Filtering
- apply bandpass filter to seismic records

Format conversion
- Convert data to ASCII format for plotting option

Check the quality of signals
- The filtered observed data are displayed in order to see if there is a contamination of foreshock or aftershock events, or small gaps that cannot be detected in the pre-processing step, and if so remove those signals before CMT analysis step

Check and modification of parameter files for CMT inversion

- After first run, all files can be modified, such as removing poor quality components of a record, changing the duration of records, changing the initial focal depth etc..

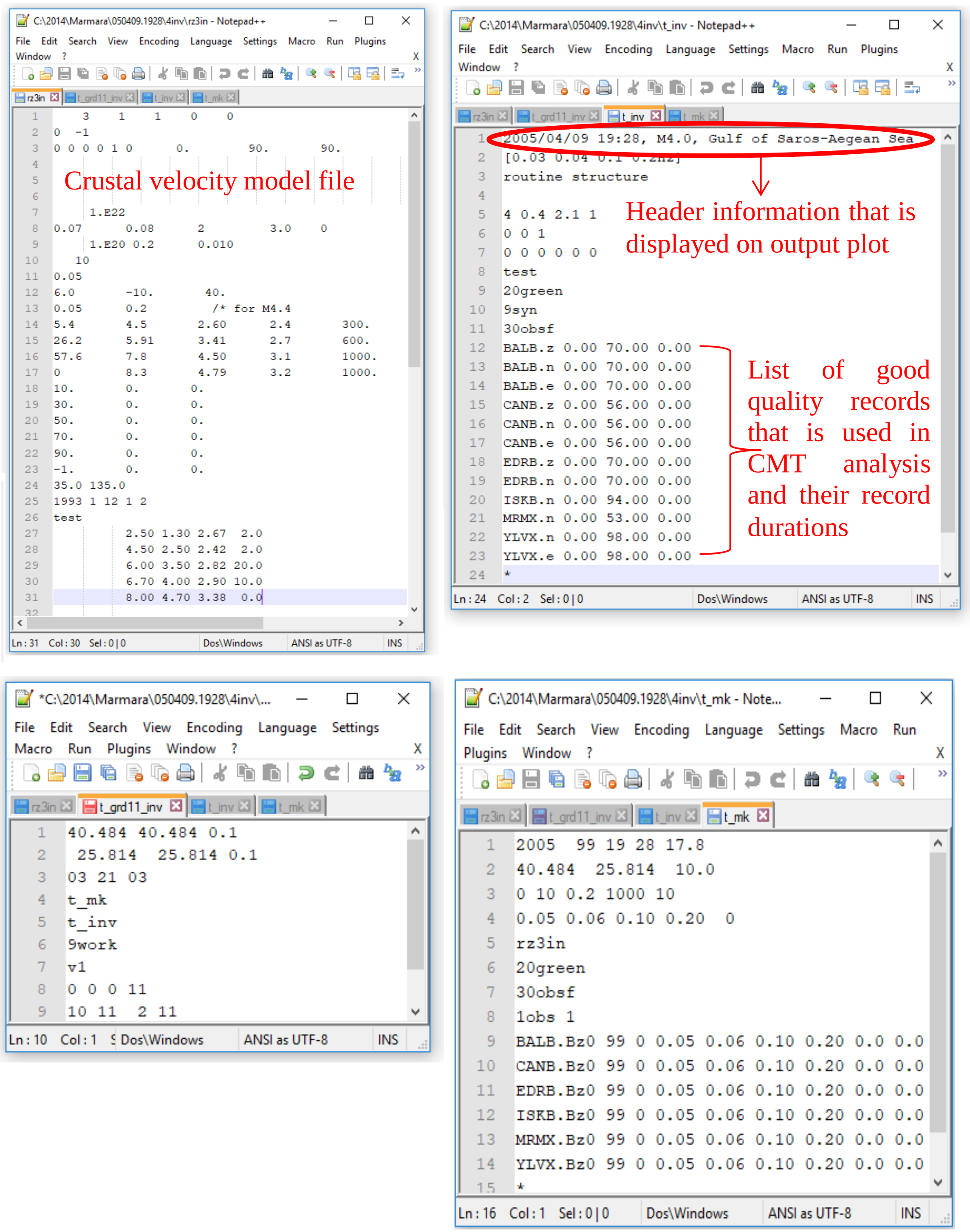

CMT inversion results

- The CMT solution of Mw 3.4 Biga-Canakkale earthquake is given as an example below.

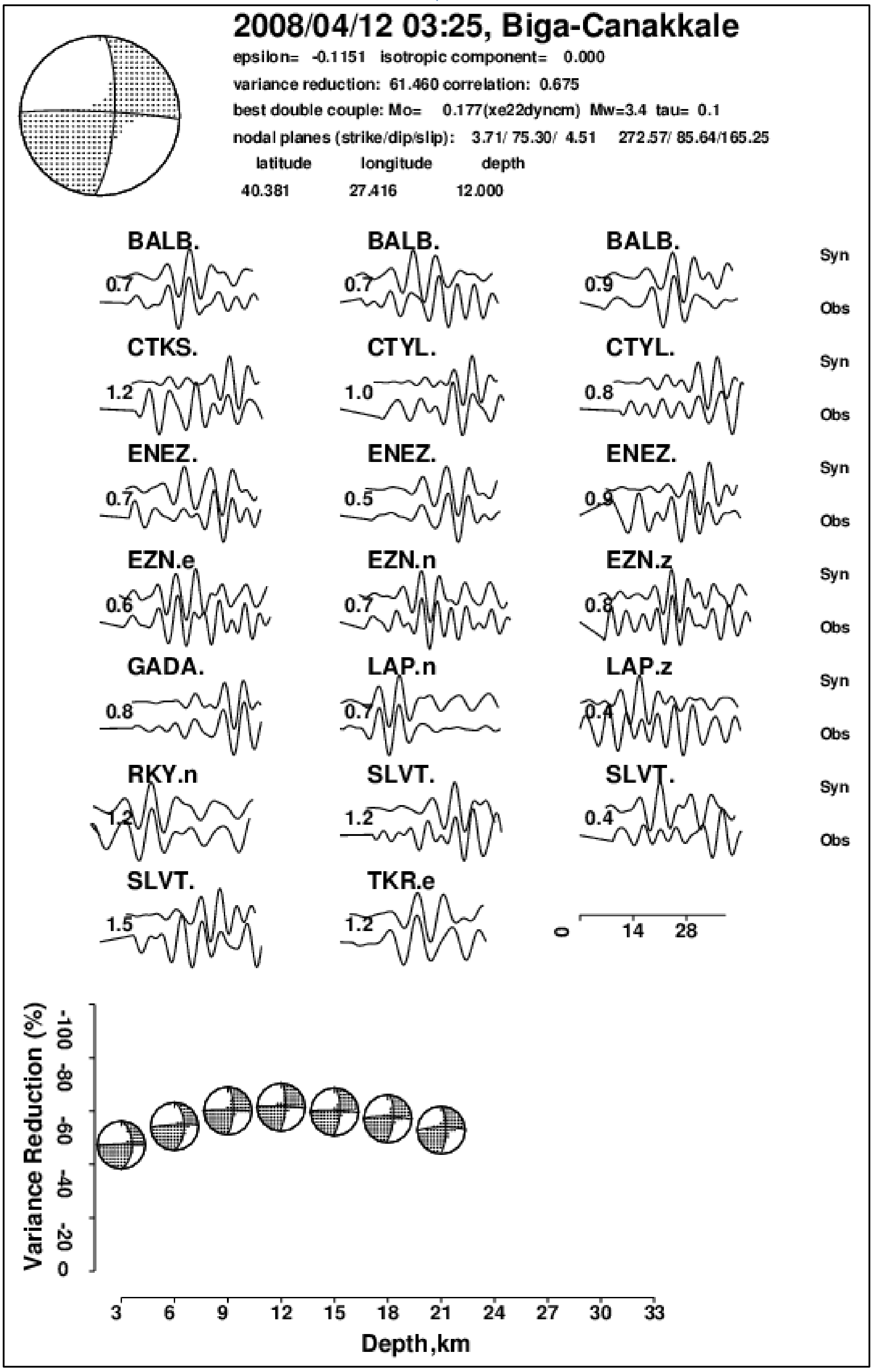

3.3. Simultaneous Inversion of First Motion Polarity Data Method

Focal mechanism solutions for many small earthquakes have been studied by many authors by using a large number of P-wave polarity data obtained by dense seismic networks (Ishida, 1992; Yamazaki et al., 1992; Castillo and Ellsworth, 1993).

It is known that there is large difference in focal mechanism solutions of earthquakes even they occur in a small area. For instance, events taking place in the San Andreas Fault zone are mostly strike-slip. Although one of the nodal planes of fault plane solutions is almost parallel to the right-lateral strike slip San Andreas Fault, in situ stress measurements made near the fault area show that the maximum principal stress is almost perpendicular to the strike of the San Andreas Fault (Zoback et al., 1987; Mount and Suppe, 1987; Shamir et al., 1988, Zoback and Healy, 1992). This observations show that the direction of the principle stress determined from focal mechanisms of individual earthquakes are differ from the in situ stress measurements.

Focal mechanism solutions of individual earthquakes, determined by using small number of P-wave polarity data, generally result in estimation error. Therefore, it becomes difficult to distinguish which of the nodal planes is the actual fault plane. In this study, the analysis of OBS data is carried out by using the method developed by Horiuchi et al. (1995), which simultaneously determines the stress tensor and the orientation of fault planes.

3.3.1. Theory

The method developed by Horiuchi et al. (1995) is based on the assumption that the slip direction of the faulting is parallel to the direction of maximum shear stress. In the method, P-wave polarity data is used for the simultaneous determination of stress tensor parameters and fault plane solutions for many earthquakes.

The ratio among principal stress σ_1, σ_2 and σ_3 is given as,

$$R = (\sigma_1 - \sigma_2) / (\sigma_1 - \sigma_3) \tag{3.2}$$

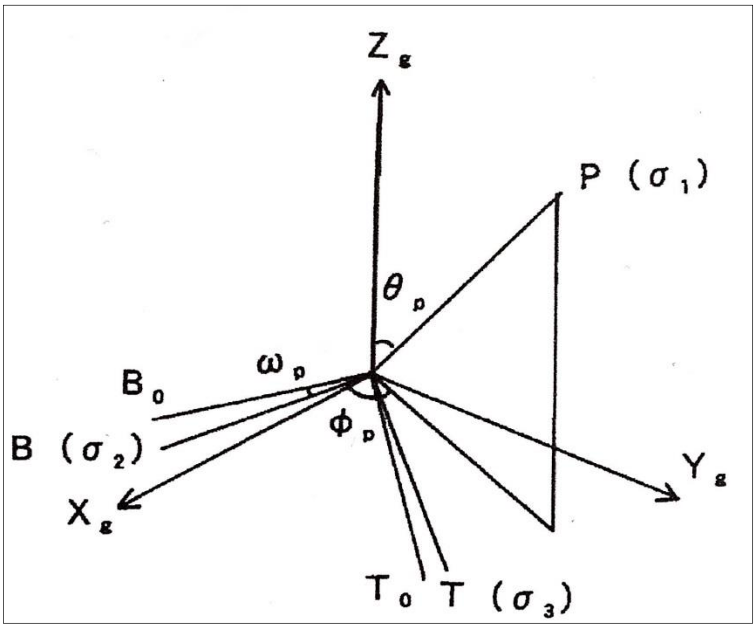

Figure 3.10. Cartesian coordinate system demonstrating geographical coordinates. As, X_g, Y_g, Z_g and corresponding principal stresses as, P= σ_1, B= σ_2 nd T= σ_3 (Horiuchi et al. 1995)

As shown in Figure 3.10, by assigning θ_p to be the inclination angle and ϕ_p to be the azimuth angle for the vector P,

$$P = X_g \cos\phi_p \sin\theta_p + Y_g \sin\phi_p \sin\theta_p + Zg \cos\theta_p \tag{3.3}$$

B and T vectors are expressed by a function of ω_p – rotation angle about P,

$$B = T \cos\omega_p + T_0 \sin\phi_p \sin\omega_p \tag{3.4}$$

$$T = - B_0 \cos\omega_p + T_0 \sin\phi_p \sin\omega_p \tag{3.5}$$

where,

$$B_0 = PZg / |PZg| \tag{3.6}$$

$$T_0 = PB_0 \tag{3.7}$$

A vector, X_i, perpendicular to the fault plane is assigned for ith event. The direction of this vector is called the pole of the fault and given as,

$$X_i = P \cos\phi_i \sin\theta_i + B \sin\phi_i \sin\theta_i + T \cos\theta_i \tag{3.8}$$

A vector, Y_0, perpendicular to T and X_i is given as,

$$Y_0 = X_i T / |X_i T| \tag{3.9}$$

By putting

$$Z_0 = X_i\ Y_0 \tag{3.10}$$

Y_i and Z_i vectors can be expressed as,

$$Y_i = Y_0 \cos\omega_i + Z_0 \sin\omega_i \tag{3.11}$$

$$Z_i = -\ Y_0 \sin\omega_i + Z_0 \cos\omega_i \tag{3.12}$$

ω_i is the angle between Y and Y_o. Since the direction of - X_i is perpendicular to the fault plane and the direction of Y_i and - Y_i is perpendicular to the auxiliary plane, X_i and Y_i vectors are defined in terms of P_m and T_m the unit vector for pressure and tension axes in the focal mechanism as,

$$X_i = (P_m + T_m) / \sqrt{2} \tag{3.13}$$

$$Y_i = (-\ P_m + T_m) / \sqrt{2} \tag{3.14}$$

The shear stress in the fault plane is defined as,

$$\tau_{xy} = c_1 \cos\omega_i + c_2 \sin\omega_i = (c_1^2 + c_2^2)^{1/2} \sin(\omega_i + \omega_0) \tag{3.15}$$

where,

$$c_1 = \cos\omega i \cos\theta_i \sin\phi_i \cos\phi_i (\sigma_1 + \sigma_2) \quad (3.16)$$

$$c_2 = \sin\omega_i \sin\theta_i \cos\theta_i (\sigma_1 \cos^2\phi_i - \sigma_2 \sin^2\phi_i - \sigma_3) \quad (3.17)$$

$$\omega_0 = \tan^{-1} (c_1/c_2) \quad (3.18)$$

The shear stress defined in Equation (3.15) becomes maximum when $\omega_i + \omega_0 = \pi/2$ and minimum when $\omega_i + \omega_0 = -\pi/2$. When the signs are taken into consideration, in order to satisfy Equation (3.13) and Equation (3.14) the equation becomes,

$$\omega_i = \omega_0 - \pi/2 \quad (3.19)$$

where τ_{xy} becomes minimum in the slip direction. If the pole of the fault is expressed as Equation (3.8), putting Equation (3.19) into Equation (3.11) gives the slip direction.

The theoretical amplitude of the P wave is expressed as,

$$S_{ij} = C (A_{ij} X_i) (A_{ij} Y_i) \quad (3.20)$$

where C is a constant and A_{ij} is a vector showing the direction of j^{th} station for i^{th} event. In order to calculate the number of inconsistent stations, the polarity of the theoretical amplitude of the P wave is compared with the observations. The total number of inconsistent stations is expressed as,

$$N_{tot} = \sum_i \sum_j N_{ij} (\theta_p, \phi_p, \omega_p, R, \phi_t, \theta_t, A_{ij}, P_{ij}) \quad (3.21)$$

where θ_p, ϕ_p, ω_p, R are the four parameters of the stress tensor, ϕ_t, θ_t are the two parameters for the pole of the fault plane, P_{ij} is a reading of a P wave polarity and N_{ij} is a value of the inconsistency.

Since the number of inconsistent stations for an event is independent of directions of fault planes for other events, there is no need to make a grid search for all combinations of unknown parameters (Horiuchi et al. 1995). Therefore, the total number of inconsistent stations can be calculated as,

$$N_{tot} = \sum_i M_i (\theta_p, \phi_p, \omega_p, R) \quad (3.22)$$

where M_i is the minimum number of inconsistent stations for the i^{th} event. The number of inconsistent stations is calculated for all cases of θ_p, ϕ_p, ω_p which define the orientation of the focal mechanism solution of i^{th} event. The calculation is made for all events making a grid search as precise as possible. M_i is then calculated using these data. The calculations are carried out by the program developed by Horiuchi et al. (1972).

3.3.2. Data

The data used in the analysis are obtained from free-fall pop-up 15 OBS stations deployed in the scope of MARDIM project, which aims to contribute to the development of efficient disaster mitigation policy and strategies based on multidisciplinary research and disaster education programs in Turkey.

During the past decades, OBS analysis play important role for the study of offshore seismicity. OBS sit on the seafloor in a fixed position and record sound waves that travel through the earth and the water. One of the main objectives to use OBS’s is to expand seismic network and azimuthal coverage around the epicenter which allows precise seismic activity location and focal mechanism determination.

Microearthquake seismicity study in a region may provide useful information about the fault geometry and fault characterization. Since land seismic stations provide inadequate data about the microearthquake activity, OBS stations are deployed beneath the Sea of Marmara in order to clarify the fault geometry and obtain more detailed information about the seismic activity (Yamamoto et.al., 2015)

OBS analysis are integrated with the moment tensor inversion of earthquakes in the Sea of Marmara with an aim to understand better the fault segmentation and fault geometry of the North Anatolian Fault crossing the Sea of Marmara. For this purpose the waveform data between July 2015-November 2016 recorded by 15 OBS seismic stations deployed by JAMSTEC along the northern branch of the North Anatolian Fault crossing the Marmara Sea are utilized (Yamamoto et al. 2015; 2017). The OBS deployment area covers the offshore Tekirdağ in the west and extends eastward towards Kumburgaz Basin (Figure 3.11). The waveform data from the last two OBS deployments in 2014-2015 and 2015-2016.

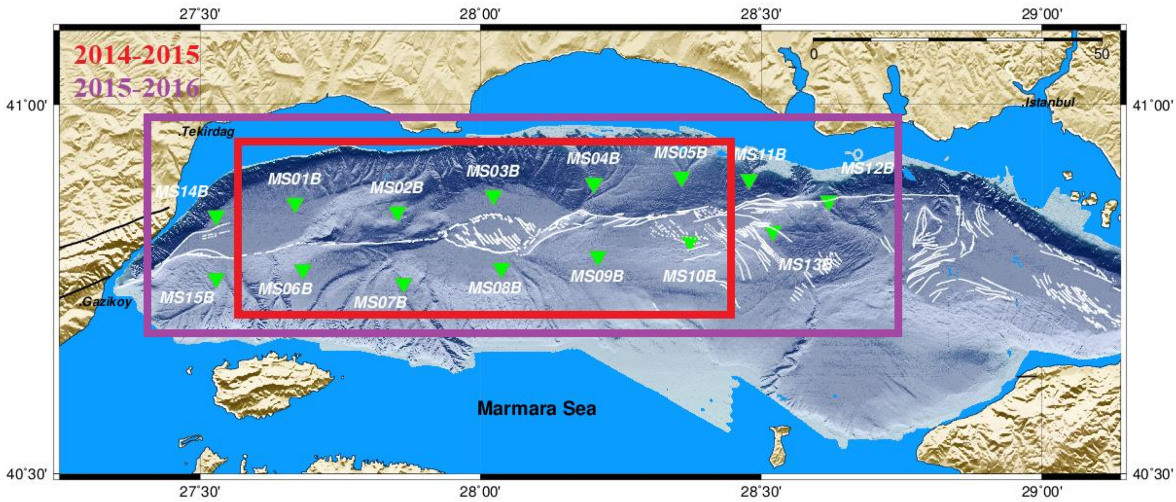

Figure 3.11. Locations of OBS stations. Green triangles indicate OBS stations.

Depending on their magnitude, the size of the earthquakes analyzed in the OBS analysis can mostly be classified as microearthquakes. Microseismic data is generally affected by stationary and background noises which make difficulty in manual P-phase arrival picking, eventually the number of polarities are limited. To increase the number of polarities and improve the azimuthal and take-off coverage, the OBS stations are integrated with the land seismic stations operated by KOERI. The locations of land seismic stations are given in Figure 3.12.

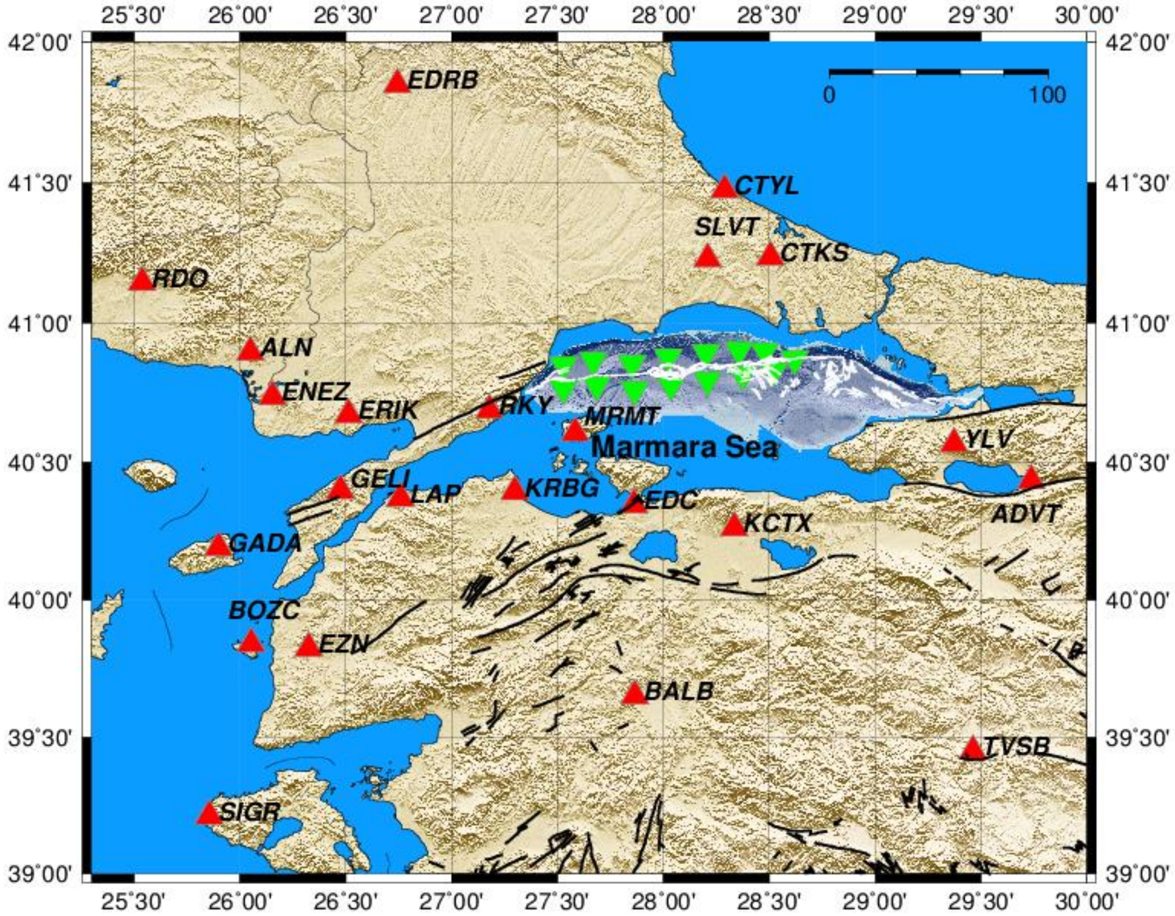

Figure 3.12. Locations of land seismic stations together with OBS stations. Green triangles indicate OBS stations and red triangles indicate land seismic stations.

The OBSs are equipped with 4.5 Hz three-component geophones and hydrophones (Figure 3.13.) (Takahashi et al. 2015). The sampling rate is 100 Hz. The stations are deployed 10 km apart on the seafloor and the locations on the seafloor are determined by triangulation. The OBS clock with GPS time is calibrated before deployment and right after recovery (Yamamoto et al. 2017).

Figure 3.13. Deployment of an OBS station
(https://www.jamstec.go.jp/obsmcs_db/e/photo/index.html?name=04)

OBS analysis covers 102 source mechanism solutions of earthquakes with magnitudes range from M1.9 to M4.6 occurred in the Sea of Marmara. 76 out of 102 events are recorded by 10 or more OBS stations, 6 out of 102 events are recorded by less than 10 OBS stations, in order to increase the number of polarities, land seismic station records are integrated with the OBS's. In order to contribute to the findings in the first section on the segmentation between Ganos Fault and Tekirdağ Basin, 20 earthquakes recorded by land seismic stations are used to determine the focal mechanisms of events occured in the study region. The histogram in Figure 3.14 shows the number of earthquakes versus magnitude occured covering the period between 2013 and 2016 and Figure 3.15 shows the locations of events recorded by OBS and land seismic stations.

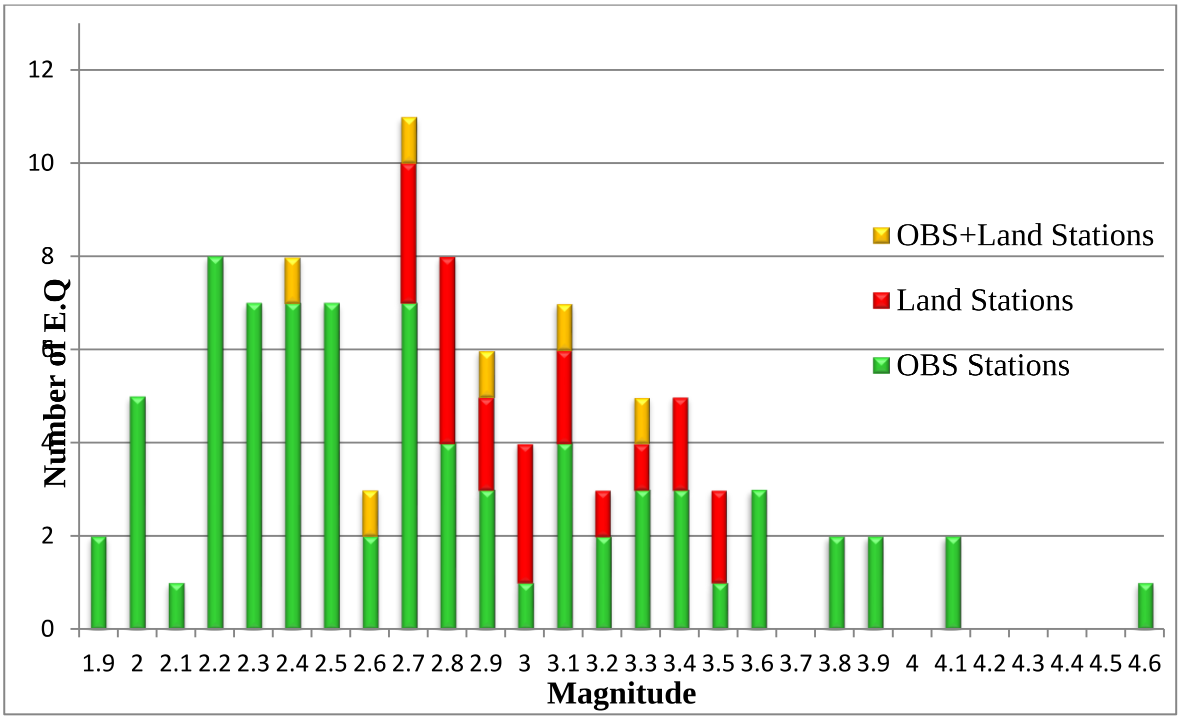

Figure 3.14. The histogram of the number of earthquake with respect to their magnitude covering the period between 2013 and 2016.

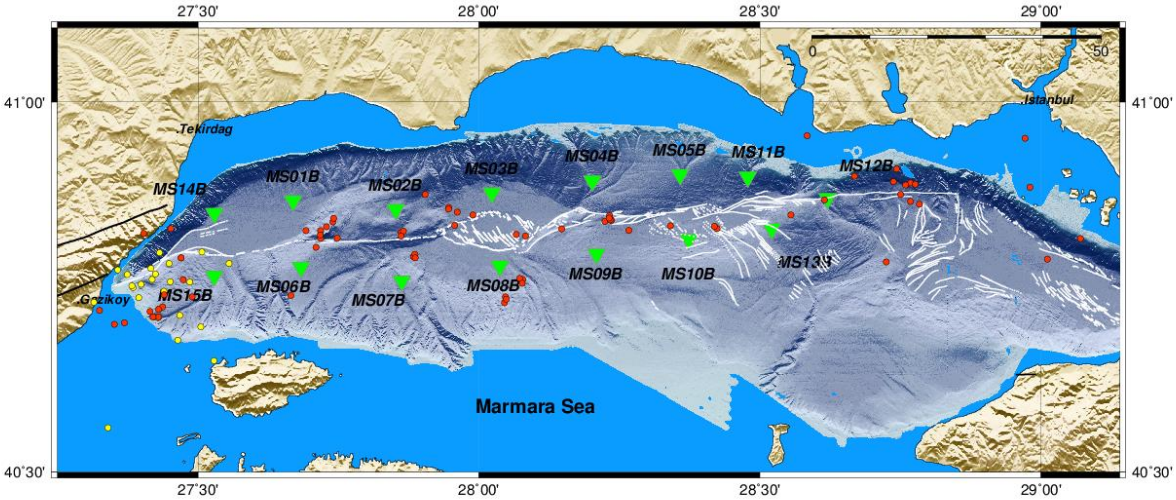

Figure 3.15. Location of events with magnitude between 1.9 and 4.6 recorded by OBS and Land seismic stations between 2013-2016. Green triangles indicate the location of OBS Stations. Yellow circles indicate events recorded by OBS and Land seismic stations. Red circles by only OBS stations.

3.3.3. Determination of Polarity Data

Data processing procedure is carried out using two different analysis software; zSacWin and WIN system. zSacWin data processing software developed by Mehmet Yılmazer, KOERI- RETMC is used for earthquake analysis and P wave polarity observations recorded by land seismic stations. WIN system, which is standard waveform processing software in Japan developed by Taku Urabe, Earthquake Research Institute, the University of Tokyo, is used for earthquake analysis and P wave polarity observations recorded by OBS stations.

The dataset analyzed using zSacWin is based on Hypo71 software (Lee and Lahr 1972). 1-D velocity model used in zSacWin is the velocity model developed by Kalafat et al. (1987) (Table 3.1).

Table 3.1. 1-D velocity model developed by Kalafat et al. (1987)

Depth (km)	**Vp (km/s)**	**Vs (km/s)**
0.00	4.50	2.60
5.40	5.91	3.10
31.6	7.80	4.50
89.2	8.30	4.80

The dataset analyzed using WIN system uses the HYPOMH program (Lee and Lahr 1972) for hypocenter calculation. 1-D P-wave velocity model is established for OBS study by combining 1-D velocity model developed by Gurbuz et al. (2000) and Bayrakci et al. (2013) (Yamamoto et al. 2015) (Figure 3.16).

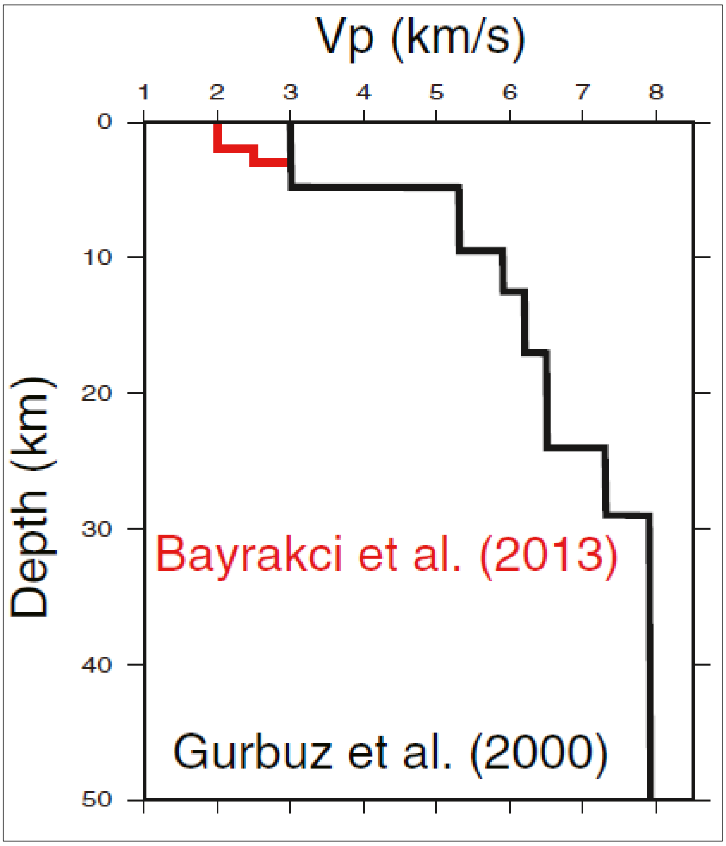

Figure 3.16. 1-D velocity model used for OBS dataset.

The first arrivals of P and S waves with first motion polarities of P waves are manually picked on unfiltered records (Figure 3.17, Figure 3.18, Figure 3.19, and Figure 3.20). The P wave polarities of first arrivals are carefully done before performing focal mechanism analysis. The success and reliability of fault plane solutions depend on the quality of the seismic records. Since the phase readings are carried out on unfiltered data, seismograms which have good signal to noise ratio are selected for focal mechanism analysis.

After determination of first motion polarity data, the data is elaborated using Horiuchi et al. (1995) analysis routine, where simultaneous inversion of the polarities of cluster of earthquakes occur in a certain small area are performed to obtain a stress tensor and focal mechanism of the individual events in the cluster.

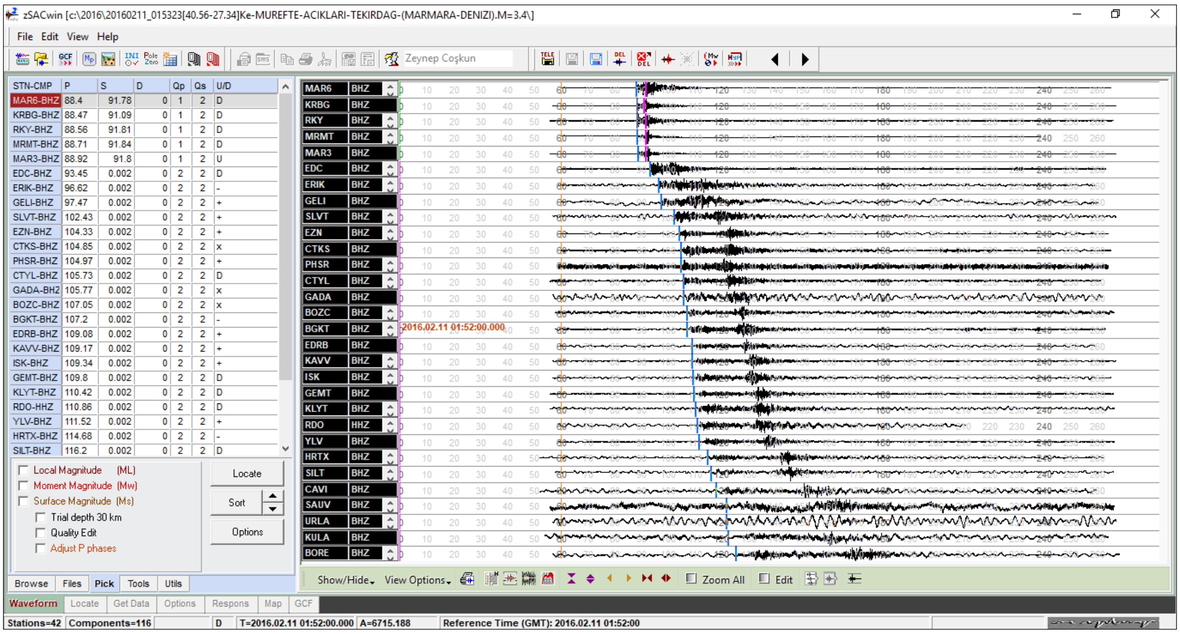

Figure 3.17. zSacWin screen showing observed seismograms recorded by land seismic stations

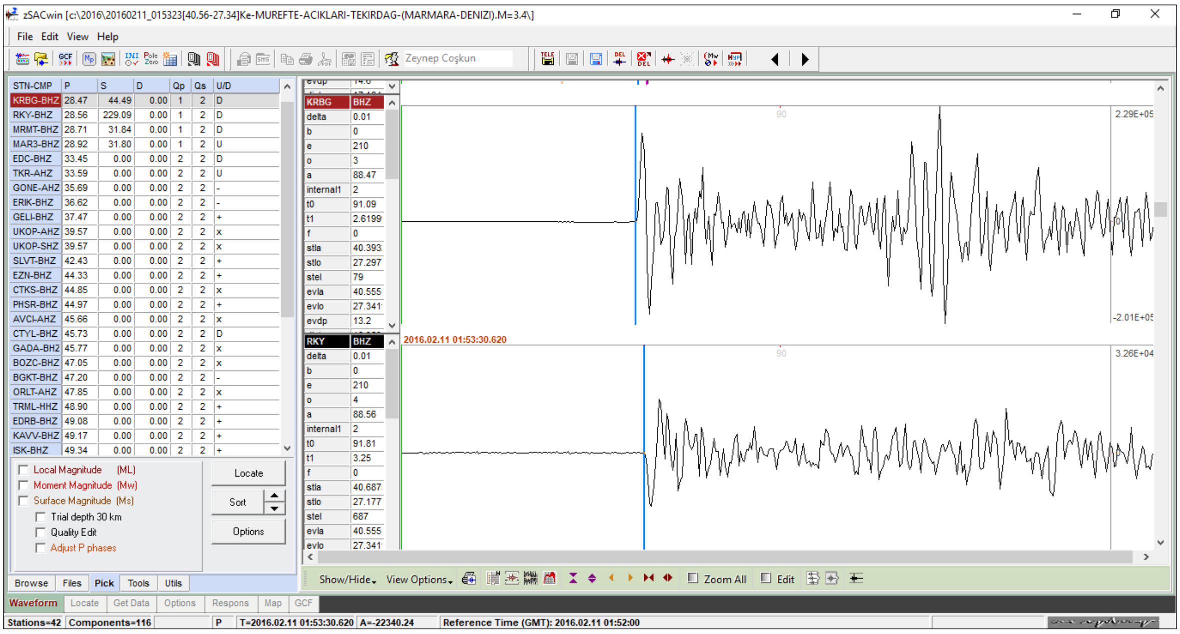

Figure 3.18. zSacWin screen showing examples of P-wave polarity picking on unfiltered data

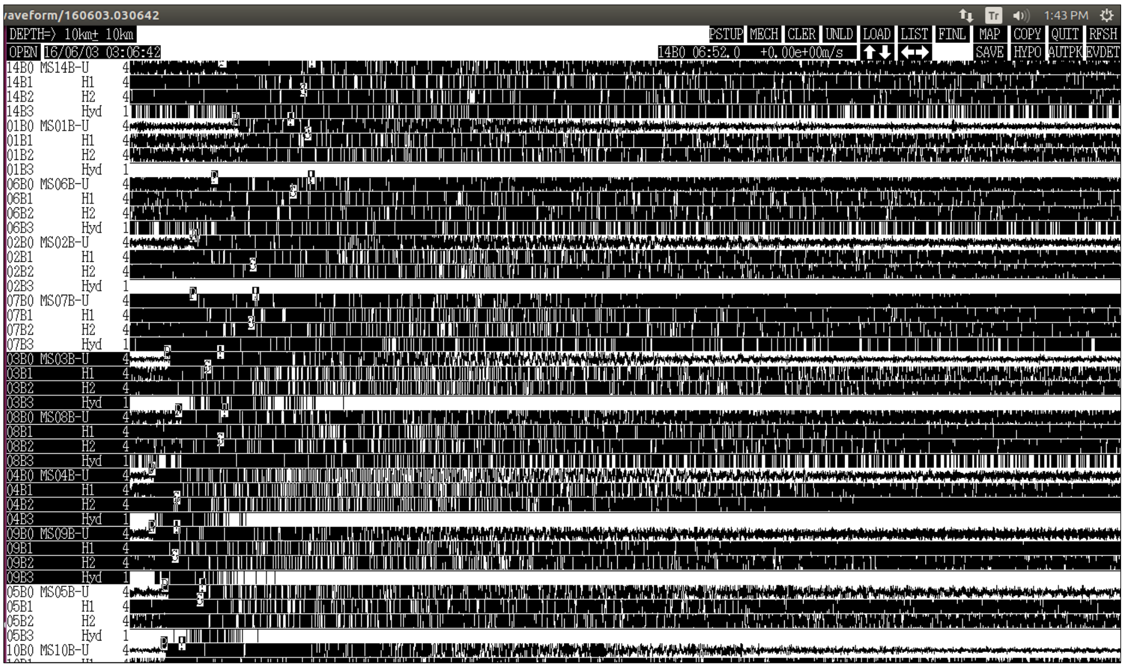

Figure 3.19. WIN system screen showing observed seismograms recorded by OBS stations

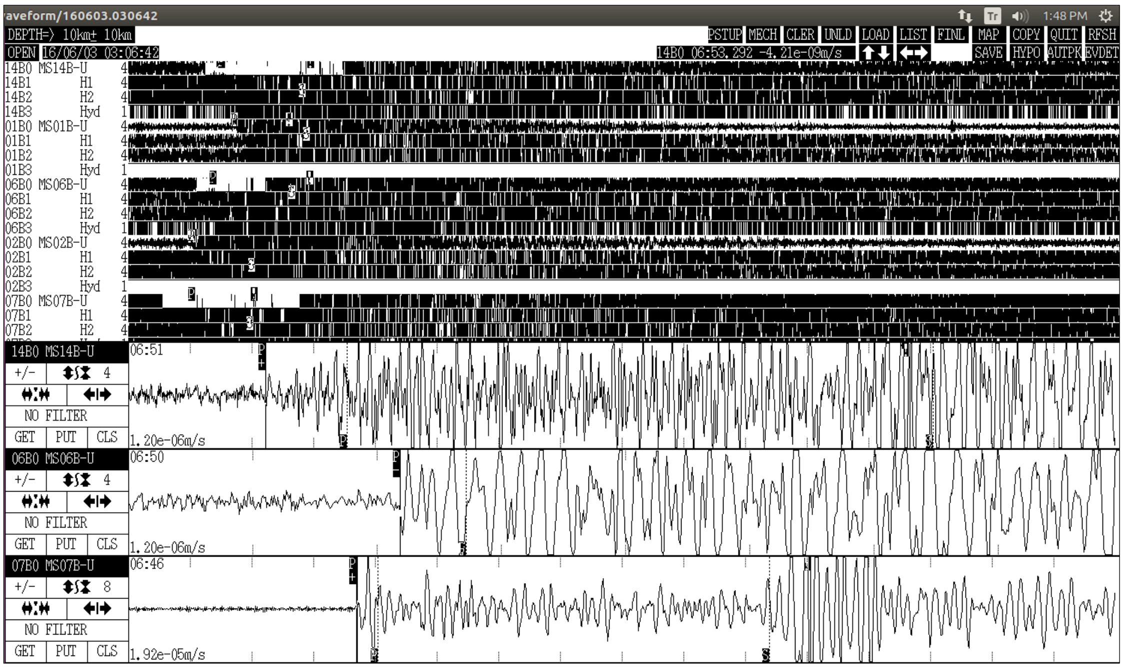

Figure 3.20. WIN system screen showing examples of P-wave polarity picking on unfiltered data

3.3.4. Determination of Focal Mechanisms

The method developed by Horiuchi is based upon on the hypothesis that the direction of slip of the faulting is parallel to maximum shear stress direction. In the method, P-wave polarity data is used for the simultaneous determination of stress tensor parameters and fault plane solutions for many earthquakes.

After determination of P-wave polarity data, as explained in Subsection 3.3.3, the results are written to a file, in the format of the input file appropriate for the program developed by Horiuchi et al. 1972. Microsoft Windows Command Propmt is used to run executable files in the program. Graphics are displayed using GSview, a graphical interface for Ghostscript under Microsoft Windows. Stress calculation and fault plane deteremination of 102 events occured in the study region is carried out running the following programs from (1) to (5) with the given order, as illustrated below.

(1) test_data

This program generates a set of theoretical polarity data to check programs. The input parameters for this program are the four parameters of stress tensor and the input parameters are given from the key as shown in Figure 3.21.

az and th of pressure axis = 300˚, 80˚
rotation angle = 30˚
r = 0.5

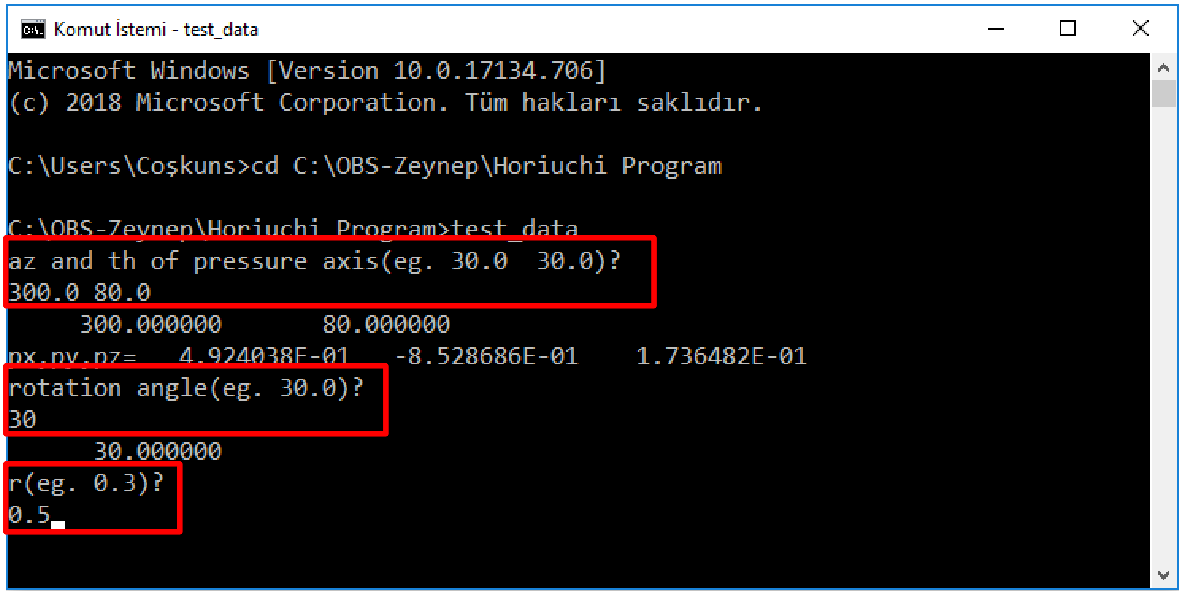

Figure 3.21. Microsoft Windows Command Prompt screen showing the steps of test_data program.

Name of the output file is "mecha_test.dat". The output file includes polarity data for many artificial events having various types of fault plane solutions. All fault plane solutions satisfy stress condition defined by the four input parameters.

(2) stress

This program calculates the number of inconsistent stations for all cases of az, th and rotation agle which define the orientation of focal mechanism of each event. The calculation is done with an interval of 5 degrees and all values are stored on disk. The input of the program is "stress_parm.dat" (Figure 4.22) and "mecha_test.dat".

"stress_parm.dat" file contains;

-grid interval in degree

-latitude range of study area

-longitude range of study area

-depth range of study area

-file name of polarity data

Polarity data is the .txt file, which the P-wave polarity results are written in the format of the input file (Figure 3.23).

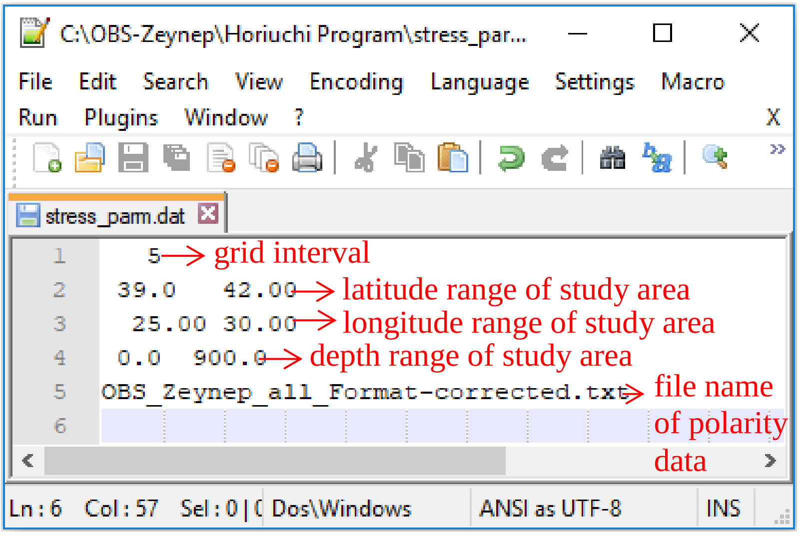

Figure 3.22. “stress_parm.dat” file format.

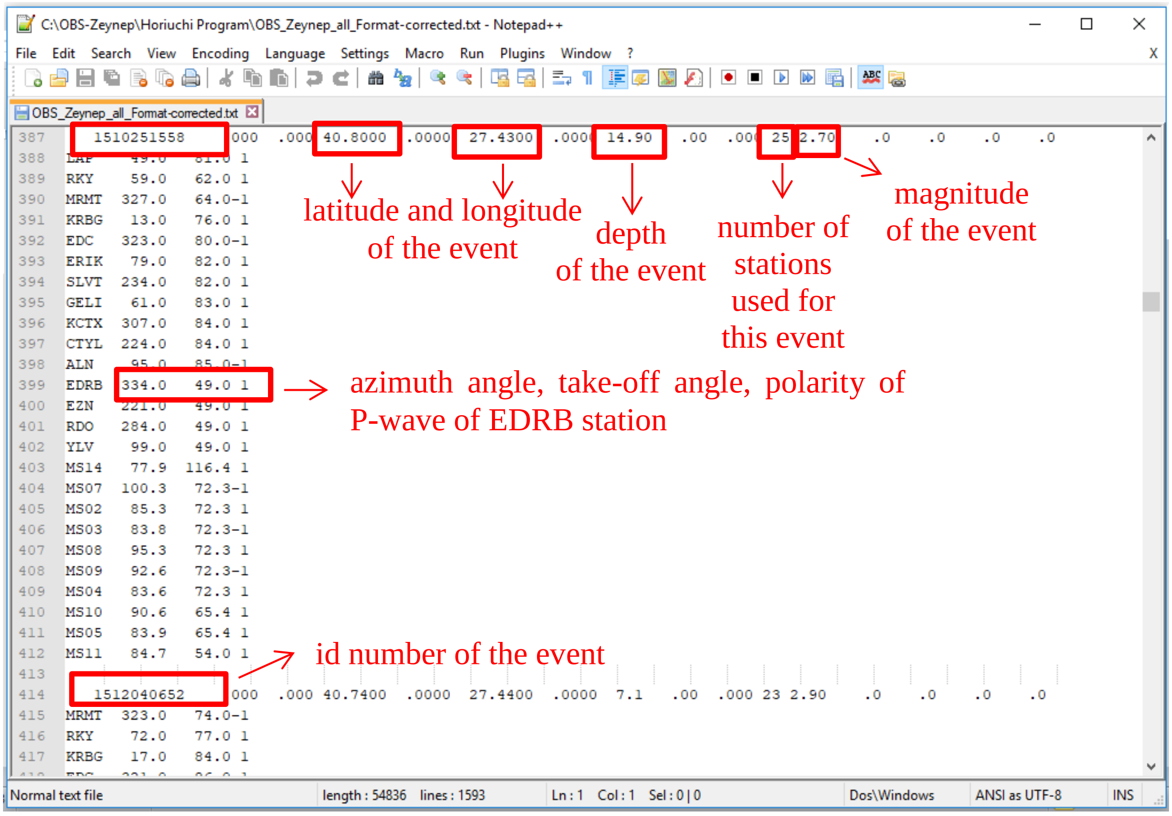

Figure 3.23. File format of polarity data.

Name of the output file is “mecha_ans.dat”. The output file includes number of inconsistent station data. Focal mechanism solutions of individual events are also calculated in this step (Figure 3.24).

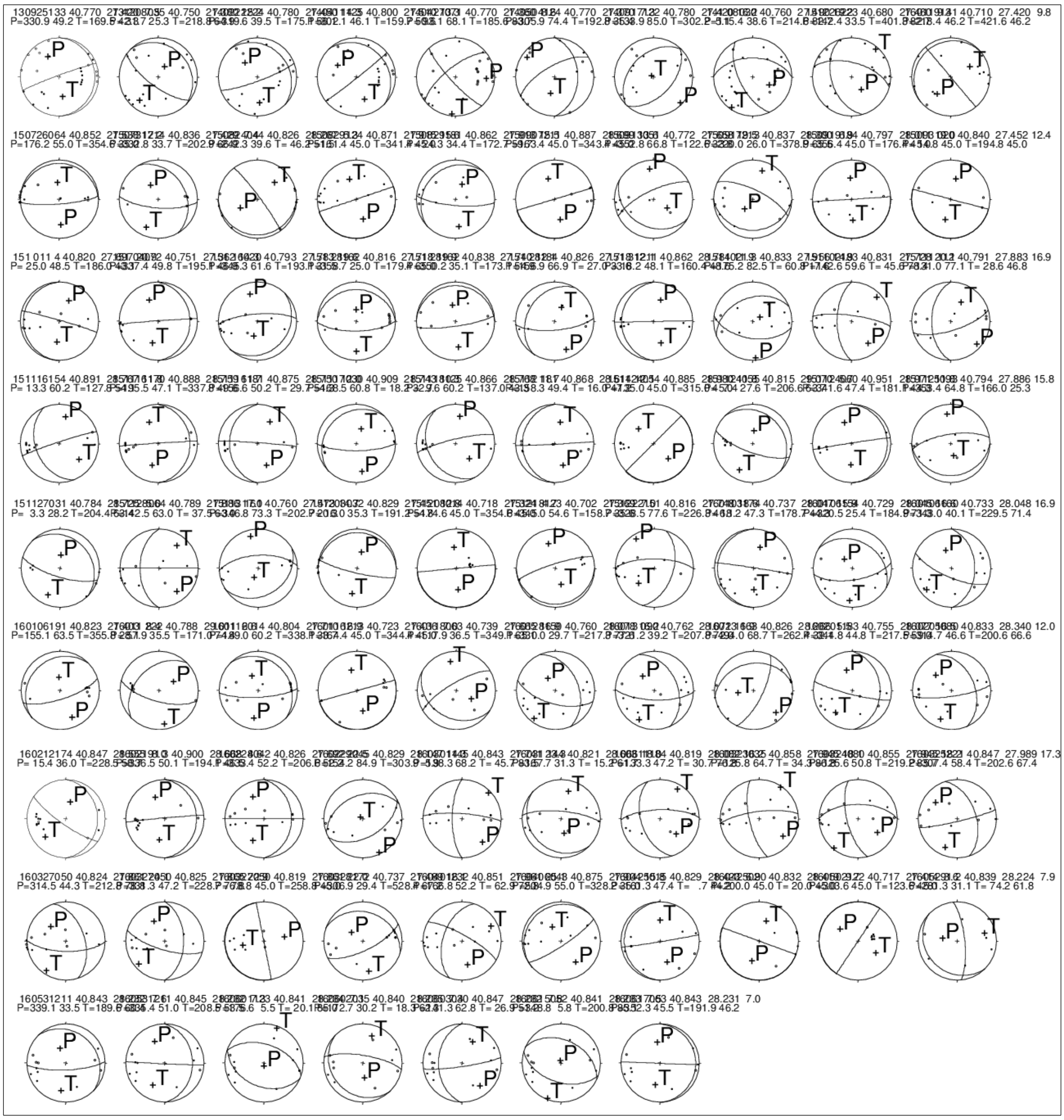

Figure 3.24. Equal area projections on the lower focal hemisphere showing the distribution of polarity data.

(3) stress2

This program calculates stress tensor. Input data is the “mecha_ans.dat” file calculated in step 2. The name of the output file is “ans_stress_field.dat” (Figure 3.25). The output data gives the minimum number of total inconsistent stations when the principal stress is in a direction defined by az and th. This value is determined by changing all other parameters with certain intervals.

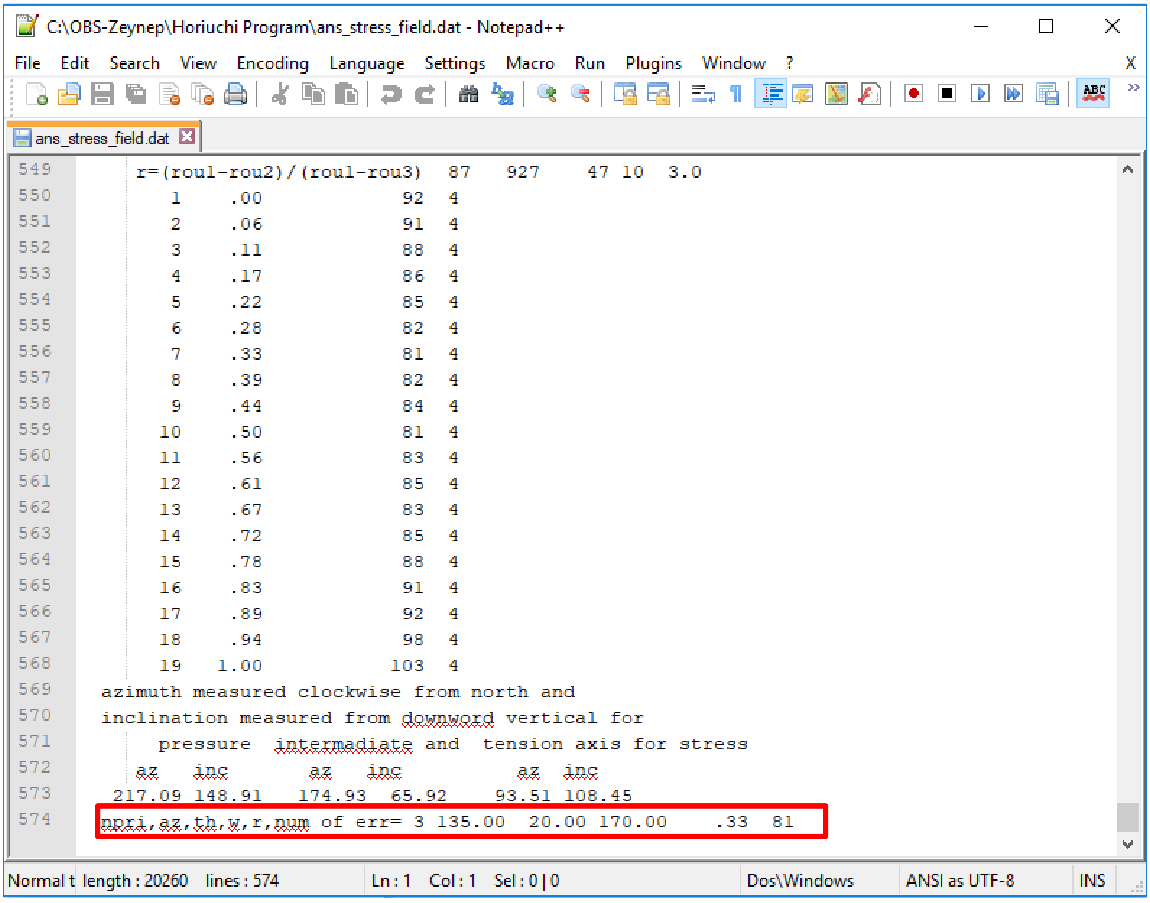


```
   r=(roul-rou2)/(roul-rou3)  87   927    47 10  3.0
      1    .00             92  4
      2    .06             91  4
      3    .11             88  4
      4    .17             86  4
      5    .22             85  4
      6    .28             82  4
      7    .33             81  4
      8    .39             82  4
      9    .44             84  4
     10    .50             81  4
     11    .56             83  4
     12    .61             85  4
     13    .67             83  4
     14    .72             85  4
     15    .78             88  4
     16    .83             91  4
     17    .89             92  4
     18    .94             98  4
     19   1.00            103  4
azimuth measured clockwise from north and
inclination measured from downword vertical for
     pressure  intermadiate and  tension axis for stress
   az   inc        az   inc          az  inc
 217.09 148.91   174.93  65.92     93.51 108.45
npri,az,th,w,r,num of err= 3 135.00  20.00 170.00     .33   81
```


Figure 3.25. The output data of “ans_stress_field.dat” file

(4) stress3

This program determines the auxiliary plane and fault plane. Input data is the "ans_stress_field.dat" file calculated in step 3 and polarity data. The orientations of fault planes are shown in Figure 3.26.

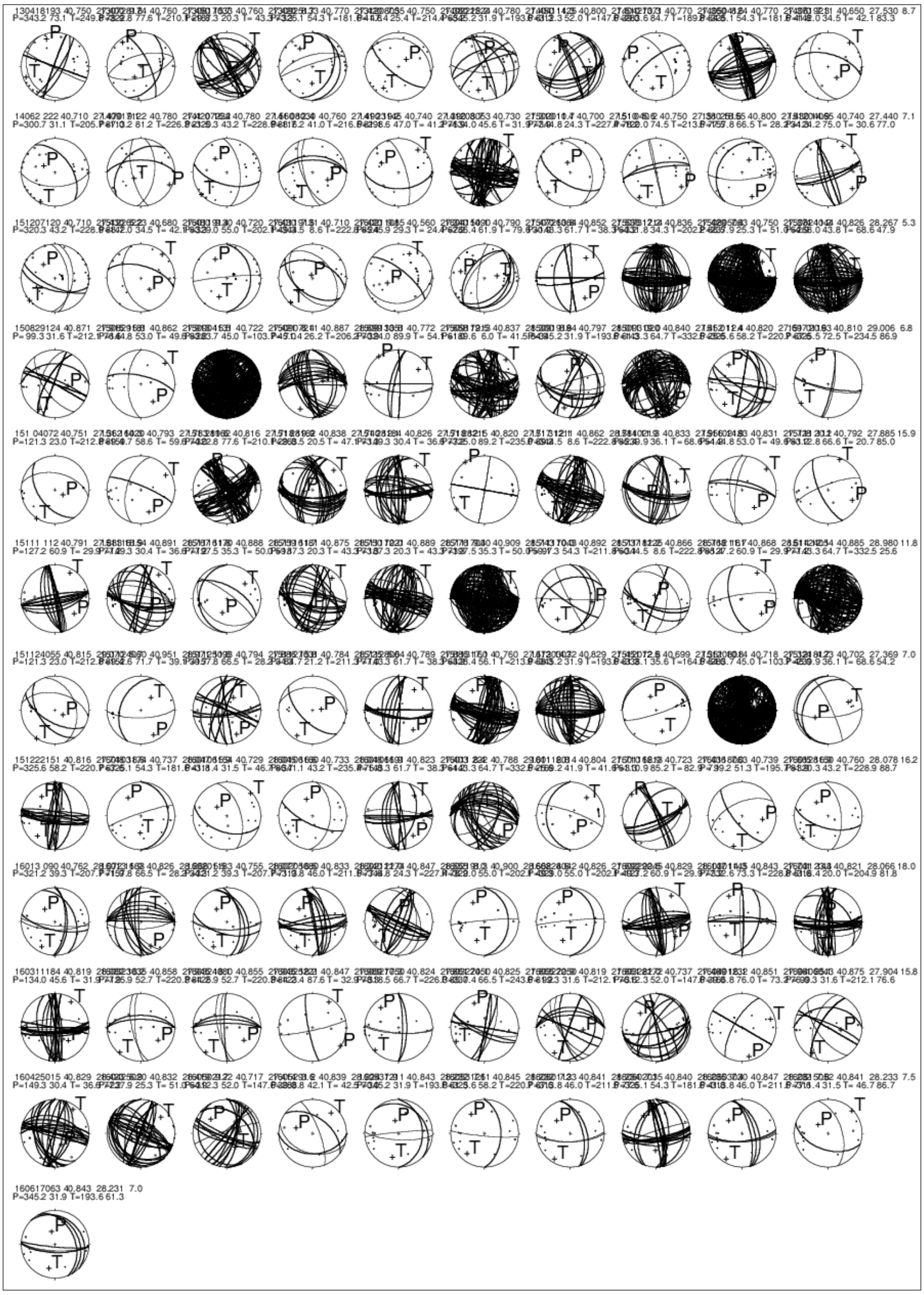

Figure 3.26. Equal area projections showing the orientations of fault planes of events in the data set. Thick lines represent fault planes and thin lines represent auxiliary planes.

4. RESULTS AND DISCUSSIONS

OBS and broadband land stations are used in order to derive faulting characteristics in and around the Sea of Marmara. The results of the analysis and the main findings are given in the subsections of this chapter in detail.

4.1. CMT Results

The multiple solutions giving a range of possible moment magnitude values, depth values and focal mechanisms are obtained for each earthquake. The best solution for each earthquake is chosen using variance reduction. The reliability of the solutions is also based on the variation of produced focal mechanisms for each event. The solution is accepted as sufficiently accurate when a clear best focal mechanism and other produced solutions show similar focal mechanisms (Figure 4.1), on the other hand, when the small changes in the source depth show very different mechanisms, the solution is considered as inaccurate (Figure 4.2).

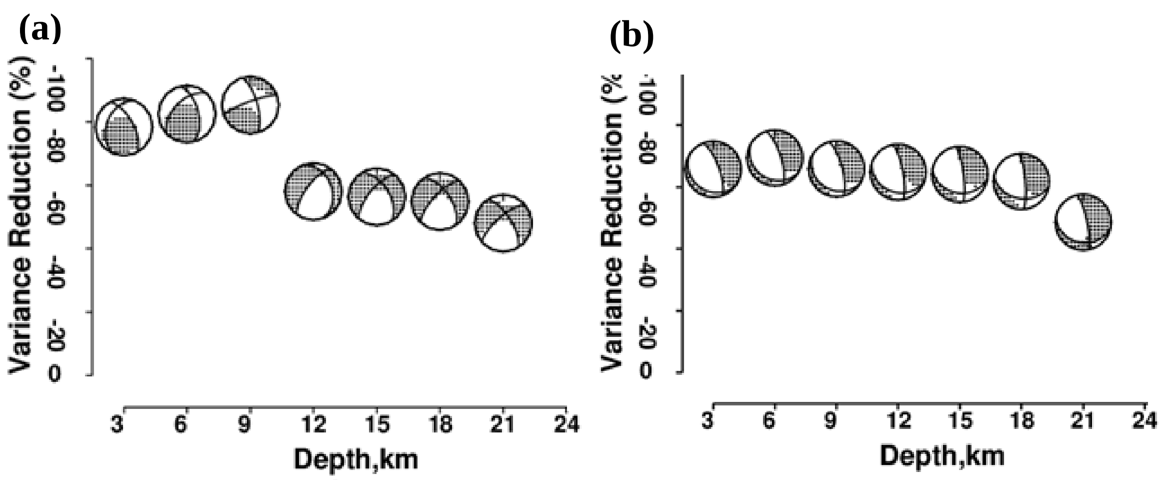

Figure 4.1. Example of two accurate CMT solution. (a) The variance reduction versus depth plot of 27.03.2015 earthquake (Mw3.5), (b) 27.06.2005 earthquake (Mw3.4).

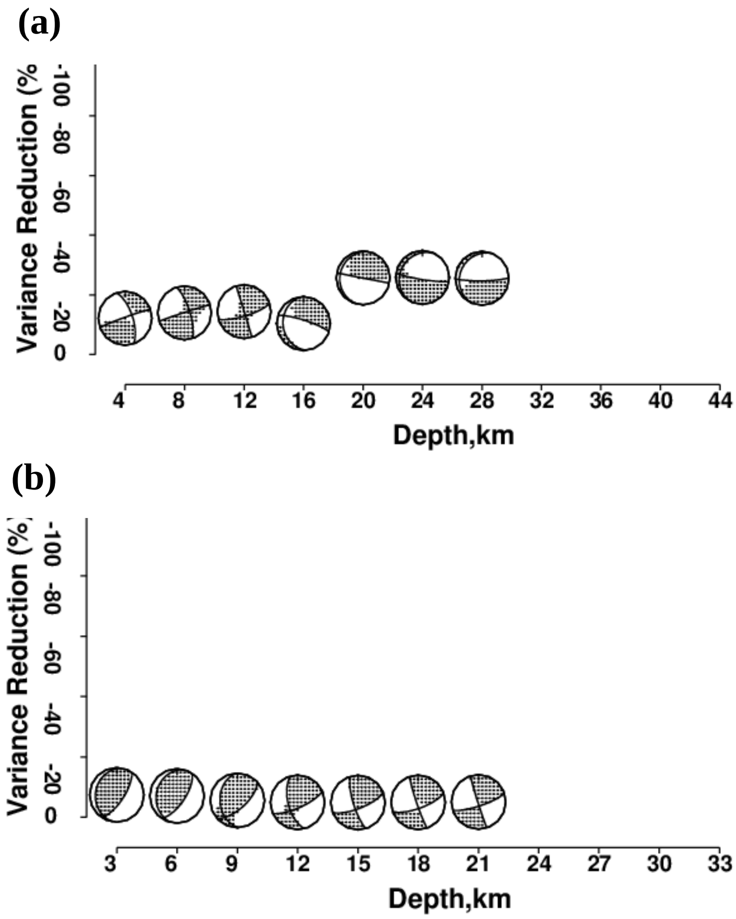

Figure 4.2. Example of two inaccurate CMT solution. (a) The variance reduction versus depth plot of 26.05.2014 earthquake (Mw3.5), (b) 25.05.2014 earthquake (Mw3.6).

The earthquakes in the dataset are relocated and their fault plane solution is retrieved using the CMT technique developed by Kuge as illustrated in the scheme in Data Analysis part. The solutions obtained by inversion are then controlled in terms of variance reduction and fault plane variations versus source depth. 88 out of 187 unreliable solutions are eliminated from generated CMT catalogue.

The CMT inversion is mainly carried out using broadband records and the results are given in Table 4.1 and Figure 4.3. For the case of May 24th, 2014 Mw 6.8 Gökçeada earthquake, where the near-source broadband seismometers are clipped, the moment tensor inversion is carried out using acceleration data (see Appendix).

Table 4.1. Source parameters of 99 events obtained by CMT inversion method H= CMT depth in km.

No.	Location	Date	Time	Latitude	Longitude	M_W	H	Strike	Dip	Rake
1	Asmalı-Balıkesir-Marmara Sea	19.04.2004	15.27	40.61	27.70	3.7	15	101	69	135
2	Gulf of İzmit	16.05.2004	03:30	40.72	29.33	4.3	3	94	72	-111
3	Çınarcık Offshore-Yalova	29.09.2004	15:42	40.79	29.02	3.8	6	85	67	82
4	Gulf of Gemlik-Marmara Sea	24.10.2006	14:00	40.42	28.99	4.9	9	97	45	-88
5	Samanlı-Yalova	28.10.2006	15:28	40.64	29.23	3.4	6	248	72	-119
6	Şenköy-Çınarcık	12.03.2008	18:53	40.62	29.01	4.4	9	89	78	-129
7	Şenköy-Çınarcık	05.10.2008	06:04	40.63	29.01	3.8	9	89	51	-117
8	Yalova Offshore-Marmara Sea	22.10.2008	01:00	40.74	29.17	3.7	3	110	70	-154
9	Ericek-Bolu	12.11.2008	11:57	40.78	31.92	3.9	12	251	71	135
10	Aşağıkuzören-Bolu	12.11.2008	14:25	40.81	31.96	3.7	9	251	73	123
11	Kozlu-Bolu	16.08.2010	03:09	40.83	31.58	3.7	3	83	89	179
12	Tuzla-Marmara Sea	09.05.2011	03:01	40.85	29.29	3.2	6	281	63	-121
13	Kızılağıl-Bolu	13.05.2011	22:28	40.77	31.53	3.9	4	302	66	-160
14	Marmara Sea	25.07.2011	17:57	40.81	27.74	4.9	6	255	81	153
15	Kaleköy-Gökçeada	31.07.2013	01:26	40.31	25.80	3.8	9	238	86	-157
16	Biga-Çanakkale	29.08.2013	06:20	40.35	27.45	3.9	12	66	65	172
17	Şarköy-Tekirdağ	25.09.2013	13:39	40.77	27.42	3.2	10	241	53	124
18	Gulf of Saros-Aegean Sea	25.10.2013	12:01	40.41	26.06	3.6	9	119	35	-97
19	Aegean Sea	23.11.2013	10:27	40.58	25.69	3.6	10	96	39	-91
20	Ulumescit-Bolu	24.11.2013	20:49	40.78	31.88	4.7	6	74	27	110
21	Gelibolu-Çanakkale	22.04.2014	18:27	40.46	26.46	3.3	6	77	30	-81
22	Gulf of Saros-Aegean Sea	24.05.2014	15:01	40.38	26.14	3.9	9	66	37	-101
23	Aegean Sea	24.05.2014	16:34	40.29	25.63	3.8	9	93	64	-94
24	Gulf of Saros-Aegean Sea	25.05.2014	01:50	40.40	25.92	3.5	6	107	57	-106
25	Gulf of Saros-Aegean Sea	25.05.2014	05:44	40.42	26.07	3.9	9	102	60	-108
26	Gulf of Saros-Aegean Sea	25.05.2014	11:47	40.41	26.09	4.2	2	79	40	171
27	Kaleköy-Gökçeada	27.05.2014	11:42	40.36	25.88	3.5	8	80	87	166
28	Gulf of Saros-Aegean Sea	28.05.2014	03:59	40.42	26.13	4.3	6	80	12	-111
29	Termal-Yalova	03.08.2014	10:42	40.61	29.16	3.5	4	109	41	-70
30	Termal-Yalova	03.08.2014	22:22	40.61	29.17	3.9	3	118	43	-62
31	Şarköy-Marmara Sea	04.11.2005	20:12	40.68	27.30	3.7	6	202	52	110
32	Şarköy-Marmara Sea	18.08.2007	07:37	40.64	27.25	3.4	3	99	76	-136
33	Biga-Çanakkale	12.04.2008	03:25	40.38	27.42	3.4	12	273	86	165
34	Şarköy-Marmara Sea	14.07.2008	16:02	40.74	27.36	3.3	10	56	70	110

35	Marmara Sea	23.01.2009	16:34	40.79	27.77	3.5	15	163	36	-140
36	Marmara Sea	18.03.2009	16:33	40.80	27.76	3.8	9	277	74	175
37	Marmara Sea	27.04.2009	19:03	40.73	27.53	4.0	12	261	43	-160
38	Marmara Sea	25.10.2009	03:26	40.79	27.76	3.6	12	144	41	-124
39	Çınarcık Offshore-Yalova	23.06.2002	23.09	40.76	29.03	2.7	3	340	66	-78
40	Çınarcık Offshore-Yalova	22.07.2003	23:55	40.73	29.07	3.0	2	110	45	-137
41	Çiftlikköy-Yalova	16.05.2004	21:07	40.70	29.31	3.3	5	100	48	-128
42	Çınarcık Offshore-Yalova	29.09.2004	15:51	40.78	29.04	2.7	20	291	57	-163
43	Çınarcık Offshore-Yalova	14.08.2005	21:11	40.74	29.04	3.4	4	315	58	-97
44	Çınarcık Offshore-Yalova	07.09.2005	13:22	40.73	29.22	3.3	9	281	70	-135
45	Çınarcık Offshore-Yalova	07.09.2005	13:50	40.74	29.25	3.2	9	290	48	-127
46	Çınarcık-Yalova	26.11.2005	22:27	40.65	29.07	3.2	6	292	56	-109
47	Çınarcık-Yalova	18.08.2008	11:06	40.71	29.12	3.0	12	248	56	-175
48	Çınarcık-Yalova	18.08.2008	11:08	40.72	29.12	3.1	10	265	64	-160
49	Çınarcık Offshore-Yalova	21.02.2009	22:29	40.76	29.05	3.3	6	303	53	-112
50	Çınarcık Offshore-Yalova	21.02.2009	23:04	40.73	29.02	3.4	6	294	63	-111
51	Koru-Çınarcık-Yalova	12.07.2009	06:59	40.67	29.17	3.3	8	253	36	-120
52	Şenköy- Çınarcık-Yalova	16.11.2009	18:47	40.60	29.01	3.2	12	88	41	-140
53	Marmara Sea	14.03.2012	09:25	40.81	28.79	3.7	10	347	49	-124
54	Lapseki-Çanakkale	04.05.2012	05:38	40.310	27.00	3.9	6	273	45	-162
55	Biga-Çanakkale	16.12.2014	09:02	40.149	27.083	4.1	12	261	85	174
56	Kuş Lake-Balıkesir	03.07.2014	05:04	40.208	27.933	4.3	9	79	86	147
57	Manyas-Balıkesir	30.03.2011	17:07	40.048	27.831	4.0	12	81	76	177
58	Gulf of Bandırma	09.03.2011	07:04	40.431	28.059	3.8	9	75	77	-120
59	Bayraktar-İzmit	01.08.2007	19:03	40.786	30.090	3.7	12	91	57	113
60	Enez-Edirne	20.05.2011	22:34	40.881	26.003	3.4	6	99	79	-176
61	Geyve-Sakarya	22.10.2014	17:11	40.406	30.114	4.2	6	66	38	-161
62	Kaynaşlı-Düzce	07.07.2015	05:08	40.820	31.291	3.7	15	322	70	-120
63	İnhisar-Bilecik	28.06.2014	01:39	40.085	30.385	3.8	6	210	30	-149
64	Tekirdağ Offshore-Marmara	01.02.2015	10:46	40.696	27.505	3.0	6	67	61	128
65	Biga-Çanakkale	16.12.2014	09:03	40.156	27.086	3.5	20	76	67	163
66	Mustafakemalpaşa-Bursa	23.01.2015	10:19	40.065	28.590	4.2	2	67	44	-135
67	Akyazı-Sakarya	31.05.2004	22:50	40.510	30.600	3.7	15	96	38	-101
68	Asmalı-Balıkesir	16.01.2005	09:57	40.609	27.723	3.2	9	246	77	-155
69	Gulf of Saros-Aegean Sea	09.04.2005	19:28	40.484	25.814	3.6	6	186	76	115
70	Biga-Çanakkale	27.07.2014	14:09	40.178	26.891	3.4	12	192	85	150
71	Aegean Sea	28.05.2014	10:31	40.282	25.482	3.5	9	30	68	-177
72	Güzelköy Offshore-Tekirdağ	27.06.2005	02:58	40.692	27.387	3.4	6	121	23	-129
73	Mürefte Offshore-Tekirdağ	01.06.2014	21:17	40.561	27.334	3.2	6	250	72	-172
74	Engurucuk-Gemlik	11.05.2015	04:16	40.415	29.125	3.5	8	265	59	-121
75	Kaleköy-Gökçeada	26.05.2014	18:54	40.400	25.894	3.5	10	272	79	-87

76	Gulf of Gemlik-Marmara Sea	27.10.2012	02:37	40.435	28.727	3.7	6	257	65	-130
77	Kaleköy-Gökçeada	30.07.2013	06:28	40.302	25.774	3.8	9	241	59	-156
78	Gulf of Gemlik-Marmara Sea	26.10.2012	03:37	40.425	28.720	3.6	9	251	75	-155
79	Güzelköy Offshore-Tekirdağ	27.03.2005	09:32	40.737	27.408	3.5	9	250	80	159
80	Aegean Sea	30.05.2014	05:21	40.188	25.554	3.6	6	224	87	-119
81	Gölyaka-Düzce	13.09.2004	01:48	40.790	30.990	3.4	2	230	15	-108
82	Gulf of Saros	17.06.2004	12:48	40.490	26.110	2.8	9	112	62	-119
83	Gulf of Gemlik-Marmara Sea	11.10.2004	01:25	40.430	28.940	3.6	20	253	48	-164
84	Kocadere-Çanakkale	24.07.2015	01:26	40.242	26.302	4.3	4	33	88	168
85	Kumbağ-Tekirdağ	13.07.2003	05:09	40.830	27.400	3.6	20	229	55	129
86	Kuş Lake	09.06.2003	17:44	40.210	27.940	4.4	12	263	90	-138
87	Güzelköy Offshore-Tekirdağ	20.08.2005	06:09	40.760	27.425	3.5	20	40	76	168
88	Akyazı-Sakarya	17.09.2002	12:05	40.720	30.610	3.8	16	262	52	-110
89	Biga-Canakkale	03.06.2008	06:59	40.163	26.918	3.5	9	116	61	133
90	Marmara Sea	03.10.2010	17:49	40.840	28.140	4.1	9	79	86	-178
91	Mürefte Offshore-Tekirdağ	12.05.2008	15:11	40.634	27.373	3.6	18	273	82	161
92	Marmara Ereğlisi Offshore-Tekirdağ	12.08.2008	15:41	40.834	27.956	3.3	6	93	74	-161
93	Marmara Sea	24.01.2009	15:58	40.785	27.764	4.0	9	137	36	-119
94	Marmara Sea	25.07.2011	20:43	40.816	27.733	3.6	5	247	78	-169
95	Marmara Ereğlisi Offshore-Tekirdağ	07.06.2012	20:54	40.854	27.923	4.9	5	89	85	173
96	Marmara Ereğlisi Offshore-Tekirdağ	12.08.2008	15:41	40.834	27.856	3.0	9	113	78	-175
97	Marmara Ereğlisi Offshore-Tekirdağ	27.11.2013	04:13	40.845	27.918	4.6	5	86	77	171
98	Marmara Sea	28.10.2015	16:20	40.820	27.764	4.3	6	246	69	160
99	Aegean Sea	24.05.2014	09:25	40.290	25.400	6.8	18	76	85	173

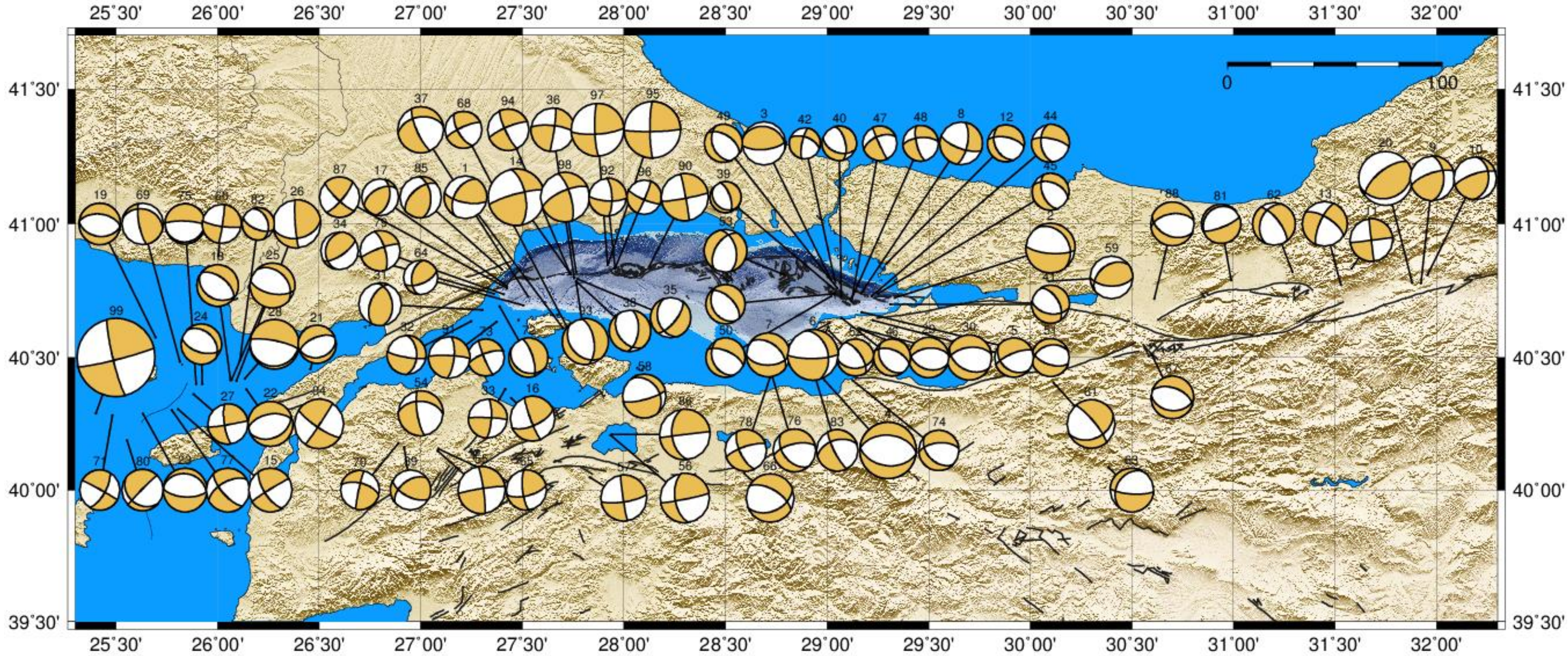

Figure 4.3. The moment tensor inversion results of the events around Marmara region.

4.1.1. Ganos Area

The first remarkable finding of this study is related with the segmentation and bending between the Ganos Fault and Tekirdag Basin.

In the west, between the Ganos Fault and Tekirdag Basin, along with the strike-slip faulting mechanism, the CMT inversion results show significant number of events having reverse faulting mechanism with NW trending compressional stress, which is consistent with the fault plane solution of the 27 April 1985 Mürefte earthquake (M=4.4) located in the Ganos Mountain (Figure 4.4).

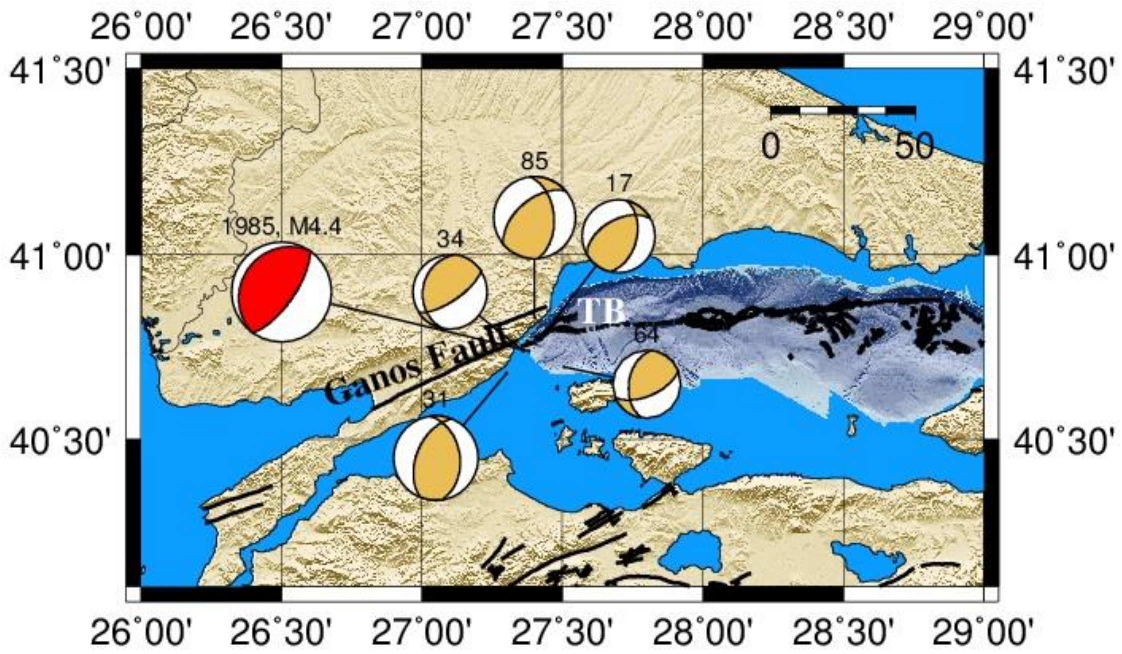

Figure 4.4. CMT inversion results having reverse faulting mechanism between the Ganos Fault and Tekirdag Basin. The solution of 1985 Mürefte Earthquake by Kalafat, 1995 is given in red. Symbol sizes are proportional to magnitudes, TB: Tekirdag Basin.

4.1.2. Eastern Marmara Segment

As for the Çinarcik Basin, the observed various types of focal mechanisms as strike-slip, normal faulting and reverse faulting mechanism may result from the presence of a segmented fault system where restraining local stresses are developed (Figure 4.5).

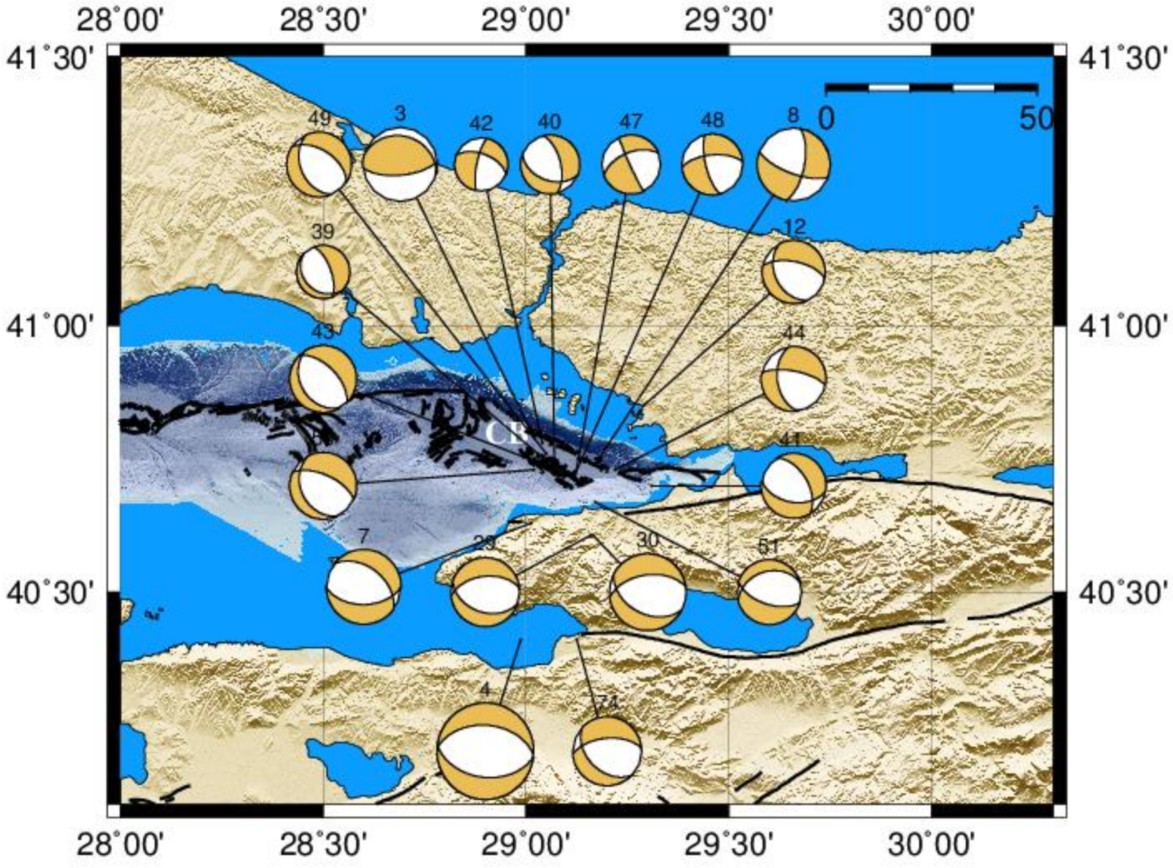

Figure 4.5. CMT inversion results in the Cinarcik Basin. Symbol sizes are proportional to magnitudes, CB: Cinarcik Basin.

Another remarkable seismotectonic feature is observed in eastern Marmara region inferred from the focal mechanisms taking place in Yalova-Çınarcık and Çınarcık basin locations. Despite the proximity of the two locations, the focal mechanisms in Yalova-Çınarcık region show predominantly N-S extension while the Çınarcık basin events show NE-SW extension. That is to say the stress fields to the north of NAF and the stress field to the south of NAF is rotated by about 45 degree.

4.1.3. Northern Aegean Sea Area

Besides the aftershocks of May 24th, 2014 Mw6.5 Gökçeada Earthquake (99, in Figure 4.6) with strike-slip mechanisms (26, 27, 71, 80 in Figure 4.6), several events showing predominantly normal faulting mechanisms (22, 23, 24, 25, 28 in Figure 4.6) were determined in the source region of the 2014 Northern Aegean earthquake.

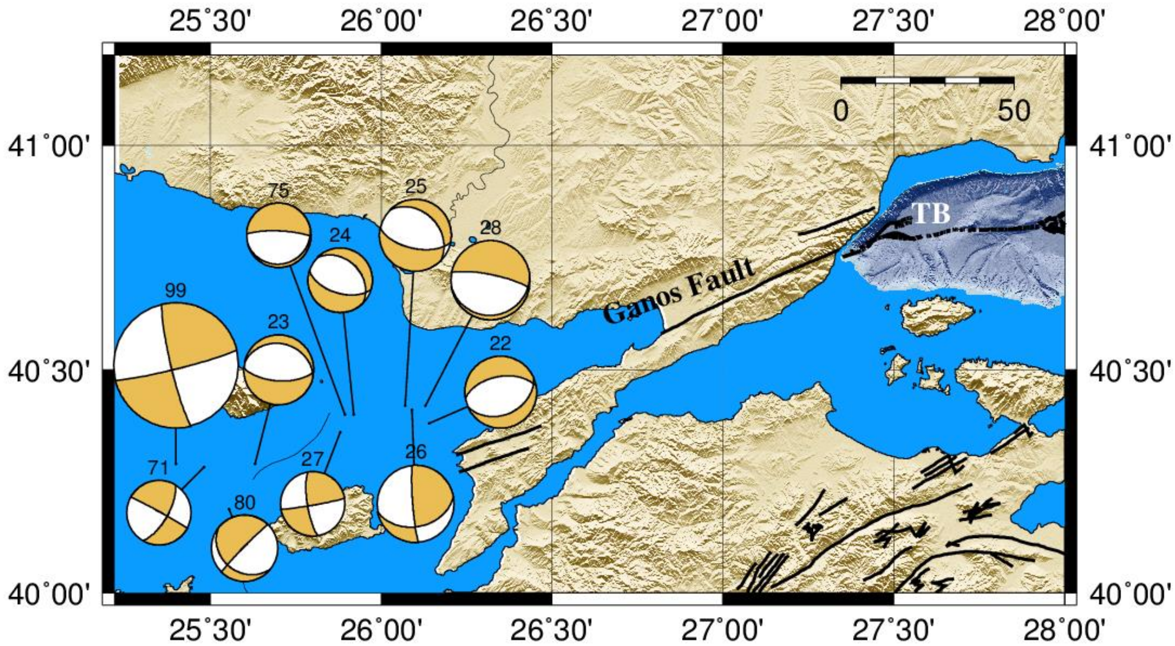

Figure 4.6. CMT inversion results in the Northern Aegean Sea. Symbol sizes are proportional to magnitudes.

4.1.4. NAF Near Bolu City

The detection of three earthquakes having pure reverse and reverse with minor strike-slip component faulting mechanisms that occurred 4 km away from the major dextral NAFZ near Bolu city is another remarkable finding of this study. Existence of NAF as one and only active major fault in the region beside local faults set us thinking that tectonic activity along the NAF and the Pontides are related with each other. The ongoing tectonism and seismicity along the NAF may result in stress accumulation along the surrounding zones forced by the shears on NAF and thus trigger the tectonic evolution of thrusts and strike slip faulting in the northern region of NAF. Both the focal mechanisms of the reverse and reverse with minor strike-slip faulting types show maximum compressional direction oriented NW-SE. This stress regime is consistent also with the focal mechanism of the 1968 Bartin earthquake (Mw=6.5) which is a strong evidence for the relation between the driving forces of the tectonics along NAF and Pontides (Figure 4.7).

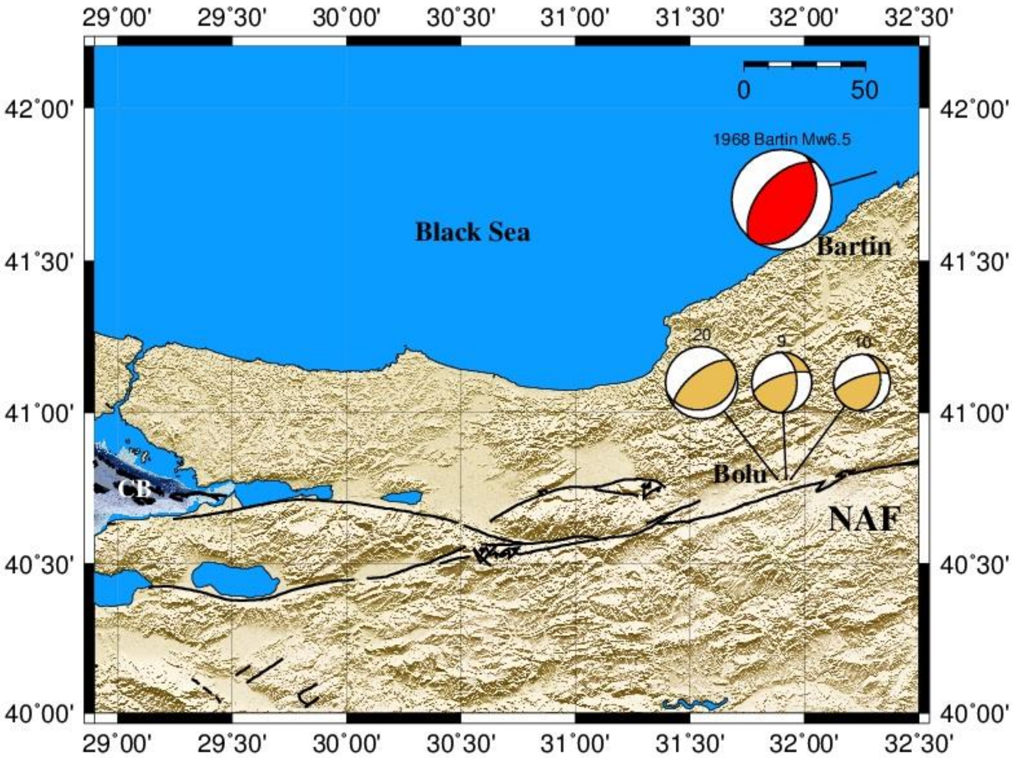

Figure 4.7. CMT inversion results of three earthquakes having pure reverse and reverse with minor strike-slip component faulting mechanisms in Bolu city. Symbol sizes are proportional to magnitudes. NAF: North Anatolian Fault.

4.2. Simultaneous Inversion of First Motion Polarity Data Results

Simultaneous inversion of the first motion polarities of cluster of earthquakes taking place within the same stress regime are performed to obtain focal mechanism of the individual events constituting the cluster. For this purpose, Horiuchi et al. (1995) method is first performed for all events in the Sea of Marmara and the results are given in Table 4.2 and Figure 4.8. Then performed separately for cluster of events occurred in Ganos Area, Western Marmara Segment and Central Marmara Segment which are different in geometry, length and seismic activity. The focal mechanisms and the list of the focal mechanism parameters are given in each subsection.

The number of inconsistent stations for all cases of the theoretical focal mechanisms is calculated with intervals of 5 degrees. This calculation is made for all observed events. Then the parameters determining the stress tensor is calculated where the number of the inconsistent stations is minimum.

Table 4.2. Focal mechanism parameters derived from simultaneous inversion of the polarity data acquired in the Sea of Marmara.

No.	**Date**	**Time**	**Latitude**	**Longitude**	**M_W**	**H**	**Strike**	**Dip**	**Rake**	**Number of Stations**
1	18.04.2013	19:36	40.75	27.40	3.0	9.8	170	45	-104	23 Land Stations
2	28.07.2013	17:45	40.76	27.45	2.9	15.7	140	51	-140	25 Land Stations
3	17.08.2013	03:37	40.76	27.42	3.1	8.7	300	45	-75	17 Land Stations
4	25.09.2013	13:39	40.77	27.42	3.5	7.5	350	39	16	24 Land Stations
5	08.12.2013	03:51	40.75	27.38	2.8	15.0	30	30	-7	16 Land Stations
6	22.02.2014	22:45	40.78	27.45	3.2	14.3	303	26	-36	16 Land Stations
7	11.04.2014	12:59	40.80	27.51	3.0	13.3	337	20	15	17 Land Stations
8	27.04.2014	07:13	40.77	27.36	3.1	8.6	231	67	175	24 Land Stations
9	04.05.2014	12:45	40.77	27.37	2.7	7.3	347	35	18	12 Land Stations
10	19.06.2014	21:14	40.65	27.53	2.9	8.7	161	36	-46	22 Land Stations
11	20.06.2014	22:21	40.71	27.47	2.8	9.1	330	45	-49	22 Land Stations
12	17.09.2014	12:20	40.78	27.42	2.7	16.2	270	60	-148	13 Land Stations
13	07.10.2014	23:49	40.78	27.56	2.8	12.4	350	45	-38	21 Land Stations
14	08.10.2014	03:08	40.76	27.49	3.3	19.2	270	60	-148	24 Land Stations
15	23.10.2014	14:53	40.74	27.39	3.4	8.7	120	45	-121	21 Land Stations
16	03.12.2014	05:39	40.73	27.31	2.8	10.7	293	18	-35	13 Land Stations

17	01.02.2015	10:46	40.70	27.51	3.5	5.6	330	30	-46	19 Land Stations
18	04.10.2015	00:24	40.75	27.38	3.0	16.6	357	65	22	21 Land Stations
19	25.10.2015	15:58	40.80	27.43	2.7	14.9	140	45	-113	11 OBS+15 Land Stations
20	04.12.2015	06:52	40.74	27.44	2.9	7.1	75	76	-175	11 OBS+13 Land Stations
21	07.12.2015	12:02	40.71	27.43	3.3	5.2	347	35	18	12 OBS+22 Land Stations
22	26.12.2015	22:31	40.68	27.46	2.7	9.4	338	48	-60	15 Land Stations
23	19.01.2016	13:09	40.72	27.43	2.6	7.6	293	18	-35	6 OBS+11 Land Stations
24	19.01.2016	13:10	40.71	27.42	2.4	9.8	130	45	-117	4 OBS+10 Land Stations
25	11.02.2016	01:53	40.56	27.34	3.4	14.1	75	30	-162	27 Land Stations
26	15.04.2016	09:05	40.79	27.47	3.1	13.8	348	30	44	11 OBS+21 Land Stations
27	26.07.2015	06:47	40.88	27.55	2.8	16.1	225	10	180	14 OBS Stations
28	05.08.2015	06:31	40.76	27.36	2.7	12.2	150	30	-127	11 OBS Stations
29	24.08.2015	04:47	40.83	28.27	2.6	5.3	90	15	139	10 OBS Stations
30	29.08.2015	12:47	40.87	27.92	3.9	15.4	193	70	-11	12 OBS Stations
31	29.08.2015	18:14	40.86	27.92	2.2	14.2	36	25	12	11 OBS Stations
32	04.09.2015	13:18	40.72	27.40	2.4	9.7	300	39	-52	10 OBS Stations
33	13.09.2015	05:11	40.80	27.68	2.3	17.6	186	75	-5	10 OBS Stations
34	17.09.2015	21:39	40.84	28.30	2.3	6.9	90	25	-174	10 OBS Stations
35	19.09.2015	18:49	40.80	28.02	2.4	17.9	180	5	-155	10 OBS Stations
36	01.10.2015	10:45	40.84	27.71	2.6	19.3	0	40	-32	10 OBS Stations
37	01.10.2015	16:38	40.81	29.00	2.7	6.9	243	50	-140	10 OBS Stations
38	16.10.2015	02:00	40.80	27.79	2.3	18.8	165	30	-123	11 OBS Stations
39	28.10.2015	16:20	40.83	27.73	4.6	14.6	65	47	-152	13 OBS Stations
40	28.10.2015	16:22	40.84	27.75	2.7	11.6	270	10	-83	10 OBS Stations
41	28.10.2015	18:43	40.83	27.72	2.1	12.1	315	30	-58	10 OBS Stations
42	28.10.2015	21:50	40.82	27.72	2.2	12.1	36	25	12	11 OBS Stations
43	31.10.2015	21:10	40.86	28.78	2.8	11.9	360	25	-21	10 OBS Stations
44	02.112015	10:33	40.53	27.96	1.9	13.8	180	5	-155	10 OBS Stations
45	02.11.2015	18:32	40.84	27.73	2.2	19.9	277	65	-161	10 OBS Stations
46	10.11.2015	11:23	40.80	27.89	2.2	14.5	90	5	113	11 OBS Stations
47	01.11.2015	11:26	40.79	27.89	2.8	16.0	90	62	-169	12 OBS Stations
48	16.11.2015	15:45	40.89	28.76	4.2	11.6	334	35	-45	14 OBS Stations
49	16.11.2015	16:36	40.90	28.74	3.2	10.3	158	20	-142	12 OBS Stations
50	16.11.2015	17:04	40.90	28.76	3.7	9.4	206	35	-118	14 OBS Stations
51	16.11.2015	18:13	40.90	28.74	2.9	9.0	144	25	-138	11 OBS Stations
52	17.11.2015	02:17	40.89	28.77	3.3	9.4	230	45	-130	12 OBS Stations

53	17.11.2015	03:05	40.92	28.74	2.5	9.4	150	15	-157	10 OBS Stations
54	17.11.2015	04:36	40.89	28.74	3.4	12.2	0	10	-1	11 OBS Stations
55	18.11.2015	12:52	40.87	28.76	3.4	12.3	349	40	-37	13 OBS Stations
56	24.11.2015	05:40	40.86	28.97	2.3	7.6	338	39	-52	10 OBS Stations
57	24.11.2015	05:55	40.79	29.03	3.1	3.0	30	15	26	10 OBS Stations
58	25.11.2015	09:34	40.80	27.89	1.8	14.1	90	30	-154	10 OBS Stations
59	28.11.2015	03:10	40.82	27.43	2.0	12.1	270	10	-83	10 OBS Stations
60	28.11.2015	06:41	40.79	27.90	3.2	16.2	180	80	-1	12 OBS Stations
61	30.11.2015	16:09	40.77	27.47	2.7	15.3	36	25	12	10 OBS Stations
62	03.12.2015	03:27	40.86	27.47	2.3	13.2	30	15	26	10 OBS Stations
63	07.12.2015	20:57	40.70	27.35	3.9	11.3	0	0	16	13 OBS Stations
64	22.12.2015	15:10	40.83	27.76	2.8	17.3	276	70	169	12 OBS Stations
65	03.01.2016	17:46	40.74	28.05	2.9	15.9	30	15	26	11 OBS Stations
66	06.10.2016	15:44	40.73	28.05	3.3	16.5	120	45	-121	13 OBS Stations
67	06.10.2016	16:04	40.73	28.05	3.0	16.9	0	40	-32	12 OBS Stations
68	06.10.2016	19:12	40.87	27.42	2.6	9.3	283	70	178	10 OBS Stations
69	12.01.2016	01:48	40.83	27.73	3.1	12.2	240	15	-107	13 OBS Stations
70	16.11.2016	21:33	40.72	27.41	2.4	9.4	62	63	-163	10 OBS Stations
71	28.01.2016	15:06	40.76	28.08	2.5	16.0	349	40	-37	13 OBS Stations
72	30.01.2016	09:03	40.76	28.07	3.8	16.9	347	35	-36	13 OBS Stations
73	30.01.2016	16:33	40.83	28.27	2.5	5.2	262	55	-141	11 OBS Stations
74	01.02.2016	18:38	40.76	28.08	2.9	16.1	360	30	-25	11 OBS Stations
75	05.02.2016	08:02	40.83	28.34	3.2	11.7	350	32	-19	13 OBS Stations
76	12.02.2016	17:43	40.85	28.55	2.5	7.9	15	30	-16	12 OBS Stations
77	19.02.2016	10:37	40.90	28.67	2.5	8.6	249	65	165	11 OBS Stations
78	24.02.2016	04:26	40.85	27.71	2.2	20.4	9	47	14	12 OBS Stations
79	29.02.2016	04:52	40.83	28.15	2.2	13.8	357	65	22	11 OBS Stations
80	01.03.2016	14:54	40.86	27.75	2.7	22.0	276	70	169	13 OBS Stations
81	10.03.2016	14:47	40.82	28.07	2.5	16.6	186	75	-5	11 OBS Stations
82	11.03.2016	18:40	40.82	28.08	2.2	15.7	94	79	170	12 OBS Stations
83	23.03.2016	03:51	40.86	27.95	3.1	17.2	2	69	22	12 OBS Stations
84	24.03.2016	08:04	40.85	27.95	3.7	18.0	270	65	-174	13 OBS Stations
85	25.03.2016	22:18	40.85	27.99	2.2	16.6	75	88	180	10 OBS Stations
86	27.03.2016	05:03	40.83	27.87	3.2	23.4	150	30	-127	13 OBS Stations
87	27.03.2015	05:03	40.83	27.87	3.9	22.5	0	50	-36	11 OBS Stations
88	27.03.2016	05:05	40.82	27.86	2.5	22.0	13	35	-23	10 OBS Stations
89	28.03.2016	17:23	40.74	27.50	4.1	16.2	0	0	16	13 OBS Stations
90	01.04.2016	23:22	40.85	27.97	2.3	24.4	160	51	-40	12 OBS Stations
91	06.04.2016	04:34	40.87	27.91	2.5	14.5	289	70	-164	12 OBS Stations
92	25.04.2016	01:51	40.83	28.42	1.9	6.8	138	42	-59	10 OBS Stations
93	27.04.2016	12:07	40.41	28.68	3.6	11.7	262	27	-158	10 OBS Stations
94	02.05.2016	12:21	40.72	27.37	2.0	8.4	90	15	139	10 OBS Stations

95	31.05.2016	21:14	40.84	28.23	3.4	7.5	330	15	-36	13 OBS Stations
96	31.05.2016	21:17	40.85	28.23	2.2	7.3	358	33	-9	11 OBS Stations
97	01.06.2016	12:32	40.84	28.23	2.3	7.1	111	40	-88	11 OBS Stations
98	02.06.2016	03:56	40.84	28.24	2.3	7.4	111	40	-88	10 OBS Stations
99	03.06.2016	03:06	40.85	28.23	2.4	7.6	320	42	-49	12 OBS Stations
100	05.06.2016	20:49	40.85	27.94	2.2	17.0	276	70	169	11 OBS Stations
101	15.06.2016	05:20	40.84	28.23	3.5	7.0	300	15	-62	12 OBS Stations
102	17.06.2016	06:35	40.84	28.23	2.3	7.0	330	15	-36	10 OBS Stations

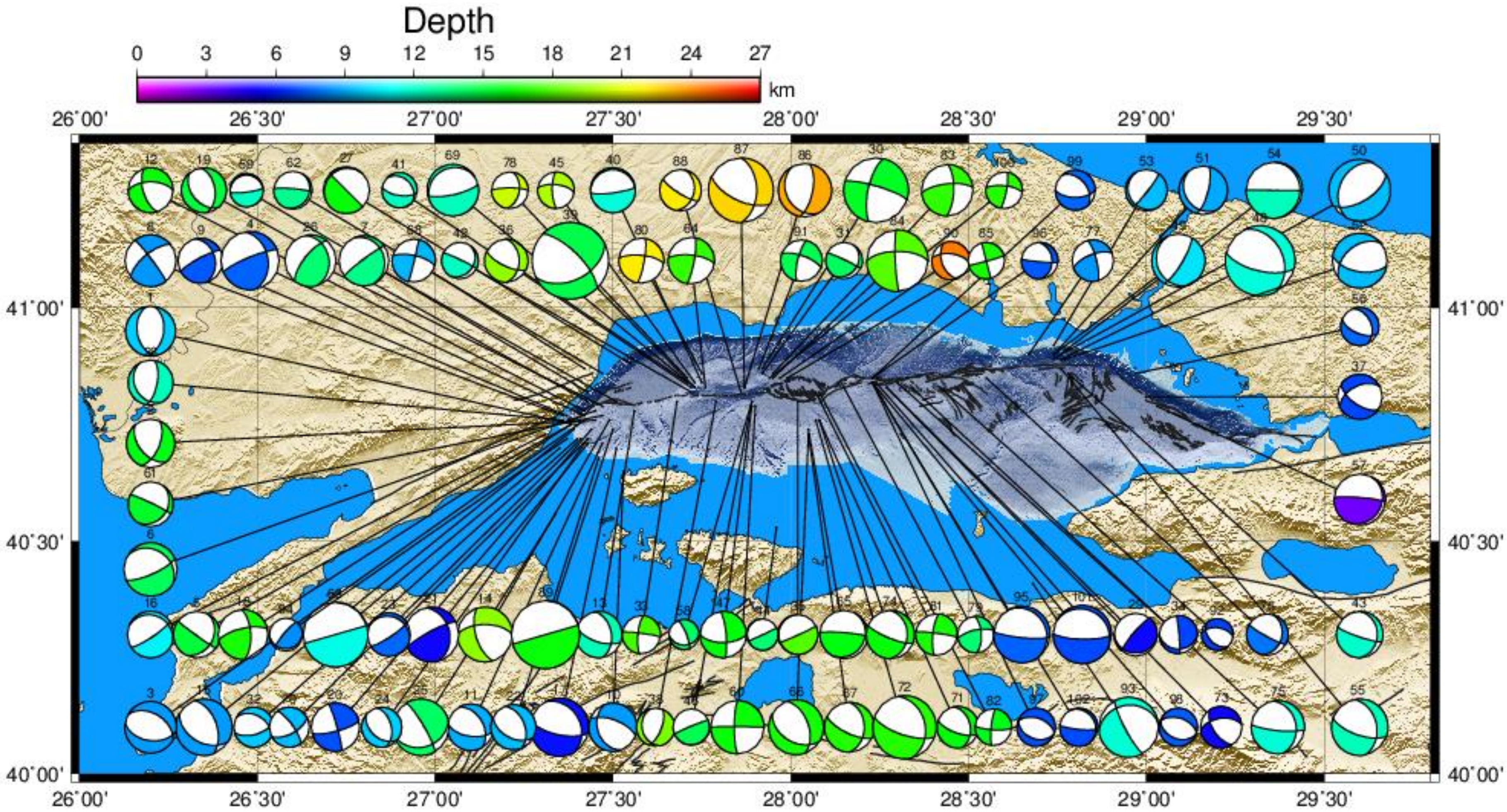

Figure 4.8. Focal mechanism derived from simultaneous inversion of the polarity data acquired in the Sea of Marmara.

4.2.1. Ganos Area

The data acquired in Ganos area include 37 events with magnitudes between 2.0 and 4.1. As mentioned in Section 3.3.2, since some events are recorded by less than 10 OBS stations, in order to increase the number of polarities and improve the azimuthal and take-off coverage, the OBS stations are integrated with the land seismic stations operated by KOERI. For this cluster in total 645 P-wave polarities are used in order to determine focal mechanisms. The focal mechanisms and list of the focal mechanism parameters are shown in Figure 4.9 and Table 4.3, respectively.

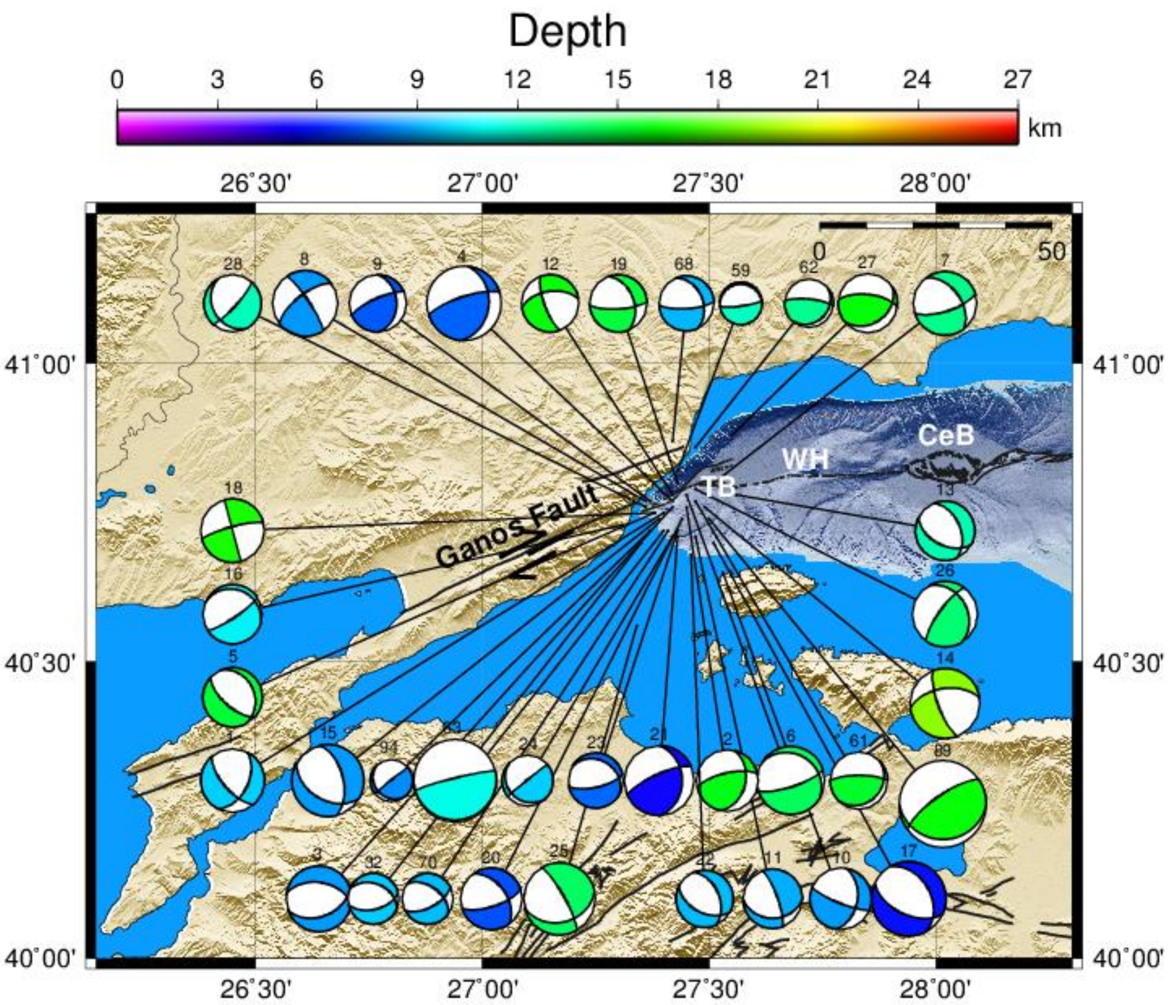

Figure 4.9. Focal mechanism derived from simultaneous inversion of the polarity data acquired in Ganos Area.

Between the Ganos Fault and Tekirdag Basin, along with the strike-slip and normal faulting mechanism, the results show significant number of events having reverse faulting mechanism with NW trending compressional stress which are consistent with the results obtained from CMT analysis. The hypocenter locations of the events occurred in Ganos area changes between about 5 km to 19 km depth.

Table 4.3. Focal mecahnism parameters derived from simultaneous inversion of the polarity data acquired in Ganos Area.

Event number	**Date**	**Time**	**Lat.**	**Lon.**	**M_W**	**H**	**Strike**	**Dip**	**Rake**	**Number of Stations**
1	18.04.2013	19:36	40.75	27.40	3.0	9.8	27	50	-32	23 Land Stations
2	28.07.2013	17:45	40.76	27.45	2.9	15.7	12	40	31	25 Land Stations
3	17.08.2013	03:37	40.76	27.42	3.1	8.7	70	45	-111	17 Land Stations
4	25.09.2013	13:39	40.77	27.42	3.5	7.5	5	33	27	24 Land Stations
5	08.12.2013	03:51	40.75	27.38	2.8	15.0	336	27	-67	16 Land Stations
6	22.02.2014	22:45	40.78	27.45	3.2	14.3	301	22	-42	16 Land Stations
7	11.04.2014	12:59	40.80	27.51	3.0	13.3	324	50	-26	17 Land Stations
8	27.04.2014	07:13	40.77	27.36	3.1	8.6	232	68	169	24 Land Stations
9	04.05.2014	12:45	40.77	27.37	2.7	7.3	358	34	27	12 Land Stations
10	19.06.2014	21:14	40.65	27.53	2.9	8.7	10	44	-16	22 Land Stations
11	20.06.2014	22:21	40.71	27.47	2.8	9.1	90	35	-156	22 Land Stations
12	17.09.2014	12:20	40.78	27.42	2.7	16.2	261	55	-159	13 Land Stations
13	07.10.2014	23:49	40.78	27.56	2.8	12.4	337	47	-60	21 Land Stations
14	08.10.2014	03:08	40.76	27.49	3.3	19.2	261	55	-159	24 Land Stations
15	23.10.2014	14:53	40.74	27.39	3.4	8.7	120	45	-126	21 Land Stations
16	03.12.2014	05:39	40.73	27.31	2.8	10.7	292	17	-35	13 Land Stations
17	01.02.2015	10:46	40.70	27.51	3.5	5.6	331	41	-60	19 Land Stations
18	04.10.2015	00:24	40.75	27.38	3.0	16.6	255	79	180	21 Land Stations
19	25.10.2015	15:58	40.80	27.43	2.7	14.9	340	45	-22	11 OBS+15 Land Stations
20	04.12.2015	06:52	40.74	27.44	2.9	7.1	324	50	-26	11 OBS+13 Land Stations
21	07.12.2015	12:02	40.71	27.43	3.3	5.2	358	34	27	12 OBS+22 Land Stations
22	26.12.2015	22:31	40.68	27.46	2.7	9.4	337	47	-60	15 Land Stations
23	19.01.2016	13:09	40.72	27.43	2.6	7.6	299	26	-50	6 OBS+11 Land Stations
24	19.01.2016	13:10	40.71	27.42	2.4	9.8	135	20	173	4 OBS+10 Land Stations

25	11.02.2016	01:53	40.56	27.34	3.4	14.1	75	35	-160	27 Land Stations
26	15.04.2016	09:05	40.79	27.47	3.1	13.8	330	33	28	11 OBS+21 Land Stations
27	26.07.2015	06:47	40.88	27.55	2.8	16.1	54	32	52	14 OBS Stations
28	05.08.2015	06:31	40.76	27.36	2.7	12.2	150	30	-159	11 OBS Stations
32	04.09.2015	13:18	40.72	27.40	2.4	9.7	292	40	-61	10 OBS Stations
59	28.11.2015	03:10	40.82	27.43	2.0	12.1	270	10	-82	10 OBS Stations
61	30.11.2015	16:09	40.77	27.47	2.7	15.3	45	20	46	10 OBS Stations
62	03.12.2015	03:27	40.86	27.47	2.3	13.2	49	21	45	10 OBS Stations
63	07.12.2015	20:57	40.70	27.35	3.9	11.3	89	5	103	13 OBS Stations
68	06.10.2016	19:12	40.87	27.42	2.6	9.3	337	40	-24	10 OBS Stations
70	16.11.2016	21:33	40.72	27.41	2.4	9.4	305	50	-37	10 OBS Stations
89	28.03.2016	17:23	40.74	27.50	4.1	16.2	90	20	123	13 OBS Stations
94	02.05.2016	12:21	40.72	27.37	2.0	8.4	135	20	173	10 OBS Stations

4.2.2. Western Marmara Segment

The data acquired in Western Marmara Segment include 38 events with magnitudes between 1.8 and 4.6. For this cluster in total 434 P-wave polarities are used to determine focal mechanisms. The focal mechanisms and list of the focal mechanism parameters are shown in Figure 4.10 and Table 4.4, respectively. The focal mechanisms determined in Western Marmara segment show mostly strike-slip and normal faulting style. There are also several events that exhibits thrust faulting around Central Basin. As normal faulting in the Sea of Marmara is a very well known feature (e.g. Parke et al., 2002), fault plane solutions numbered 66, 67, 71, 72, 74, 81 located in the southern part of Central Basin indicates NE-SW extensional normal faulting mechanism.

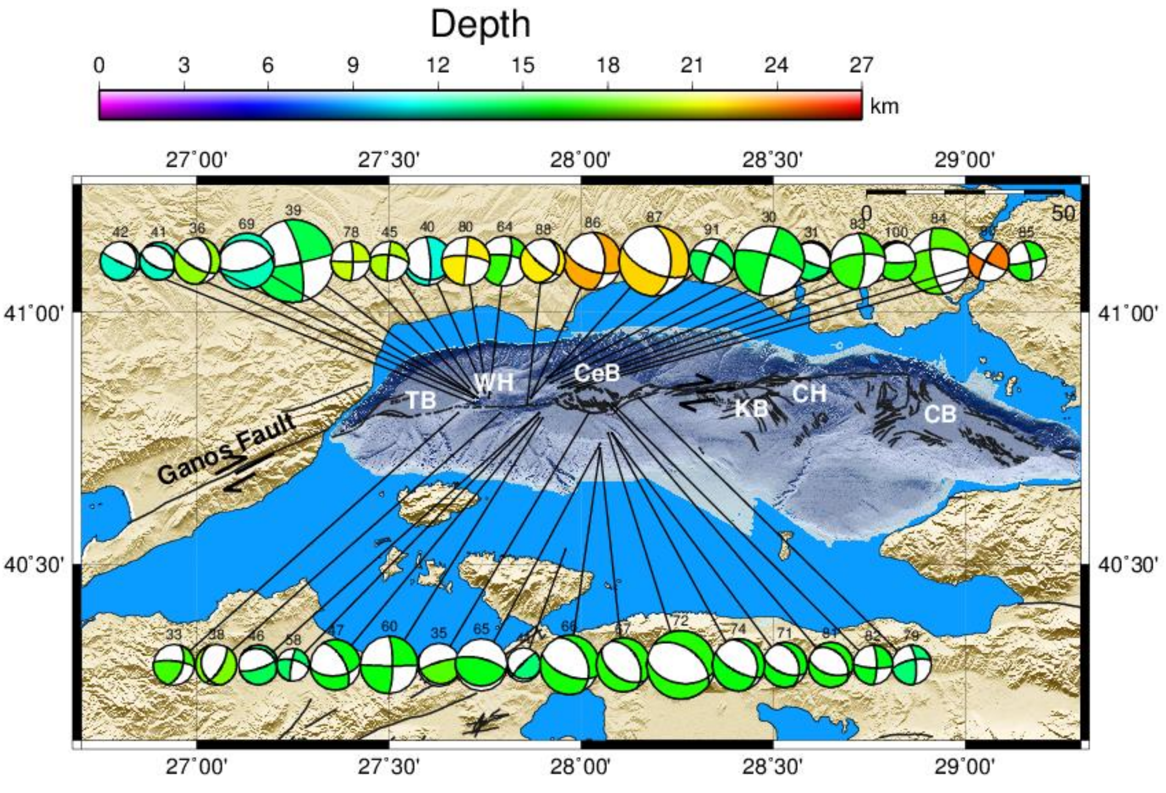

Figure 4.10. Focal mechanism derived from simultaneous inversion of the polarity data acquired in Western Marmara Segment. KB: Kumburgaz Basin, CH: Central High, CB: Cinarcik Basin.

The focal mechanism of event numbered 45, 80, 64, 83, 84 show that NAF crosses the WH and eastern CeB in almost E-W direction with a fault segment dipping gently northward.

Table 4.4. Focal mecahnism parameters derived from simultaneous inversion of the polarity data acquired in Western Marmara Segment.

Event number	**Date**	**Time**	**Lat.**	**Lon.**	**M_W**	**H**	**Strike**	**Dip**	**Rake**	**Number of Stations**
30	29.08.2015	12:47	40.87	27.92	3.9	15.4	287.2	75.5	-174.9	12 OBS Stations
31	29.08.2015	18:14	40.86	27.92	2.2	14.2	315.1	10.0	-67.3	11 OBS Stations
33	13.09.2015	05:11	40.80	27.68	2.3	17.6	17.0	54.6	18.5	10 OBS Stations
35	19.09.2015	18:49	40.80	28.02	2.4	17.9	120.0	15.0	136.1	10 OBS Stations
36	01.10.2015	10:45	40.84	27.71	2.6	19.3	0.0	40.0	-37.6	10 OBS Stations
38	16.10.2015	02:00	40.80	27.79	2.3	18.8	165.0	30.0	-131.7	11 OBS Stations
39	28.10.2015	16:20	40.83	27.73	4.6	14.6	348.0	75.0	-5.6	13 OBS Stations
40	28.10.2015	16:22	40.84	27.75	2.7	11.6	108.0	25.0	-156.4	10 OBS Stations
41	28.10.2015	18:43	40.83	27.72	2.1	12.1	315.1	30.0	-72.5	10 OBS Stations
42	28.10.2015	21:50	40.82	27.72	2.2	12.1	10.6	17.8	-16.6	11 OBS Stations
44	02.112015	10:33	40.53	27.96	1.9	13.8	112.5	20.0	156.5	10 OBS Stations
45	02.11.2015	18:32	40.84	27.73	2.2	19.9	276.9	65.0	-176.3	10 OBS Stations
46	10.11.2015	11:23	40.80	27.89	2.2	14.5	298.7	21.3	-45.3	11 OBS Stations
47	01.11.2015	11:26	40.79	27.89	2.8	16.0	85.3	53.5	-141.5	12 OBS Stations
58	25.11.2015	09:34	40.80	27.89	1.8	14.1	283.8	65.0	-170.3	10 OBS Stations
60	28.11.2015	06:41	40.79	27.90	3.2	16.2	0.0	80.0	-2.9	12 OBS Stations
64	22.12.2015	15:10	40.83	27.76	2.8	17.3	276.4	70.0	160.6	12 OBS Stations
65	03.01.2016	17:46	40.74	28.05	2.9	15.9	90.0	20.0	76.4	11 OBS Stations
66	06.10.2016	15:44	40.73	28.05	3.3	16.5	337.4	40.0	-52.1	13 OBS Stations
67	06.10.2016	16:04	40.73	28.05	3.0	16.9	330.9	42.8	-71.2	12 OBS Stations
69	12.01.2016	01:48	40.83	27.73	3.1	12.2	283.7	27.7	-65.3	13 OBS Stations
71	28.01.2016	15:06	40.76	28.08	2.5	16.0	337.4	40.0	-52.1	13 OBS Stations
72	30.01.2016	09:03	40.76	28.07	3.8	16.9	100.0	45.0	-108.7	13 OBS Stations
74	01.02.2016	18:38	40.76	28.08	2.9	16.1	345.0	30.0	-47.3	11 OBS Stations
78	24.02.2016	04:26	40.85	27.71	2.2	20.4	0.0	80.0	-2.9	12 OBS Stations
79	29.02.2016	04:52	40.83	28.15	2.2	13.8	257.1	70.0	159.6	11 OBS Stations
80	01.03.2016	14:54	40.86	27.75	2.7	22.0	275.0	72.5	180.0	13 OBS Stations
81	10.03.2016	14:47	40.82	28.07	2.5	16.6	315.4	38.7	-66.5	11 OBS Stations
82	11.03.2016	18:40	40.82	28.08	2.2	15.7	360.0	75.1	-13.2	12 OBS Stations
83	23.03.2016	03:51	40.86	27.95	3.1	17.2	263.6	70.0	159.8	12 OBS Stations
84	24.03.2016	08:04	40.85	27.95	3.7	18.0	270.0	60.0	-160.2	13 OBS Stations

85	25.03.2016	22:18	40.85	27.99	2.2	16.6	348.0	75.0	-5.6	10 OBS Stations
86	27.03.2016	05:03	40.83	27.87	3.2	23.4	360.0	55.0	-33.9	13 OBS Stations
87	27.03.2015	05:03	40.83	27.87	3.9	22.5	360.0	50.0	-35.9	11 OBS Stations
88	27.03.2016	05:05	40.82	27.86	2.5	22.0	15.1	30.0	-27.8	10 OBS Stations
90	01.04.2016	23:22	40.85	27.97	2.3	24.4	208.1	80.0	6.2	12 OBS Stations
91	06.04.2016	04:34	40.87	27.91	2.5	14.5	296.5	68.1	-169.2	12 OBS Stations
100	05.06.2016	20:49	40.85	27.94	2.2	17.0	210.1	15.0	-149.1	11 OBS Stations

4.2.3. Central Marmara Segment

The data acquired in Central Marmara Segment include 24 events with magnitudes between 1.9 and 4.2. For this cluster in total 273 P-wave polarities are used in order to determine focal mechanisms. The focal mechanism results and list of the focal mechanism parameters are shown in Figure 4.11 and Table 4.5, respectively. Although there are ten M > 3.0 earthquakes occur in this cluster, the seismic activity is visibly less than Ganos and Western Marmara segments. Morever, results indicate that there is no seismicity along with Main Marmara Fault between Kumburgaz Basin and western Cinarcik Basin.

The focal mechanisms in eastern Central Basin show predominantly N-S extension while the Çınarcık basin events show NW-SE extension. The hypocenter locations of the events occurred in Central Marmara Segment changes between about 5 km to 12 km depth. The results show that the Central Marmara Segment is the shallower and seismically less active segment of the NAF in Marmara Sea.

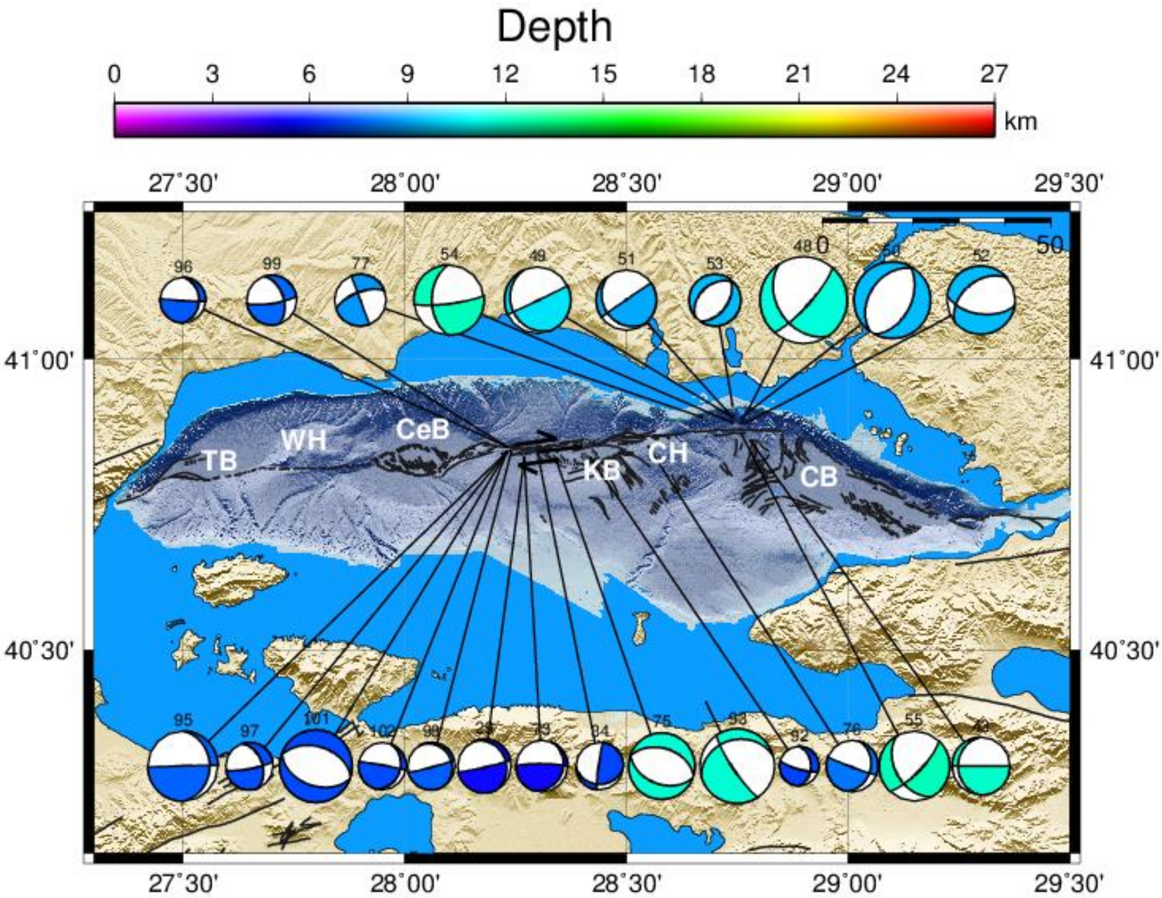

Figure 4.11. Focal mechanism derived from simultaneous inversion of the polarity data acquired in Central Marmara Segment.

Table 4.5. Focal mecahnism parameters derived from simultaneous inversion of the polarity data acquired in Central Marmara Segment.

No.	Date	Time	Latitude	Longitude	M_W	H	Strike	Dip	Rake	Number of Stations
29	24.08.2015	04:47	40.83	28.27	2.6	5.3	337	20	-10	10 OBS Stations
34	17.09.2015	21:39	40.84	28.30	2.3	6.9	90	25	-171	10 OBS Stations
43	31.10.2015	21:10	40.86	28.78	2.8	11.9	180	22	180	10 OBS Stations
48	16.11.2015	15:45	40.89	28.76	4.2	11.6	146	40	-161	14 OBS Stations
49	16.11.2015	16:36	40.90	28.74	3.2	10.3	157	20	-176	12 OBS Stations
50	16.11.2015	17:04	40.90	28.76	3.7	9.4	215	40	-83	14 OBS Stations
51	16.11.2015	18:13	40.90	28.74	2.9	9.0	144	25	-178	11 OBS Stations
52	17.11.2015	02:17	40.89	28.77	3.3	9.4	230	45	-128	12 OBS Stations
53	17.11.2015	03:05	40.92	28.74	2.5	9.4	228	40	-80	10 OBS Stations

54	17.11.2015	04:36	40.89	28.74	3.4	12.2	180	50	-169	11 OBS Stations
55	18.11.2015	12:52	40.87	28.76	3.4	12.3	150	45	-158	13 OBS Stations
73	30.01.2016	16:33	40.83	28.27	2.5	5.2	22	20	22	11 OBS Stations
75	05.02.2016	08:02	40.83	28.34	3.2	11.7	110	45	-87	13 OBS Stations
76	12.02.2016	17:43	40.85	28.55	2.5	7.9	15	30	-6	12 OBS Stations
77	19.02.2016	10:37	40.90	28.67	2.5	8.6	249	65	179	11 OBS Stations
92	25.04.2016	01:51	40.83	28.42	1.9	6.8	360	40	-20	10 OBS Stations
93	27.04.2016	12:07	40.41	28.68	3.6	11.7	254	29	-159	10 OBS Stations
95	31.05.2016	21:14	40.84	28.23	3.4	7.5	359	25	1	13 OBS Stations
96	31.05.2016	21:17	40.85	28.23	2.2	7.3	0	30	-4	11 OBS Stations
97	01.06.2016	12:32	40.84	28.23	2.3	7.1	340	45	-13	11 OBS Stations
98	02.06.2016	03:56	40.84	28.24	2.3	7.4	330	15	-15	10 OBS Stations
99	03.06.2016	03:06	40.85	28.23	2.4	7.6	342	50	-14	12 OBS Stations
101	15.06.2016	05:20	40.84	28.23	3.5	7.0	110	45	-87	12 OBS Stations
102	17.06.2016	06:35	40.84	28.23	2.3	7.0	18	25	8	10 OBS Stations

4.3. A Case Study - Comparison of Focal Mechanism Solution Determined by CMT and Simultaneous Inversion of the Polarity Data Method

Within datasets, the focal mechanism of 07.12.2015 M3.3 Güzelköy Offshore-Tekirdağ earthquake is determined individually by using CMT and Simultaneous Inversion of the Polarity Data methods. This case study is conducted in order to compare the focal mechanism solution and observe if there is a change in focal mechanism solution and source parameters of the same event by using different approaches and stations.

- *CMT Analysis Result of M3.3 Güzelköy Offshore-Tekirdağ earthquake*

The recordings of 14 permanent broadband seismic stations operated by KOERI are used for the analysis. The locations of permanent broadband seismic stations are shown in Figure 5.12.

Since this event is out of observation period gathered for CMT analysis in Chapter 3, the results in Table 4.1 do not contain this event. The pre-processing and data analysis steps for determination of focal mechanism is carried out using the same procedure as explained in Chapter 3. The moment tensor inversion result for the 07.12.2015 earthquake is given in Figure 4.13.

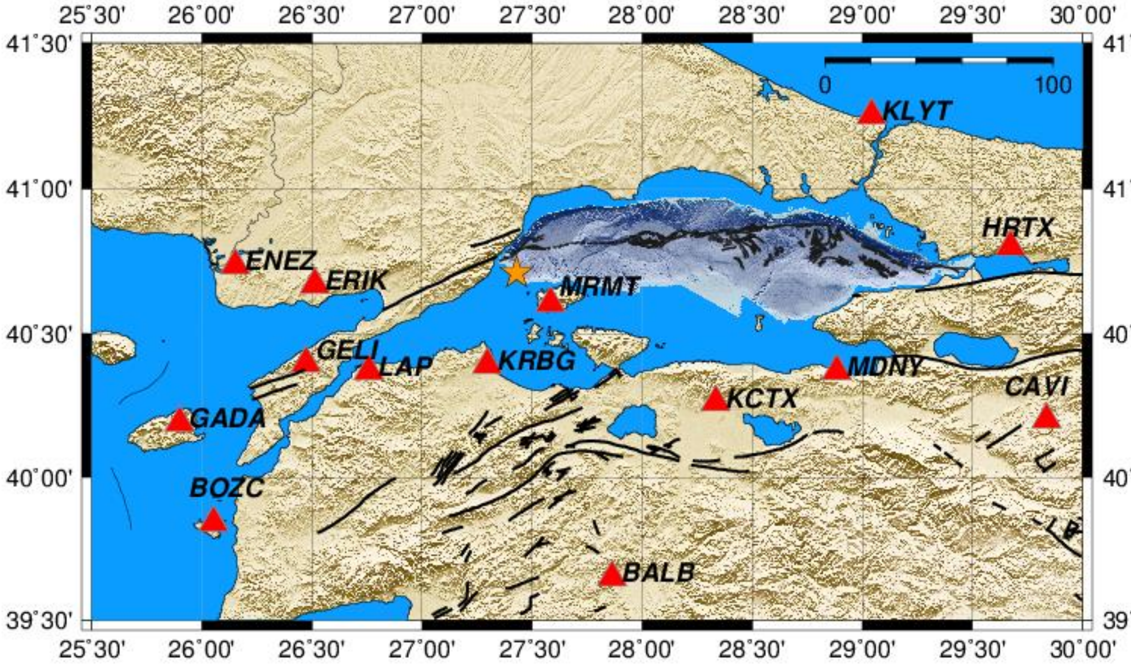

Figure 4.12. Location of land seismic stations used in CMT analysis, together with the location of 07.12.2015 M3.3 Güzelköy Offshore-Tekirdağ earthquake. Red triangles indicate broadband stations operated by KOERI. Orange star indicates the epicenter of 07.12.2015 M3.3 Güzelköy Offshore-Tekirdağ earthquake.

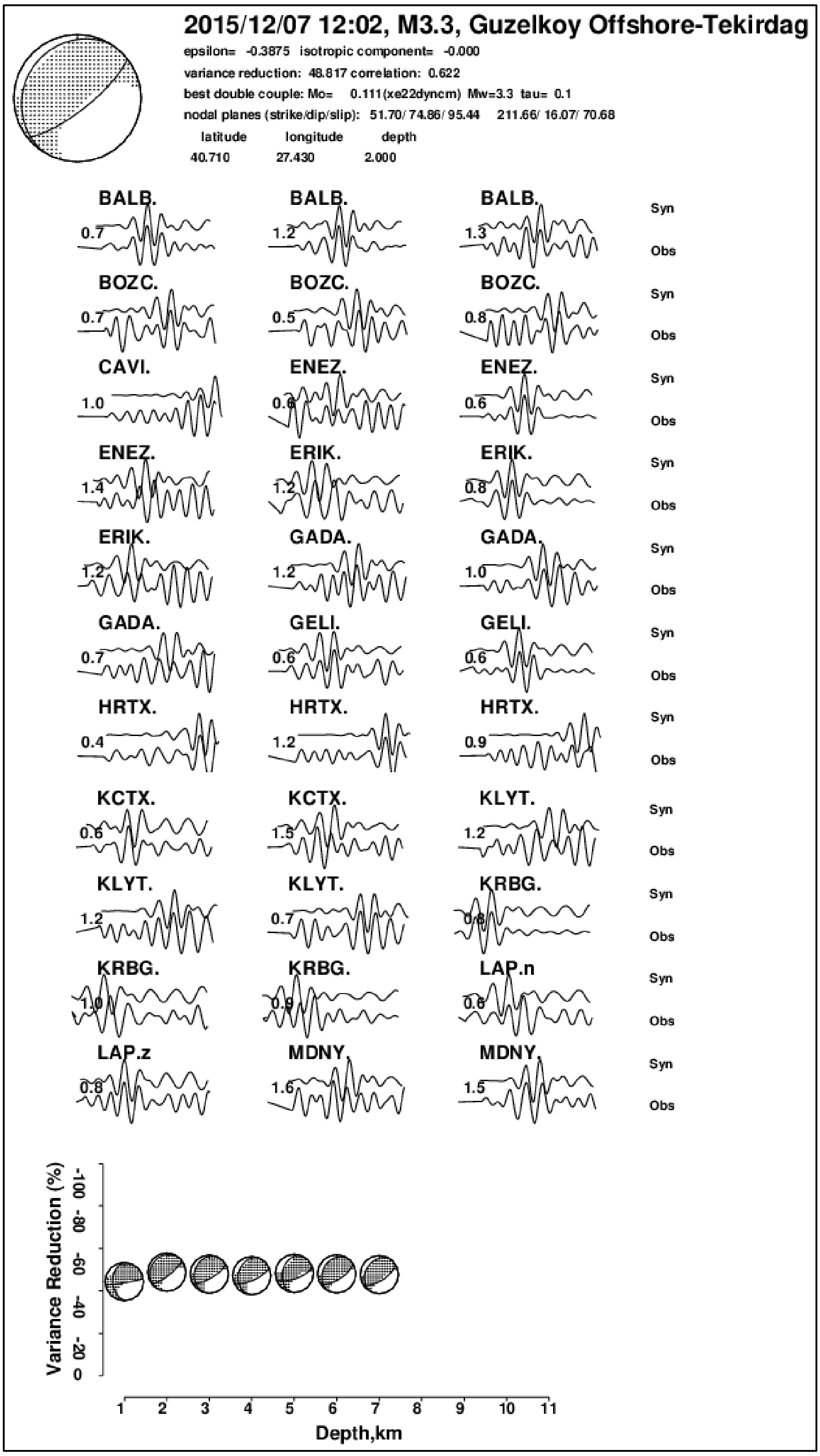

Figure 4.13. The moment tensor inversion result for the 07/12/2015 earthquake (Mw=3.3).

- *Simultaneous Inversion of the Polarity Data Result of M3.3 Güzelköy Offshore-Tekirdağ earthquake*

07.12.2015 M3.3 Güzelköy Offshore-Tekirdağ earthquake is recorded by 12 OBS and 22 Land seismic stations. The focal mechanism of this event is determined in the cluster of Ganos Area in Section 4.2.1. Figure 4.14 shows the location of seismic stations that the first arrival of P-waves is used.

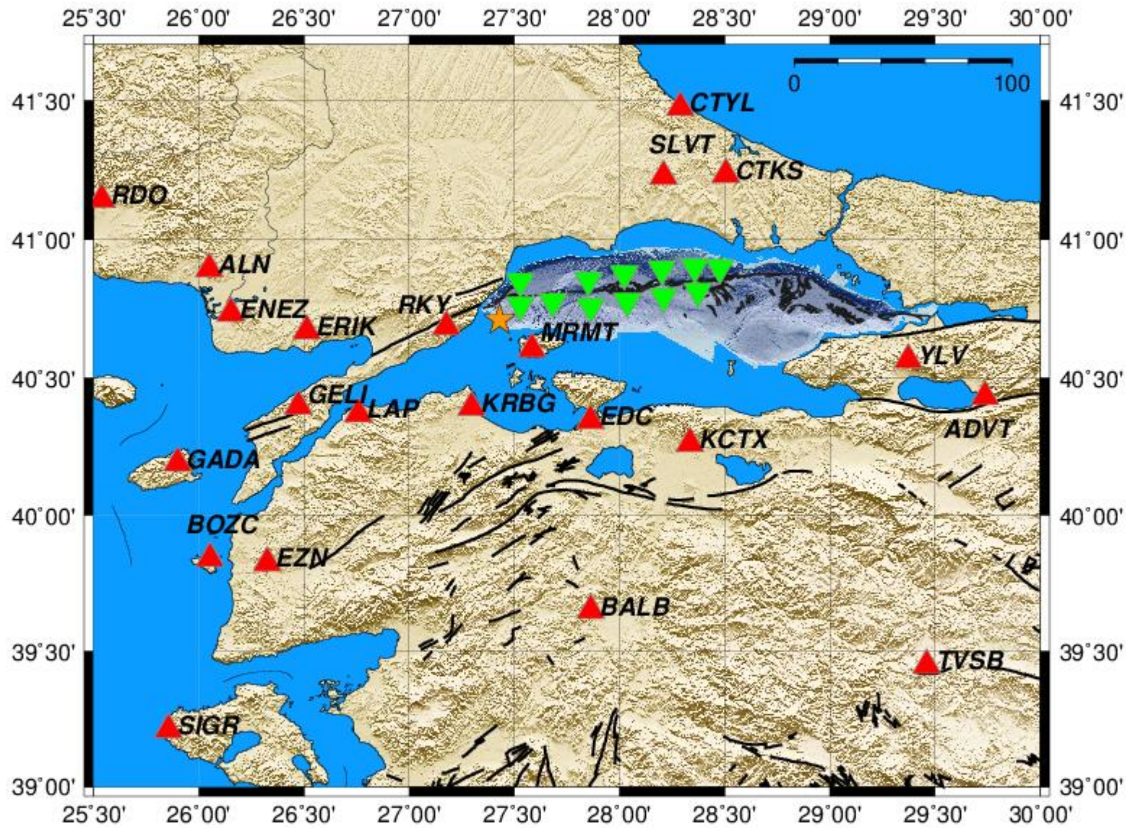

Figure 4.14. Location of OBS stations and land seismic stations used in Simultaneous Inversion of the Polarity Data analysis together with the location of 07.12.2015 M3.3 Güzelköy Offshore-Tekirdağ earthquake. Red triangles indicate broadband stations operated by KOERI. Green triangles indicate OBS stations. Orange star indicates the epicenter of 07.12.2015 M3.3 Güzelköy Offshore-Tekirdağ earthquake.

The result of this case study shows that there is a slight difference in the focal mechanism solution of the same event by using different approaches and datasets (Figure 4.15). By using 14 broadband land seismic stations and following the CMT inversion method developed by Kuge (2003), reverse faulting mechanism is determined for the 07.12.2015 M3.3 Güzelköy Offshore-Tekirdağ earthquake. By using 12 OBS stations together with 22 land seismic stations and following the Simultaneous Inversion of the Polarity Data method using developed by Horiuchi et al. (1995), reverse with minor strike-slip component faulting mechanism is determined for the same event.

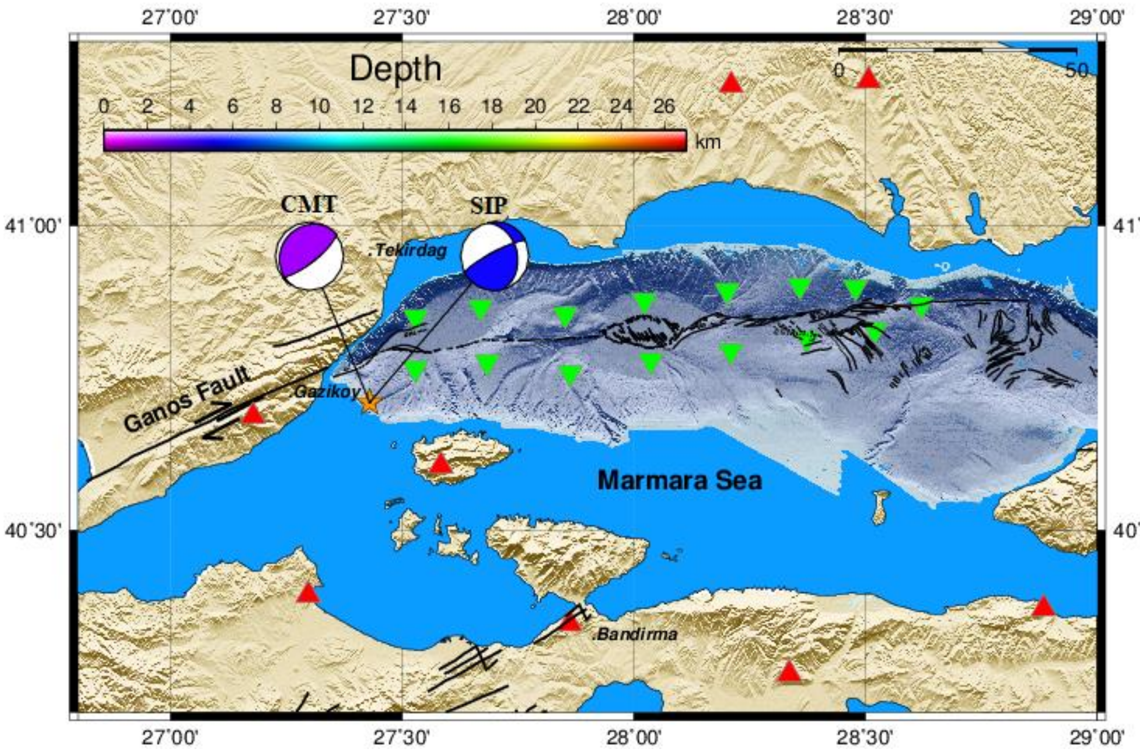

Figure 4.15. Focal mechanism solution of 07.12.2015 M3.3 Güzelköy Offshore-Tekirdağ earthquake using CMT and Simultaneous Inversion of the Polarity Data methods. CMT: Centroid Moment Tensor, SIP: Simultaneous Inversion of the Polarity Data. Red triangles indicate broadband stations operated by KOERI. Green triangles indicate OBS stations. Orange star indicates the epicenter of 07.12.2015 M3.3 Güzelköy Offshore-Tekirdağ earthquake.

Both the focal mechanism of the reverse and reverse with minor strike-slip component faulting types show maximum compressional direction oriented NW-SE. This stress regime is also consistent with the focal mechanism M4.4, 1985 Mürefte earthquake (Figure 4.4).

4.4. September 2019 Offshore Silivri Sequence

During the writing process of the thesis, on 26 September 2019 at 10:59 UTC, M5.7 earthquake occurred in the Sea of Marmara, approximately 20-25 km offshore Silivri. As the results of this study also show that the segment between Silivri offshore and south of Avcılar, namely Kumburgaz segment, is silent in terms of seismicity, the occurrence of magnitude 4.6 and 5.7 earthquakes on the edge of Kumburgaz segment has become critical. The focal mechanism of M4.6 and M5.7 event and 8 largest events occurred within this sequence are determined using CMT method. The results show that the mechanism of the mainshock is reverse with minor strike-slip component (Figure 4.17), and the largest aftershocks are reverse and dominantly strike-slip with a significant reverse component. The results are given Table 4.6 and Figure 4.16.

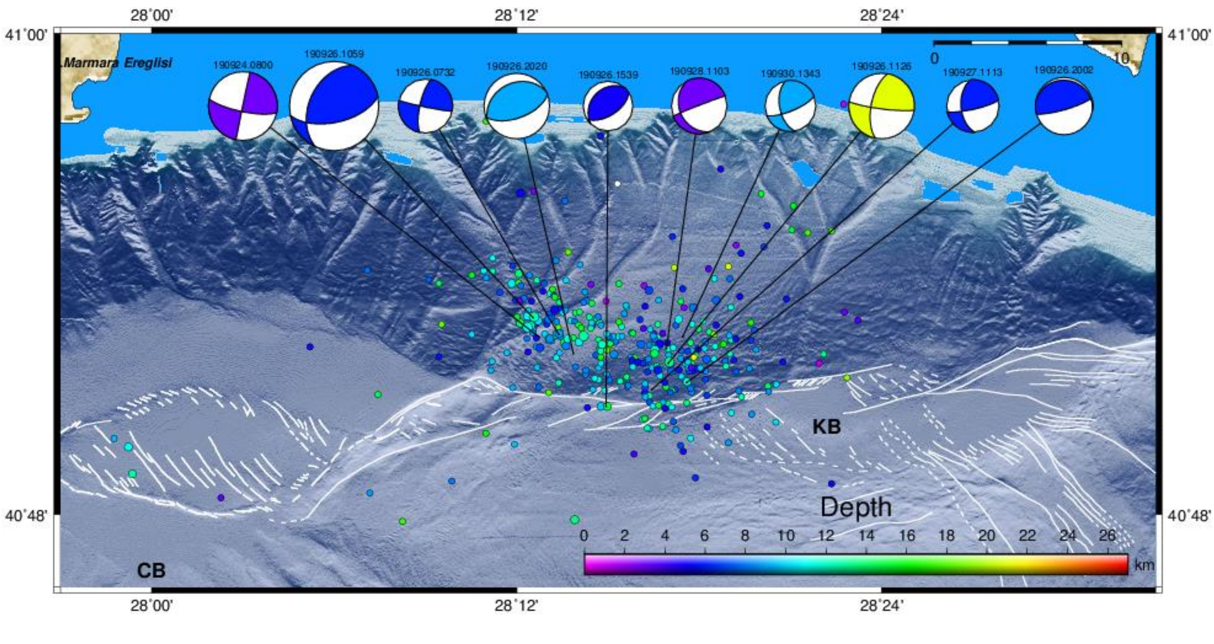

Figure 4.16. CMT inversion results of 24 September 2019 M4.6, 26 September 2019 M5.7 Offshore Silivri earthquakes and largest 8 aftershocks. Circles indicate M>1 events occurred between 13.09.2019-30.09.2019. Symbol sizes are proportional to magnitudes.

Table 4.6. Source parameters of September 2019 Offshore Silivri Sequence obtained using CMT method.

No.	Date	Time	Latitude	Longitude	M_W	H	Strike	Dip	Rake
1	24.09.2019	08:00	40.87	28.21	4.3	3	101	76	179
2	26.09.2019	07:32	40.87	28.22	3.4	6	101	86	163
3	26.09.2019	10:59	40.88	28.20	5.6	6	77	59	123
4	26.09.2019	11:26	40.86	28.28	4.1	21	97	82	153
5	26.09.2019	15:39	40.84	28.24	3.1	5	57	58	97
6	26.09.2019	20:02	40.85	28.29	3.6	6	73	79	85
7	26.09.2019	20:20	40.86	28.23	4.1	9	69	59	93
8	27.09.2019	11:13	40.85	28.27	3.3	6	77	79	142
9	28.09.2019	11:03	40.86	28.28	3.5	3	248	88	-119
10	30.09.2019	13:43	40.87	28.29	3.2	9	67	73	143

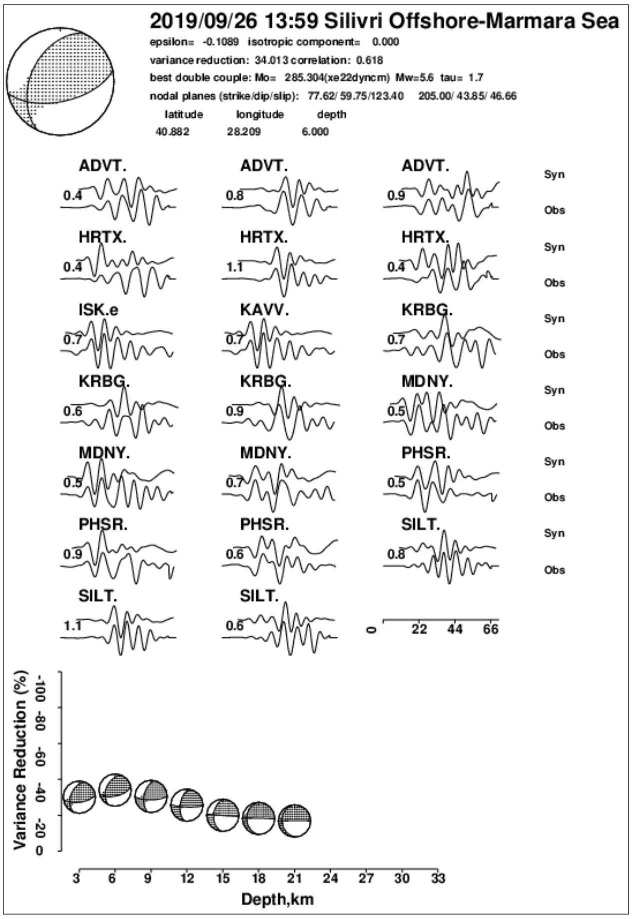

Figure 4.17. The moment tensor inversion result for the 26/09/2019 offshore Silivri earthquake.

5. OUTCOMES OF DATA ACCUMULATION

The first remarkable finding is related with the segmentation and bending between the Ganos Fault and Tekirdag Basin. The transpression is reflected in the morphology as the Ganos Mountain, a major zone of uplift, 10 km wide and 35 km long, elongated parallel to the transpressional Ganos Fault segment west of this bend (Okay et al., 2000). In the west, between the Ganos Fault and Tekirdag Basin, along with the strike-slip faulting mechanism, the focal mechanism solutions of microearthquakes derived by the simultaneous inversion of first motion polarity data by OBS and land seismic stations show significant number of events having reverse faulting mechanism with NW trending compressional stress (Figure 4.9). It is observed that the results are consistent with the fault plane solutions of small to moderate size events determined by CMT analysis and also fault plane solution of the M4.4 27 April 1985 Mürefte earthquake located in the Ganos Mountain, that gives a reverse fault mechanism with a NE striking fault plane (Figure 4.4).

Another remarkable seismotectonic feature is observed in eastern Marmara region inferred from the focal mechanisms taking place in Yalova-Çınarcık and Çınarcık basin locations. Despite the proximity of the two locations, the focal mechanisms in Yalova-Çınarcık region show predominantly N-S extension while the Çınarcık basin events show NE-SW extension. That is to say the stress fields to the north of NAF and the stress field to the south of NAF is rotated by about 45 degree. The results are also consistent with the stress tensor inversion study of Pinar et al (2003), Bulut et al (2009), Pinar et al (2016). Moreover, various types of focal mechanisms are observed in Çinarcik Basin, as strike-slip, normal faulting and reverse faulting mechanism may result from the presence of a segmented fault system where restraining local stresses are developed.

The detection of three earthquakes having pure reverse and reverse with minor strike-slip component faulting mechanisms that occurred 4 km away from the major dextral NAFZ near Bolu city is another remarkable finding of this study. Existence of NAF as one and only active major fault in the region beside local faults, set us thinking that tectonic activity along the NAF and the Pontides are related with each other. The ongoing tectonism and seismicity along the NAF may result in stress accumulation along the surrounding zones forced by the shears on NAF and thus trigger the tectonic evolution of thrusts and strike slip faulting in the northern region of NAF. Both the focal mechanisms of the reverse and strike-slip faulting types show maximum compressional direction oriented NW-SE. This stress regime is consistent also with the focal mechanism of the 1968 Bartin earthquake (Mw=6.5) which is a strong evidence for the relation between the driving forces of the tectonics along NAF and Pontides (Figure 4.7).

The CMT inversion results also give some evidences on the depth of the seismogenic zone of NAF beneath the Sea of Marmara. The centroid depth of the events (85, 87, 91 in Figure 4.3, Table 4.1) taking place offshore Tekirdağ ranges between 18-20 km.

The event numbered 61 took place on the Iznik-Mekece fault showing predominantly strike-slip mechanism with normal faulting component (Figure 4.3). This event not only shows the faulting type of this highly important fault segment in Marmara region extending from Mudurnu valley through Lake Iznik to Gemlik Bay but also the potential of being a capable fault.

The results also show that there are several capable faults in the Biga Peninsula where the predominant faulting type we obtained is strike-slip faulting. In the proximity of this region the devastating Mw=7.2 1953 Yenice-Gönen earthquake took place where the associated surface ruptures indicated mostly strike-slip mechanism. Similar findings we observed on the faults occurring around Kapidag peninsula.

The analysis of microeartquakes recorded by OBS stations deployed closely around the NAF in the Sea of Marmara gives a considerable amount of information about the seismic activity and the seismogenic zone along the different segments of the MMF. The results indicate that Tekirdag Basin, Western High and Central Basin are the most seismically active part in Marmara Sea when compared to eastern segments. The deepest events up to 20-24 km are also observed in Western Marmara Segment, namely Western High and Central Basin. In west, in Ganos Area, the depth of the events observed in the range between 5-19 km. When it comes to Central Marmara Segment, between eastern Central Basin and western Cinarcik Basin, the seismic activity visibility reduces when compared to western segments. Besides, the eastern segments accommodate shallower seismicity. The events generally occur at 7 km deep; the deepest event observed in this region is ≈ 12 km.

In the entire data set, covering microearthquakes and small to moderate size events, the results indicate that there is almost no seismic activity in the Kumburgaz Basin. The results are also consistent with the latest studies of Lange et al (2019) and Schmitbuhl et al (2015) indicating the low seismicity in the Kumburgaz Basin along the MMF. The sparse seismicity beneath the Kumburgaz Basin, besides the high level of seismicity on both edges suggests that this section of the NAF is locked and so accumulating strain (Lange et al, 2019, Schmitbuhl et al, 2015, Yamamoto et al, 2015).

6. DATA INTERPRETATION-METHOD AND RESULTS

In this part of the study, the focal mechanisms of small size NAF earthquakes obtained in data accumulation part are used to obtain the dominat stress acting on the NAF in the Sea of Marmara. Moreover the focal mechanisms are used to obtain representative deformation pattern for each segment, to be used as an input in instrumental period seismic strain rate estimations. The seismic, geodetic and geologic strain rates and moment rates are determined to identify the transpressional and transtentional features and also their seismic potential. The detailed information about the data and methods are explained in the subsections of this chapter.

6.1. Representative Moment Tensors

Kostrov (1974) summation demonstrates how strain rates in a seismogenic volume can be estimated from moment tensors (See section 6.3). In order to estimate seismic strain rates for instrumental period, the moment tensor solutions of events from 1900 to present are needed. Unfortunately, the vast majority of moment tensors are not available for this period. In order to overcome this problem, a representative deformation pattern is estimated from the available fault plane solutions obtained from the first part of this study.

A wide range of focal mechanism solutions of earthquakes in the observation period in the Sea of Marmara and surroundings provide a basis to determine Representative Moment Tensor for the region. With simple arithmetic addition, the moment tensor components of the mechanism are summed up and a moment tensor that represents the sum appears. This calculation is done for each segment using fault plane solutions in Figure 4.5, Table 4.3, Table 4.4, Table 4.5, and the results are shown in Figure 6.1.

Seismic Moment Tensor, M, can be diagonalized and decomposed to the parts since it is symmetric. For a double-couple source, the components of the moment tensor are expressed by ϕ strike, δ dip, λ rake angles of the fault plane and M_0 seismic moment (Equation 6.1) (Aki and Richards, 1980).

$$
\begin{aligned}
Mxx &= -M_0(\sin\delta \cos\lambda \sin 2\phi + \sin 2\delta \sin\lambda \sin 2\phi) \\
Mxy &= M_0(\sin\delta \cos\lambda \cos 2\phi + 0.5 \sin 2\delta \sin\lambda \sin 2\phi) \\
Mxz &= -M_0(\cos\delta \cos\lambda \cos\phi + \cos 2\delta \sin\lambda \sin\phi) \\
Myy &= M_0(\sin\delta \cos\lambda \sin 2\phi - \sin 2\delta \sin\lambda \cos 2\phi) \\
Myz &= -M_0(\cos\delta \cos\lambda \sin\phi - \cos 2\delta \sin\lambda \cos\phi) \\
Mzz &= M_0 \sin 2\delta \sin\lambda
\end{aligned}
\tag{6.1}
$$

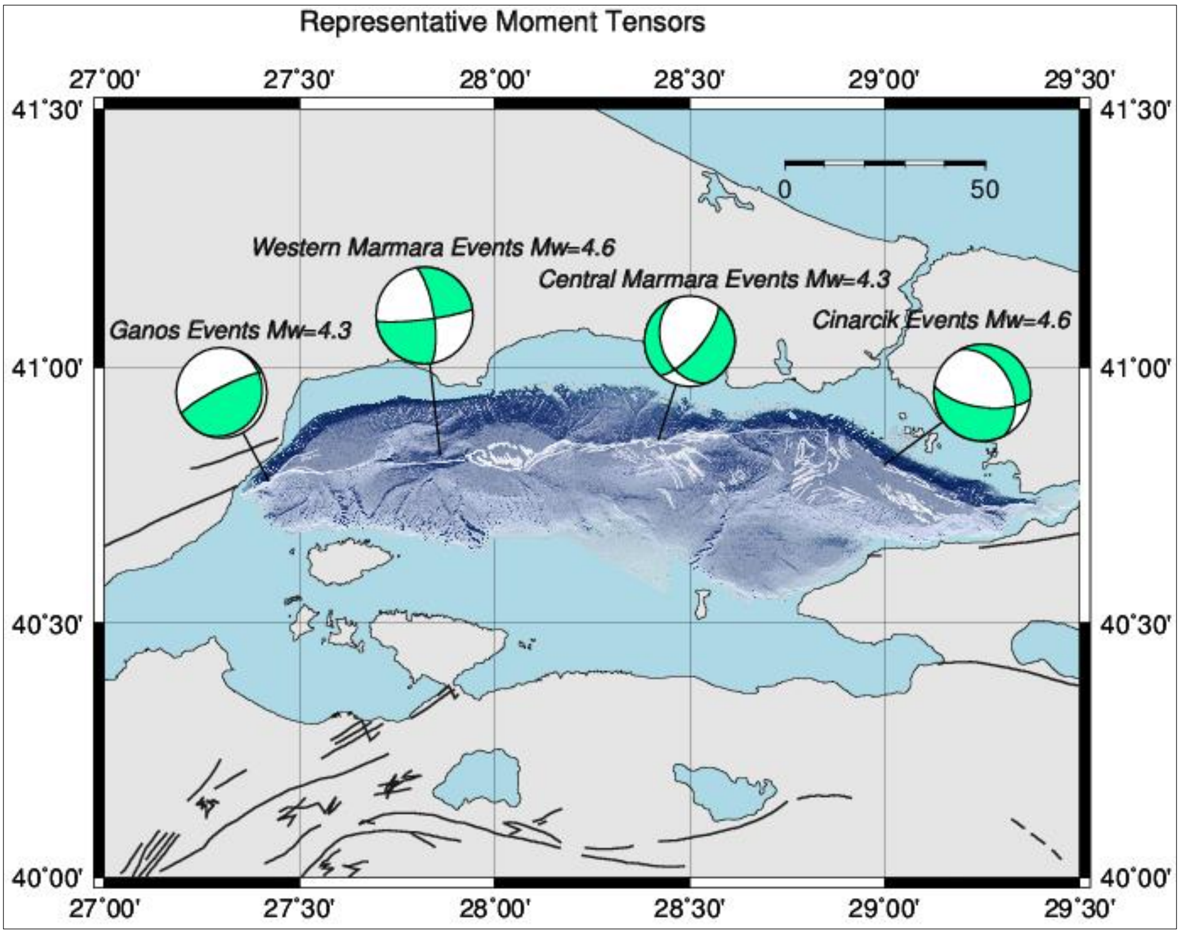

Figure 6.1. Representative Moment Tensor solutions derieved for the study region using fault plane solutions obtained from this study. The mechanisms derived using 37 fault plane solutions of Ganos events, 38 of Western Segment events, 24 of Central Segment events and 24 of Çınarcık Basin events.

6.2. Stress Tensor Inversion

The dominant stress acting on the NAF in the Sea of Marmara is derived following the method developed by Gephart (1990). The dataset is the orientation of the P- and T-axes of 102 earthquake focal mechanisms determined by Simultaneous Inversion of First Motion Polarity analysis (Table 4.2).

In this method, it is assumed that the events have occurred in a region without any spatial or temporal changes in the stress field, and so the slip direction indicates the shear stress direction on any fault plane (Pinar et al., 2016). The stress tensor is the combination of the three principal axes σ1 (maximum compression), σ2 (intermediate compression), σ3 minimum compression, and the ratio of their differences, the stress magnitude ratio, defined as $R = (\sigma 2 - \sigma 1)/(\sigma 3 - \sigma 1)$. R value points out the dominant stress regime in the region of interest. The best-fitting stress model, which is the closest model match the whole observed data set, is determined by a grid search over range of four stress tensor parameters (Gephart, 1990). The misfit is defined as the smallest rotation about an axis of any orientation that brings one of the nodal plane and its slip vector into an orientation consistent with the stress model (Pinar et al., 2016).

The stress tensor inversion results are obtained for group of events in Ganos Area, Western Marmara Segment and Central Marmara Segment are given in Figure 6.2, Figure 6.3 and Figure 6.4. The stress tensor inversion results point out NW-SE oriented σ1 and NE-SW oriented σ3 in almost entire Marmara Sea.

Ganos Area

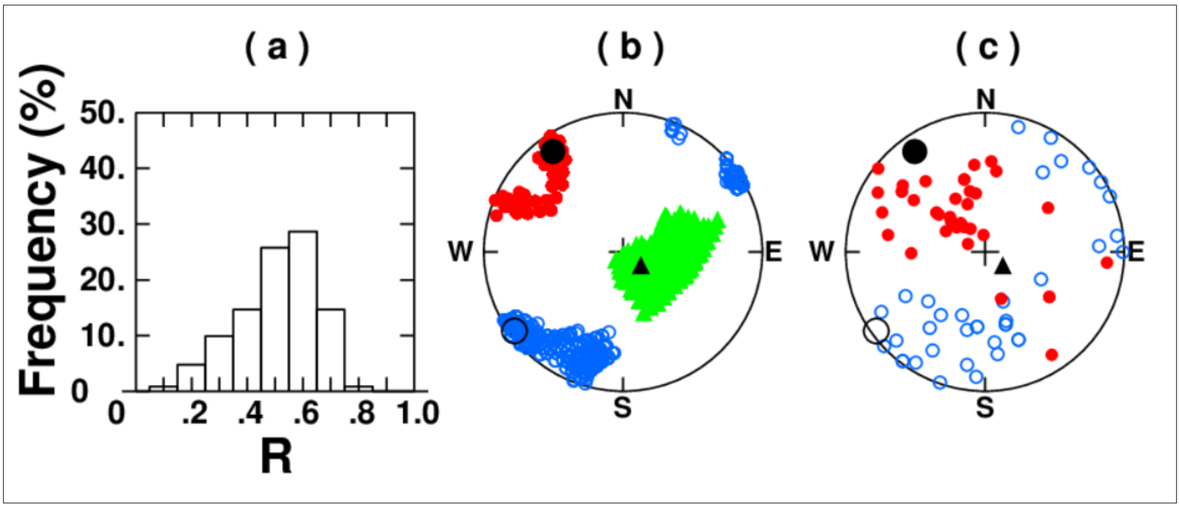

Figure 6.2. Regional stress tensor results for the Ganos area earthquakes. (a) The histogram of R-values, (b) The dissipation of the predicted principal stress axes, red dots indicate azimuth and plunge of σ1, blue circles σ3 and green triangles σ2. (c) The dissipation of the observed P- and T-axes. Red dots indicate the P-axes and blue circles the T-axes.

Western Marmara Segment

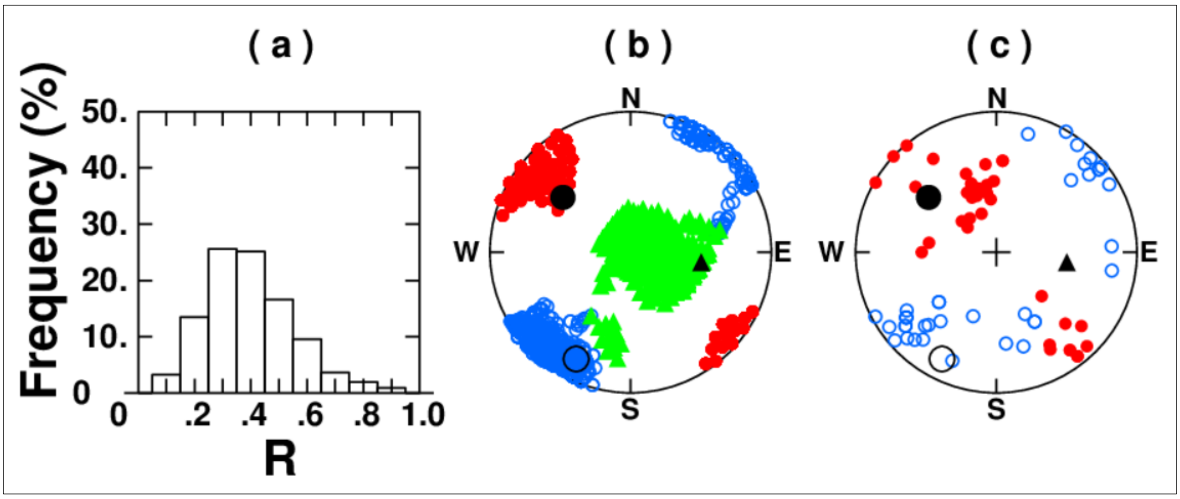

Figure 6.3. Regional stress tensor results for the Western Marmara Segment earthquakes.

<u>*Central Marmara Segment*</u>

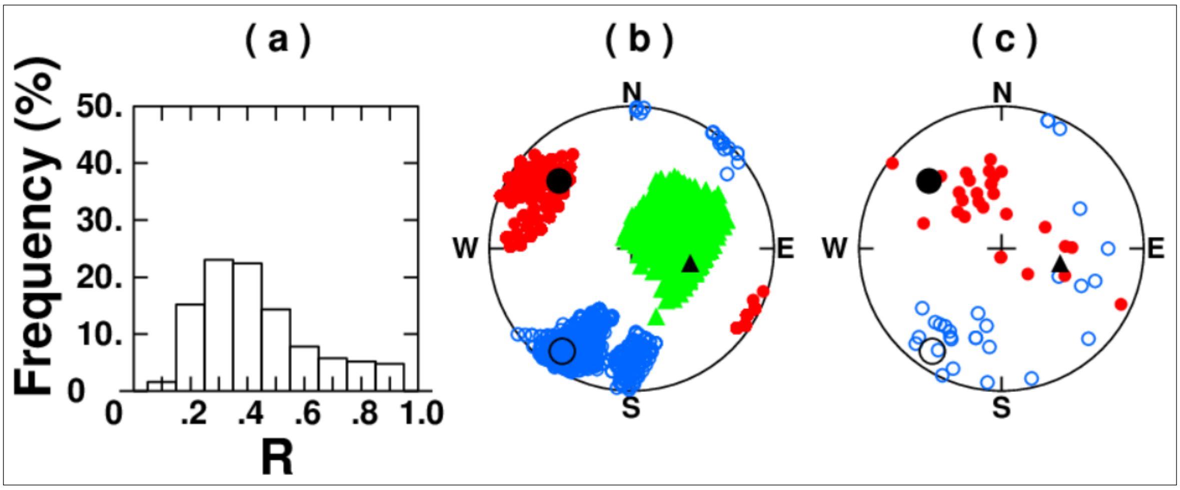

Figure 6.4. Regional stress tensor results for the Central Marmara Segment earthquakes.

6.3. Relation Between Strain Rate and Seismic Moment Rate

Utilizing the earthquakes within a volume taking place at a certain time yields strain rates based on seismicity (Kostrov, 1974; England and Molnar, 1997; Ward 1998). Kostrov introduced the translation formula between strain rate $\dot{\varepsilon}$ and seismic moment rate $\dot{M}_0$ in 1974 which was modified by Ward (1998) as follows,

$$2\mu A H_s \dot{\varepsilon} = \left(\frac{1}{T}\right) \sum_{n=1}^{m} M_n \tag{6.2}$$

The left side of the equation is the average strain rate in a volume and the right side is equivalent to sum of earthquake moment tensors (Ward, 1998). Where μ is rigidity, *A* is the area, *Hs* is the seismogenic thickness. Figure 6.5 is a schematic description of the equation.

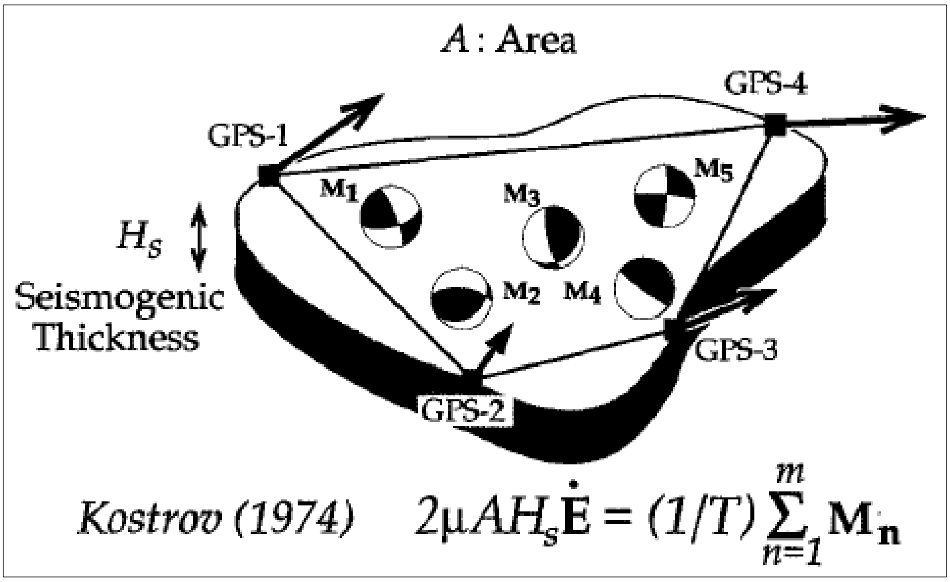

Figure 6.5. Illustration of Kostrov's (1974) linear relationship between the observed geodetic crustal deformation within area A and seismic moment release. (Ward, 1994).

Figure 6.5 states that if the average surface strain rate in a seismogenic area A is known from GPS observations then the Kostrov's equation can be used to estimate the rate of earthquake production. Moreover, the geodetic strain rates can be used to quantify potential earthquake activity that occurs on faults that are undocumented, too slowly slipping or too deep to study by classical seismological or geological techniques (Ward, 1998). Ward outlines the power of space geodesy in estimating earthquakes rates as follows;

- Rates of earthquakes on faults which are unobservable or undocumented can be provided;
- Independent verification of deformation rates in regions can be provided where the faults have been documented by geologists; and
- Means can be provided to judge the consistency of the historical earthquake record and present day deformation field.

Kostrov's equation rewritten in a form to relate geodetic strain rate to seismic moment Mo is expressed as follows

$$2\mu V\dot{\varepsilon} = (\frac{1}{T})M_o \qquad (6.3)$$

Where $\mu = 3 * 10^{11} dyn.cm$ is rigidity, V is the source volume where the strain is accumulated to generate an earthquake that will release the seismic moment M_o. Since the strain rate $\dot{\varepsilon}$, is already a known parameter, having determined the volume V, one can approximate the recurrence time of an earthquake of magnitude M_w using the Hanks and Kanamori (1979) relation between moment magnitude and seismic moment: $M_w = \frac{2}{3}(\log M_o - 10.7)$.

6.3.1. The Earthquake Source Volume Estimation

The crucial point in caluculations is how to estimate the earthquake source volume V; especially, how to determine the horizontal width around a seismic source where the strain is evolving. Very few studies exist tackling the problem of correlating the earthquake volume with earthquake size or seismic energy released (e.g. Bath and Duda 1964, Lida 1965). The earthquake source volume is approximated as $V = A * H_w$, where A is a rupture area determined from the relation between rupture area RA, and magnitude given as ($LogRA = -3.43 \pm 0.18 + (0.90 \pm 0.03)\mathrm{M}_w$) in Wells and Coppersmith (1994). The H_w parameter was fixed after elaborating the recurrence data retrieved from an extensive paleo seismology study along San Andreas fault on the Wrightwood segment (Weldon et al. 2004) and the strain rate data around that segment (Shen et al. 2015). The recurrence time interval is determined as 31-165 years from 45 trenches, where the mean observed slip is 3.2 m (0.7 m – 7 m per event) and the strain rate in that site is about 200 nanostrain/year. After several trials it was found out that $H_w = 50\ km$ yields satisfactory results in earthquake volume estimations. All these estimations are for strike-slip faulting type.

For normal faulting events the relation between RA and magnitude is given by $LogRA = -2.87 \pm 0.50 + (0.82 \pm 0.08)M_w$. The H_w parameter was set to 50 km for normal faulting following the literature elaborating normal events in Italy where GPS derived strain rates also exist (Pantosti et al. 1993, Galadini and Galli 1999, Palumbo et al. 2004, Devoti et al. 2014, D'Agostino 2014).

For reverse faulting events the $LogRA = -3.99 \pm 0.36 + (0.98 \pm 0.06)M_w$ relation is used for rupture area estimation (Wells and Coppersmith 1994). Because most of the thrust faults in Zagros are hidden no paleo seismology data exist denoting the recurrence rate of large earthquakes (Berberian 1995). Making analogy with the normal faulting case and considering the dip slip sense of motion on the thrust faults, $H_w = 50\,km$ has been adopted for the faults in the compressional regions.

6.3.1.1. Width Estimation of the Source Area of NAF in the Sea of Marmara. In the literature, it is stated that the width of the North Anatolian Fault Zone increases from few kilometers in the east to 100 km in the west (Şengör et al., 2005). But however there is a lack of information on the fault width where the strain is evolving. With similar approach carried for San Andreas Fault, the source width of segments in the Sea of Marmara is estimated using the relationship between slip rates and strain rates by Ward (1994). The geologic slip rates are gathered from various paleoseismic investigations and the strain rates are calculated in this study from geodetic data. The detailed information about the issues is given in related sections below. Using Ward (1994) relation, the width of the source area for each segment in the Sea of Marmara are calculated as given in Table 6.1 and an average single representative value is assisgned as 47 km for the width of the source are for each segment in the Sea of Marmara.

Table 6.1. Estimated source width of NAF in the Sea of Marmara

Region	$\dot{s}_{geol}$, mm/yr	$\dot{\varepsilon}_{geod}$, 10^{-8}/y	**W, km**
Ganos	17.0	17.5	**49**
Western Marmara	17.4	16.0	**54**
Central Marmara	9.5	11.0	**43**
Çınarcık	18.5	23.0	**40**

6.3.1.2. Seismogenic Thickness Estimation of NAF in the Sea of Marmara. In Kostrov (1974), the relationship between strain rate and moment rate depend on the seismogenic thickness parameter. Since the results are highly affected by seismogenic thickness and thus the selection of that parameter plays important role in computations, instead of a single study, various studies (i.e. Bohnhoff et al., 2013, Schmittbuhl et al., 2015, Lange et.

al, 2019, Yamamoto et al., 2017, 2020) on seismogenic thickness of the segments in the Marmara Sea are considered, and a single representative value is obtained by Logic Tree approach for each segment. The values are given in related section below.

6.4. Seismic-Instrumental Period- Strain Rate and Moment Rate

Seismic strain rate and slip rate are one of the most important parameters which reveal the stress accumulation, seismic activity and seismic potential of a fault. Seismic and geodetic strain rate comparison can reveal areas of potential seismic hazard (Middleton et al., 2018).

In this study, the seismic strain rates of Ganos area, Western Marmara, Central Marmara and Çınarcık Basin are estimated following Kostrov summation (1974):

$$\acute{\varepsilon}_{ij} = \frac{1}{2\mu VT} \Sigma M_0 m_{ij} \tag{6.4}$$

In Equation 6.4, μ is the rigidity (3 x 10^{11} dyne/cm^2), V is the volume (fault length (L) x fault width (W) x seismogenic thickness (H_s)), T is the catalogue duration, M_0 is the seismic moment, m_{ij} is the unit moment tensor (Figure 6.5). The right hand side of the equation is determined from seismic observations.

Table 6.2, Table 6.3, Table 6.4, and Table 6.5 show the input parameters that are used in Kostrov (1974) summation for Ganos area, Western Marmara, Central Marmara and Çınarcık Basin, respectively. Figure 6.6 shows the locations of earthquakes occurred in the instrumental period and also the source area that the instrumental period strain rates calculated. Table 6.6 shows the calculated seismic strain and slip rates for each segment.

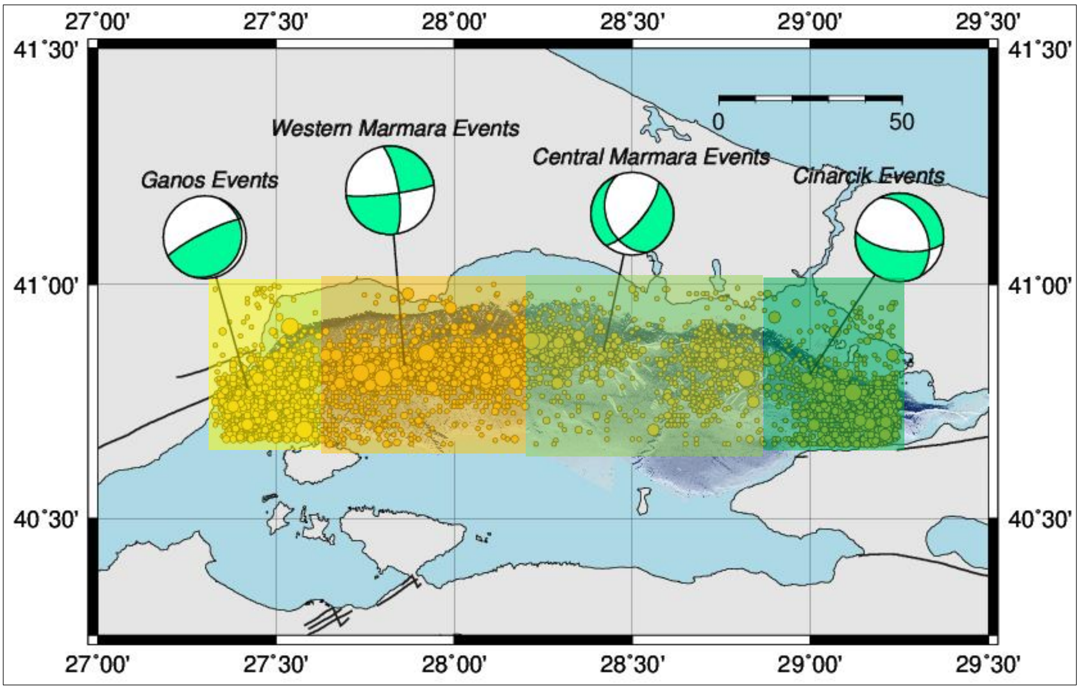

Figure 6.6. The locations of instrumental period events from 1900 to 2020 together with the source area for each segment.

Ganos Area

KOERI Earthquake Catalogue for earthquakes M ≥ 0.5 since 1959 in the source are is used in the analysis for strain rate determination. Figure 6.7 a shows cumulative seismic moment release versus time, Figure 6.7 b shows the total number of earthquakes versus years in the area.

(a)

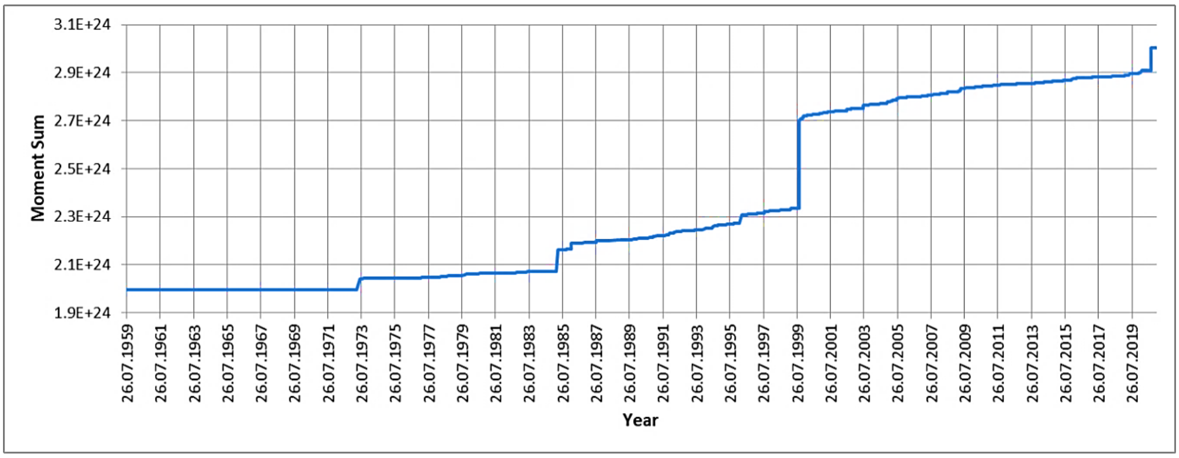

(b)

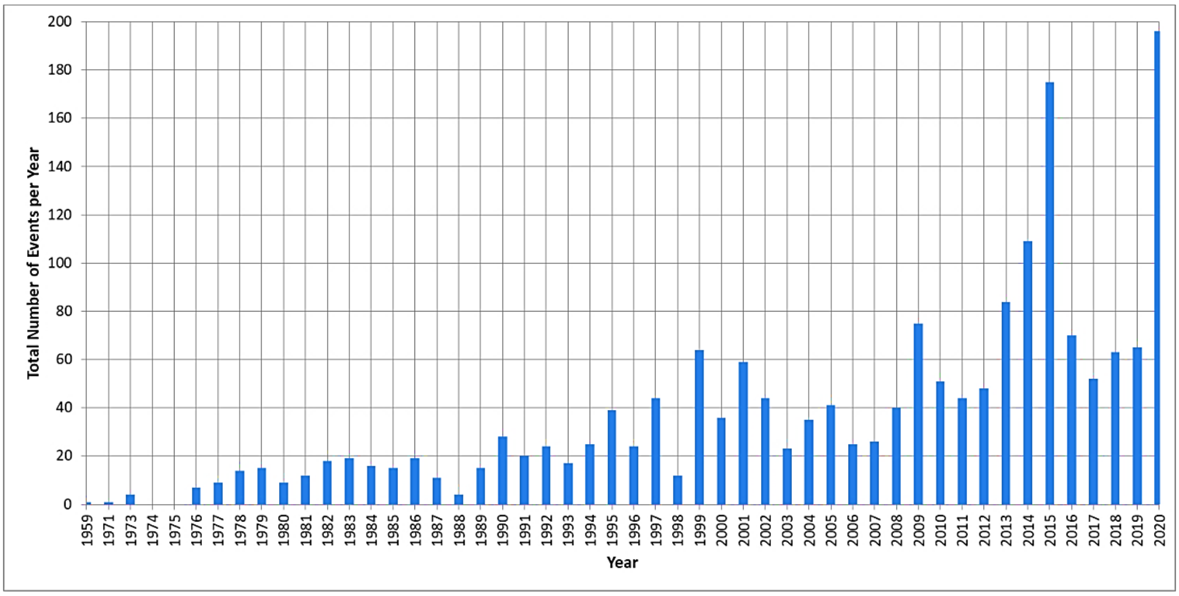

Figure 6.7. The histogram showing the distribution of events in KOERI catalogue occurred in Ganos Area (Latitude: 40.67-41.00, Longitude: 27.33-27.63) between 1959-2020. (a) Cumulative seismic moment release in the 22 km long Ganos region as a function of time. Total seismic moment released is 3.0 x 10^{24} dyne-cm. (b) Total number of earthquakes per year in Ganos region.

Table 6.2. Input parameters for Kostrov (1974) summation - Ganos Area.

Total number of earthquakes	1847
Strik/dip/rake (derieved in section 6.1)	243/81/98
Catalogue duration	61 years
Width of the area	47 km
Length of the area	22 km
Seismogenic thickness	12 km
Source area (A = length x width)	1034 km^2

<u>*Western Marmara*</u>

KOERI Earthquake Catalogue for earthquakes M ≥ 0.5 since 1942 in the source are is used in the analysis for strain rate determination. Figure 6.8 a shows cumulative seismic moment release versus time, Figure 6.8 b shows the total number of earthquakes versus years in the area.

(a)

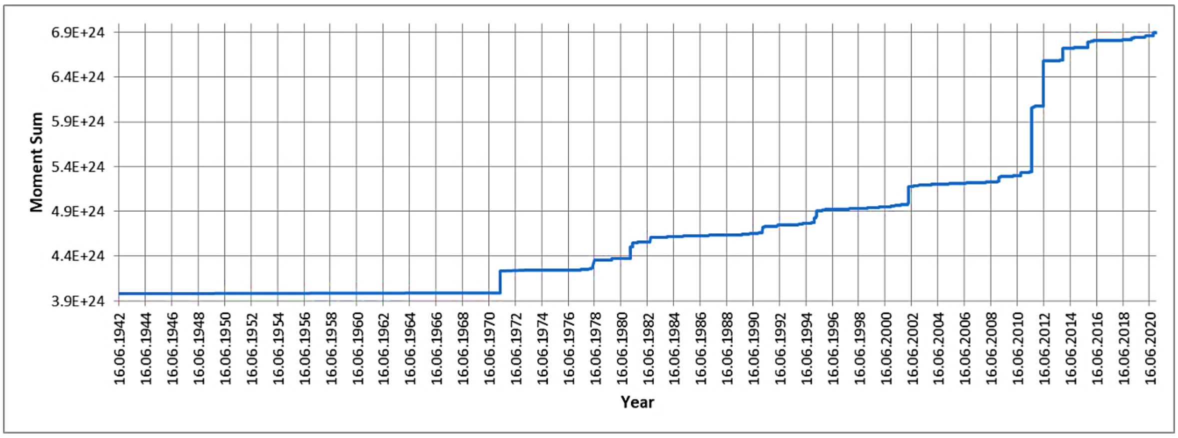

(b)

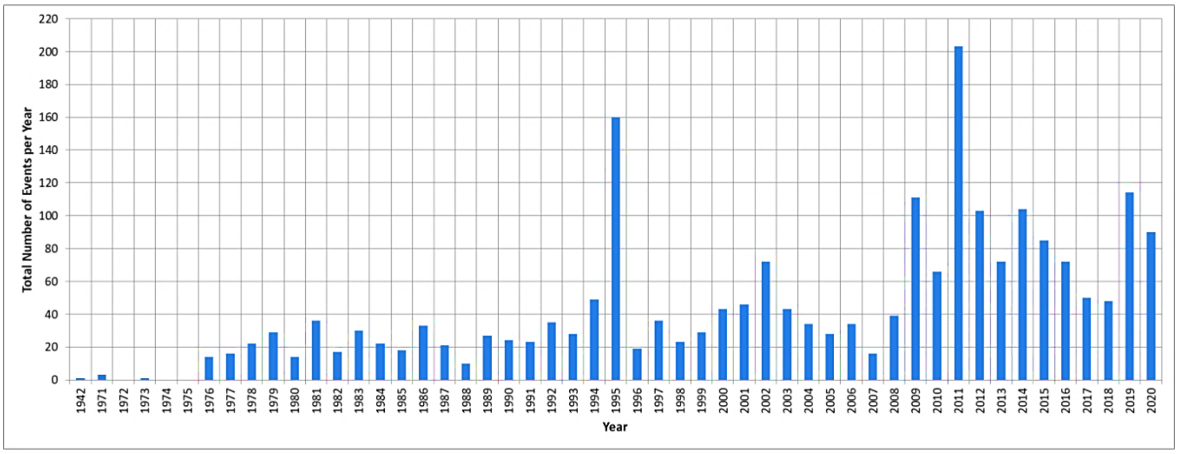

Figure 6.8. The histogram showing the distribution of events in KOERI catalogue occurred in Western Marmara (Latitude: 40.66-41.00, Longitude: 27.63-28.20) between 1942-2020. (a) Cumulative seismic moment release in the 49 km long Western Marmara segment as a function of time. Total seismic moment released is 6.89 x 10^{24} dyne-cm. (b) Total number of earthquakes per year in Western Marmara segment.

Table 6.3. Input parameters for Kostrov (1974) summation - Western Marmara.

Total number of earthquakes	2213
Strik/dip/rake (derieved in section 6.1)	83/83/-164
Catalogue duration	78 years
Width of the area	47 km
Length of the area	49 km
Seismogenic thickness	13 km
Source area (A = length x width)	2303 km^2

Central Marmara

KOERI Earthquake Catalogue for earthquakes M ≥ 0.5 since 1962 in the source are is used in the analysis for strain rate determination. Figure 6.9 a shows cumulative seismic moment release versus time, Figure 6.9 b shows the total number of earthquakes versus years in the area.

(a)

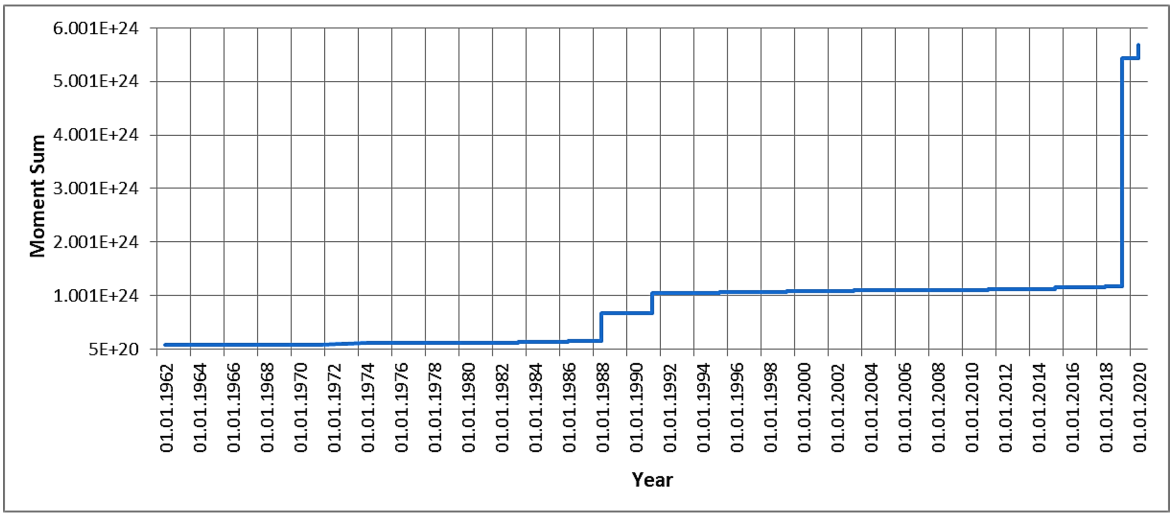

see next page

(b)

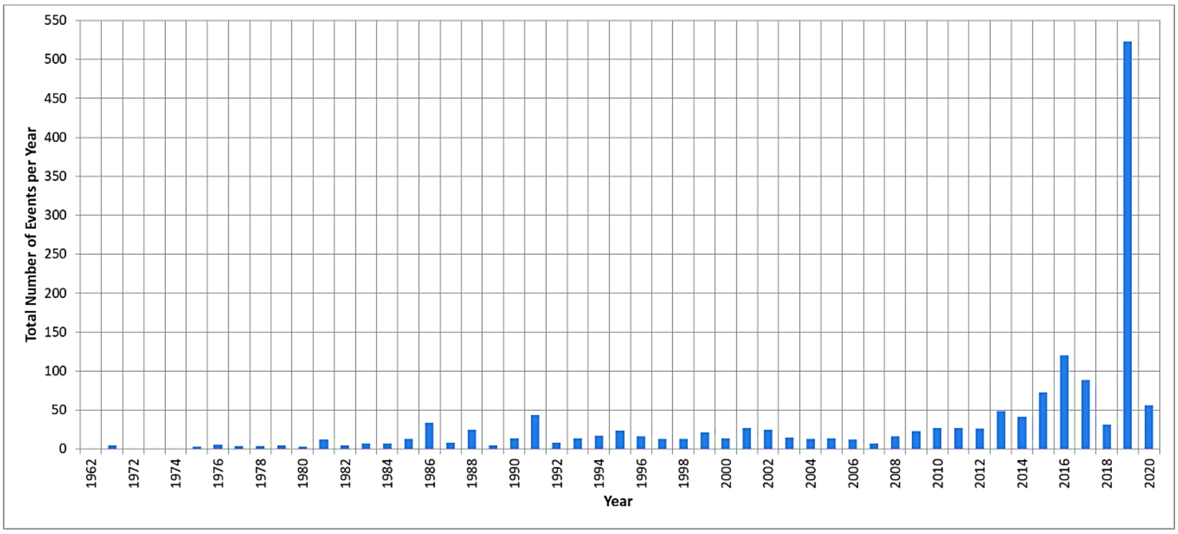

Figure 6.9. The histogram showing the distribution of events in KOERI catalogue occurred in Central Marmara (Latitude: 40.66-41.00, Longitude: 28.20-28.85) between 1962-2020. (a) Cumulative seismic moment release in the 54 km long Central Marmara segment as a function of time. Total seismic moment released is 5.69 x 10^{24} dyne-cm. (b) Total number of earthquakes per year in Central Marmara segment.

Table 6.4. Input parameters for Kostrov (1974) summation - Central Marmara.

Total number of earthquakes	1560
Strik/dip/rake (derieved in section 6.1)	40/70/-58
Catalogue duration	58 years
Width of the area	47 km
Length of the area	54 km
Seismogenic thickness	8 km
Source area (A = length x width)	2538 km^2

Çınarcık Basin

KOERI Earthquake Catalogue for earthquakes M ≥ 0.5 since 1963 in the source are is used in the analysis for strain rate determination. Figure 6.10 a shows cumulative seismic moment release versus time, Figure 6.10 b shows the total number of earthquakes versus years in the area.

(a)

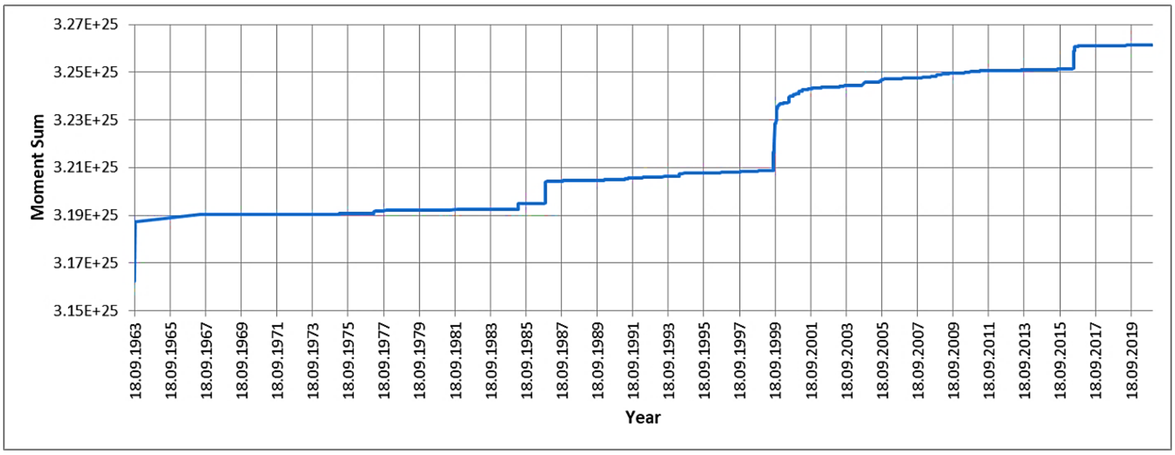

(b)

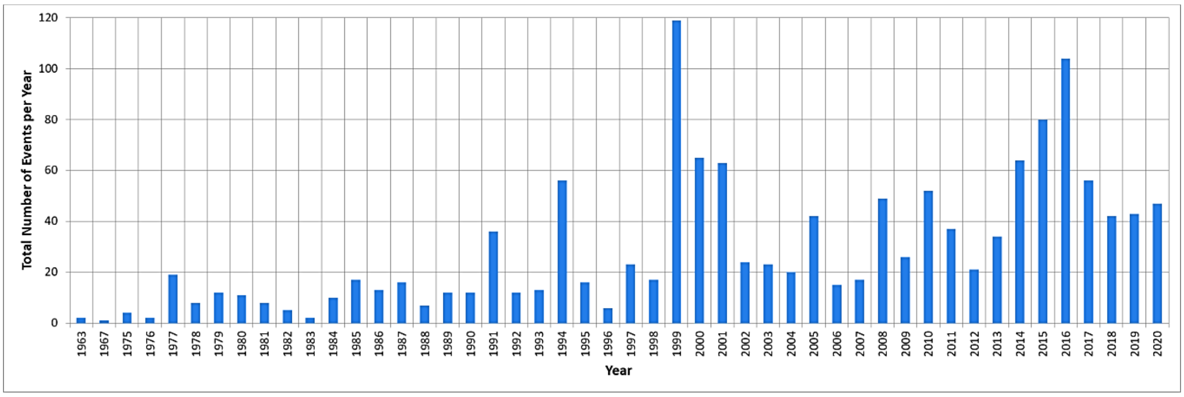

Figure 6.10. The histogram showing the distribution of events in KOERI catalogue occurred in Çınarcık Basin (Latitude: 40.66-41.00, Longitude: 28.85-29.25) between 1963-2020. (a) Cumulative seismic moment release in the 37 km long Çınarcık region as a function of time. Total seismic moment released is 3.26 x 10^{25} dyne-cm. (b) Total number of earthquakes per year in Çınarcık region.

Table 6.5. Input parameters for Kostrov (1974) summation - Çınarcık Basin.

Total number of earthquakes	1383
Strik/dip/rake (derieved in section 6.1)	98/65/-121
Catalogue duration	57 years
Width of the area	47 km
Length of the area	37 km
Seismogenic thickness	13 km
Source area (A = length x width)	1739 km^2

Table 6.6. Seismic Strain Rates, Slip Rates and Moment Rates in the region.

Region	Strain Rate 10^{-8}/y	Slip Rate mm/yr	Moment Rate dyne-cm/yr	T years
Ganos Area	0.56	0.12	4.9 x 10^{22}	61
Western Segment	0.45	0.21	8.8 x 10^{22}	78
Central Segment	0.65	0.31	9.8 x 10^{22}	58
Çınarcık Area	2.77	1.02	5.7 x 10^{23}	57

6.5. Geodetic Strain Rate and Moment Rate

Several studies point out how the horizontal GPS velocities are used to determine the strain rate tensors (e.g., Hackl et al., 2009; Kreemer et al., 2014a; Kreemer et al., 2014b; Ashurkov et al., 2016). The gradients of the velocities are calculated along the northern and eastern directions that give continuous strain fields with values corresponding to strain rate tensor components estimated as;

$$\acute{\varepsilon}_{ee} = \frac{\delta \upsilon_e}{\delta x_e} \tag{6.5}$$

$$\acute{\varepsilon}_{nn} = \frac{\delta \upsilon_n}{\delta x_n} \tag{6.6}$$

$$\acute{\varepsilon}_{en} = \frac{1}{2}\left(\frac{\delta \upsilon_e}{\delta x_e} + \frac{\delta \upsilon_n}{\delta x_n}\right) \tag{6.7}$$

where υ is the GPS velocity at the point x; *e* is the longitude and *n* is the latitude. Having estimated the strain tensor components at each grid point the direction (α_1, α_2) and magnitude ($\acute{\varepsilon}_1$, $\acute{\varepsilon}_2$) of the principal strains is calculated as;

$$\tan 2\alpha_1 = \frac{2\acute{\varepsilon}_{en}}{\acute{\varepsilon}_{nn}-\acute{\varepsilon}_{ee}} \tag{6.8}$$

$$\tan 2\,\alpha_2 = \frac{2\acute{\varepsilon}_{en}}{\acute{\varepsilon}_{nn}-\acute{\varepsilon}_{ee}} \pm 90° \tag{6.9}$$

$$\acute{\varepsilon}_{1,2} = \frac{1}{2}\,(\acute{\varepsilon}_{ee} + \acute{\varepsilon}_{nn}) \pm \sqrt{(\acute{\varepsilon}_{ee} - \acute{\varepsilon}_{nn})} + 4\acute{\varepsilon}_{en}^2 \text{, where } \acute{\varepsilon}_1 > 0,\ \acute{\varepsilon}_1 > \acute{\varepsilon}_2 \tag{6.10}$$

The sum of the diagonal elements of the tensor gives the rate of relative change of area (volume change) and provides the possibility to identify regions of compression or extension (Hackl et al., 2009). The dilatation rate (δ) is estimated as

$$\delta = \acute{\varepsilon}_1 + \acute{\varepsilon}_2 \tag{6.11}$$

The directions of maximum shear strain give possibility to define the directions of the strike-slip faults (dextral and sinistral). The maximum shear strain rate γ_{max} and its directions $\theta_{1,2}$ are found as

$$\gamma_{max} = (\acute{\varepsilon}_1 - \acute{\varepsilon}_2) \tag{6.12}$$

and

$$\tan 2\theta_1 = \frac{\acute{\varepsilon}_{nn}-\acute{\varepsilon}_{ee}}{2\acute{\varepsilon}_{en}} \tag{6.13}$$

$$\tan 2\,\theta_2 = \frac{\acute{\varepsilon}_{nn}-\acute{\varepsilon}_{ee}}{2\acute{\varepsilon}_{en}} \pm 90° \tag{6.14}$$

The style of strain rate tensor, S, is determined as

$$S = (\acute{\varepsilon}_1 + \acute{\varepsilon}_2)\,/max\,(|\acute{\varepsilon}_1|,|\,\acute{\varepsilon}_2|) \tag{6.15}$$

S can be used to approximately quantify the type of displacement into extension ($S > 0.5$), strike-slip ($0.5 < S < -0.5$) and contraction ($S < -0.5$). The second invariant of the strain rate tensor (I_2) is estimated as

$$I_2 = \sqrt{\acute{\varepsilon}_{ee}{}^2 + \acute{\varepsilon}_{nn}{}^2 + 2\acute{\varepsilon}_{en}{}^2} \tag{6.16}$$

6.5.1. GPS Data

The GPS data used to estimate the horizontal crustal strain rates over the Marmara Sea region were compiled from Ergintav et al. (2014). The distribution of the compiled data of 112 GPS stations is shown in Figure 6.11. The station list, including the north and east component of the GPS vectors along with their standard deviations is given as a supplement file Ergintav et al. (2014). The data reduced to Eurasia fixed reference frames is used in the strain rate estimation.

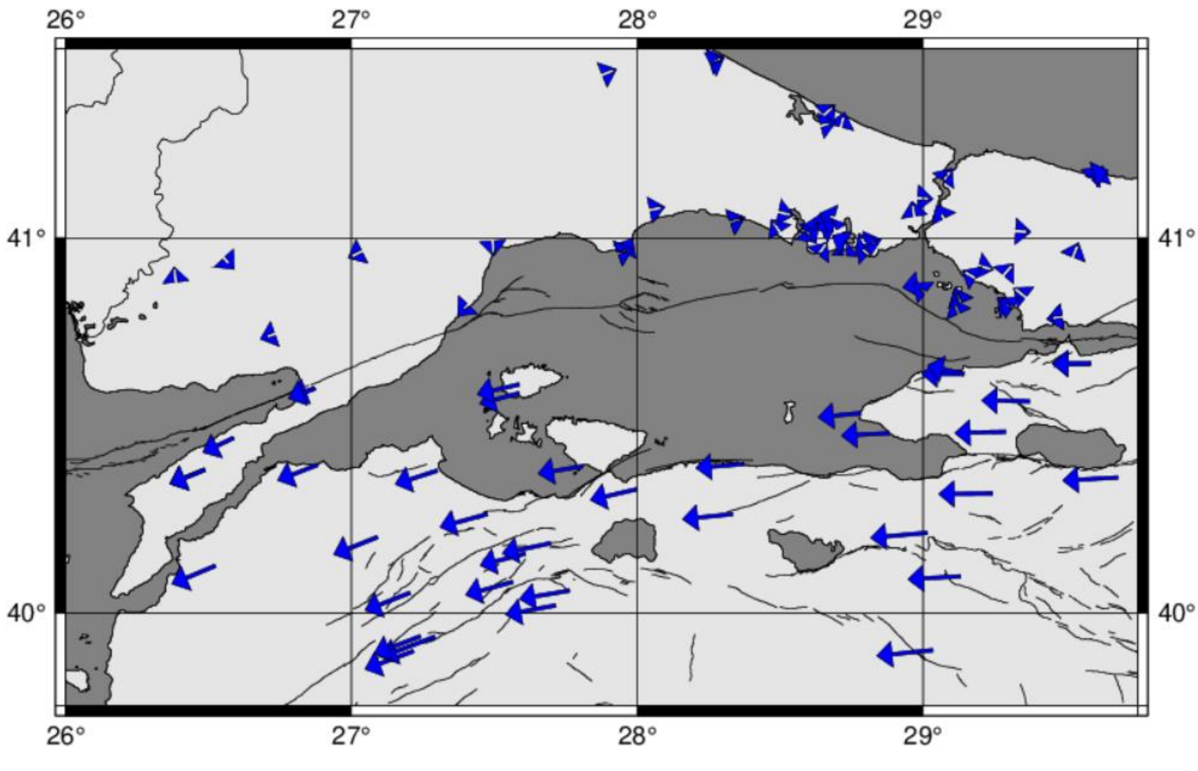

Figure 6.11. The GPS data from the study of Ergintav et al. (2014).

The observation period (from 1994 to 2013) vary from station to station. The computed horizontal velocities with a precision less than 1 mm/yr are found to be between 1-24 mm/year. Note that the stations sitting on the northern block of NAF are located on

Eurasian plate used as a reference frame. As such, the GPS data is compatible with the estimates obtained by others (Meade et al., 2002, Reilinger et al., 2006, Hergert et al., 2011).

6.5.2. GPS Data Optimization

Distance and areal weighting functions are applied to get the smoothly interpolated continuous strain field maps. Gaussian and Quadratic functions are applied for distance weighting. On the other hand, Voronoi cell and azimuthal functions are applied for areal weighting that evaluates the density of the GPS observations. A combination of the two distance and the two areal weighting functions constitutes a weighting scheme (Gi). With a given weighting scheme it is needed to find an optimal net weighting threshold Wt. Having tested various combinations a weighting scheme comprised of Gaussian distance weighting and Voronoi cell areal weighting have been found to be appropriate for the present GPS data set. Afterward, a set of solutions have been obtained employing Gaussian distance weighting function and Voronoi cell areal weighting where net weighting threshold Wt, is set to be Wt=6, 12, 18, and 24. As shown in Shen et al. (2015) it was found out that as Wt increases the strain field is getting smoother.

An optimal interpolation model has been determined through examination of differential strain-rate pattern of two strain-rate fields derived using different Wt in a way described by Shen et al. (2015). Three differential strain rate fields for (Wt=6-Wt=12), (Wt=12-Wt=18) and (Wt=18−Wt=24) using Gaussian and Voronoi cell weighting scheme have been explored (see for details Shen et al. 2015). The differential strain-rate field for (Wt=18−Wt=24) was found to be quite smooth. The (Wt=18−Wt=24) differential strain rate pattern has shown that as Wt decreases from 24 to 18, the strain-rate model picks up more tectonic signals along the active faults. And, vice versa in low deforming zones the amplitudes of the differential principal strain rates significantly diminishe. This result suggests that the Wt>18 net weighting threshold values over-smooth tectonic signals. When Wt decreases from 18 to 12 some incremental strains emerge. However, further decrease in Wt from 12 to 6 reveals that the differential strain rate deteriorates somewhat comparing to that obtained for Wt12-Wt18. Balancing the tradeoff between the resolution and robustness, one may choose model Wt=12 as the optimal model for characterization of the strain-rate field. Model Wt=6 provides more resolution but the increase in noise level is problematic. As for Wt=10 model, it decreases the noise level satisfactorily compared to Wt=6 and increases the resolution compared to Wt=12 model. Therefore, Wt=10 has been selected as an optimal smoothing model for this study (Figure 6.12).

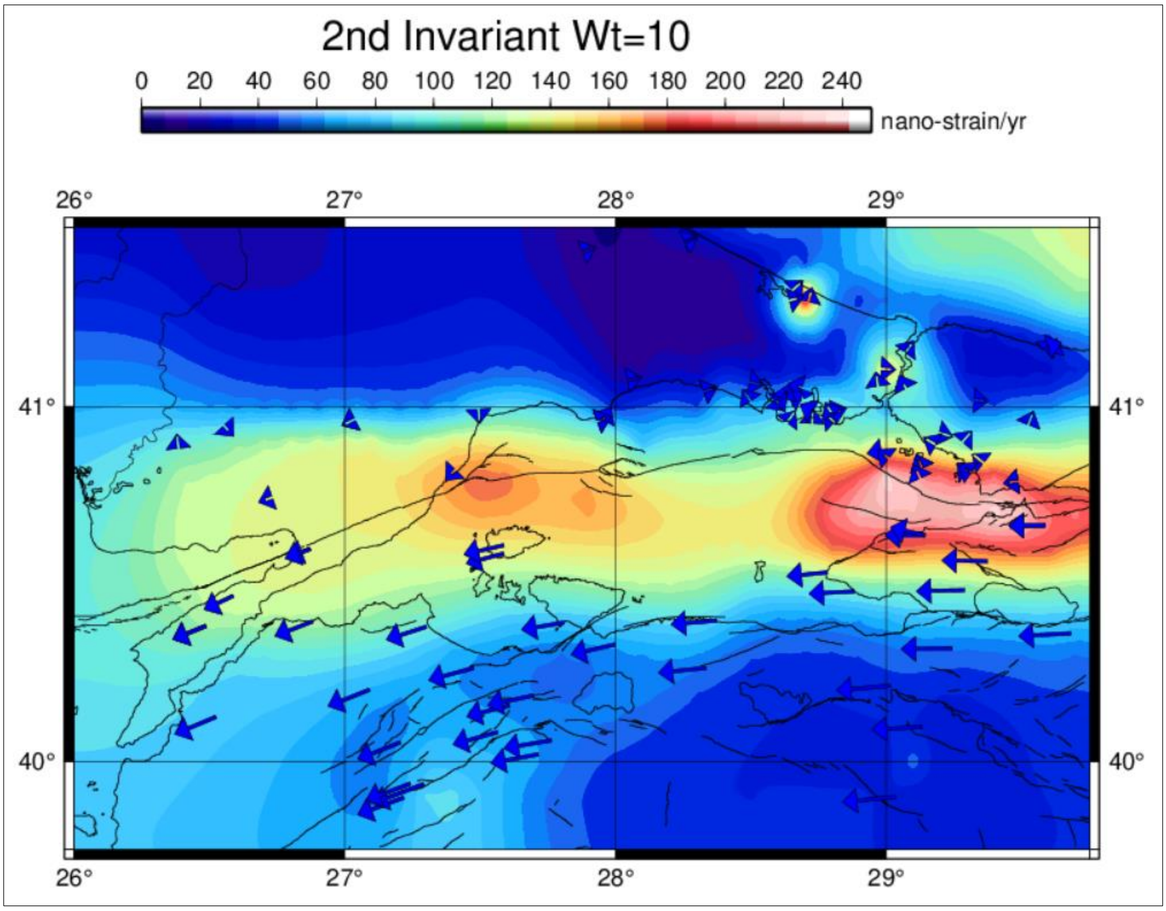

Figure 6.12. The Second Invariant of Strain Rates using Gaussian and Voronoi Cell Weighting Functions with net weighting thresholds set as Wt=10.

6.5.3. Uncertainty and Resolution

In the method of Shen et al. (2015) several parameters are important in assessing the quality of strain-rate estimation. Shen et al. (2015) states that the formal uncertainty cannot be directly used, in a classic sense, to measure the quality of the result. In this method, the uncertainties are smaller in regions in which the data distributions are sparser.

Shen et al. (2015) point out that “such uncertainties are measures of averaged strain rates, which are strongly affected by the degree of smoothing imposed on the data. As the degree of smoothing varies spatially, assessment of the spatial distribution of the smoothing range becomes a crucial part for the evaluation of real strain-rate uncertainties”.

Figure 6.13 shows the Gaussian smoothing coefficient D used in reweighting, which is a measure of the range of smoothing involved in the calculation using different net weighting thresholds Wt. Thus, instead of formal uncertainty σ spatial variations in the smoothing coefficient D represents better the solution quality. Shen et al. (2015) further states that the D parameter “can be regarded as a measure of the in situ data strength because it is reciprocally proportional to data density, and reflects spatial resolution of the result. For the assessment of quality of strain-rate interpolation result, it is more practical and useful to assess the relative resolution”, as shown in Figure 6.13.

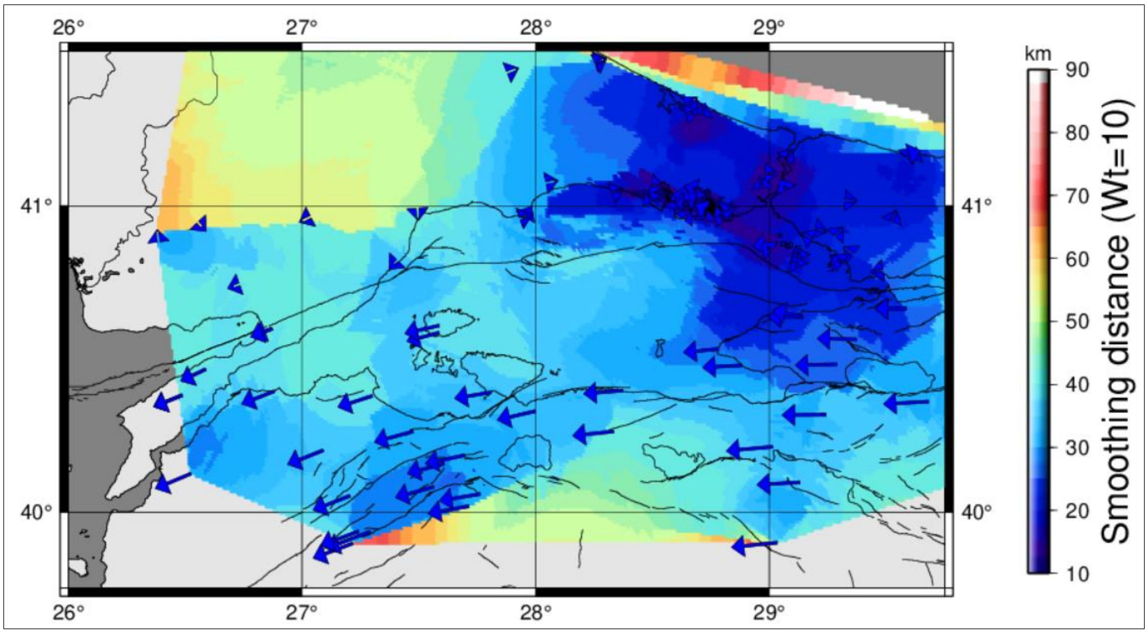

Figure 6.13. The smoothing distance D (background) using Gaussian and Voronoi cell weighting functions with the net weighting threshold set as Wt=10.

6.5.4. Style of Strain Rate Tensor Results

The strain rate tensor style S can be used to determine the type of tectonic regime prevailing in a region. The predominant compressional regions correspond to areas where S < −0.5, the strike-slip regime is characterized by 0.5 < S < −0.5, and extension is represented by S > 0.5. The spatial variations in the style of strain rate tensor is shown in Figure 6.14, where distinct tectonic features can be easily noticed. Extensional and strike-slip style dominate Marmara region, while compression features are rare.

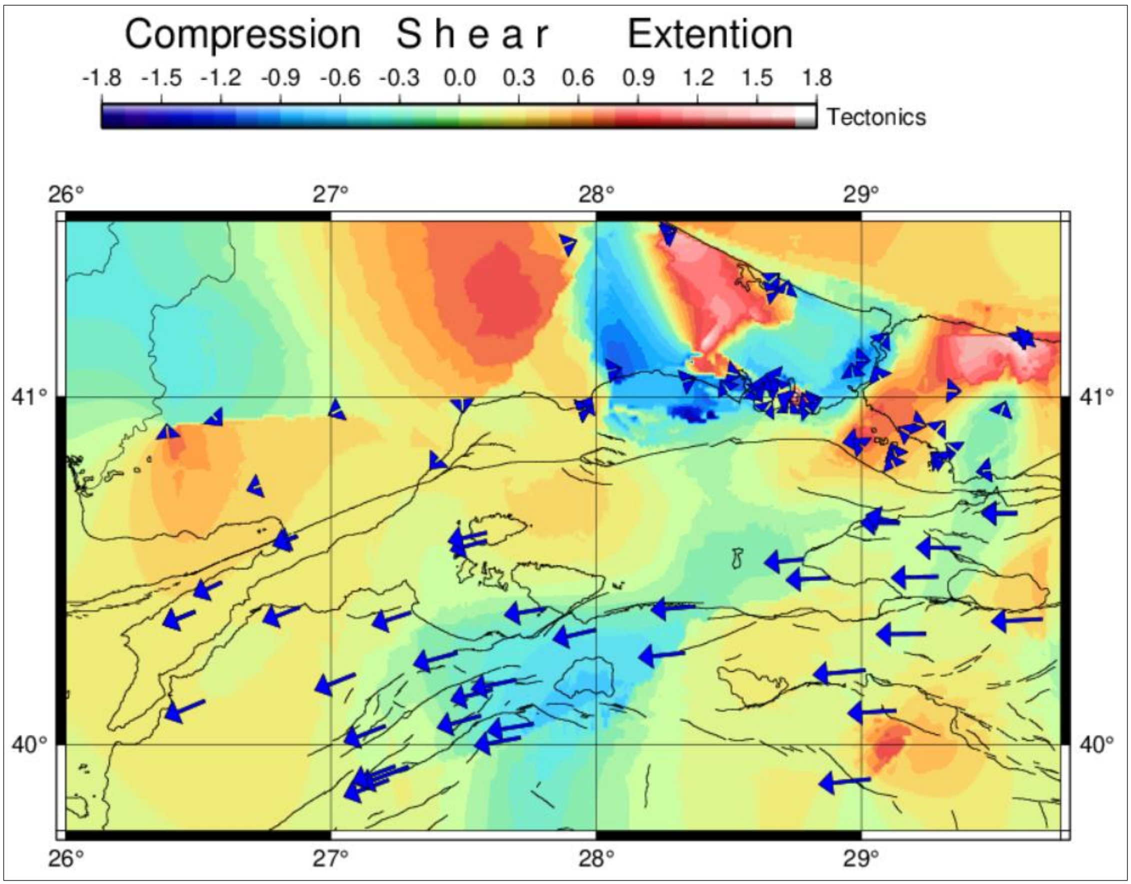

Figure 6.14. The Strain Rate Tensor Style S.

6.5.5. Dilatation Results

The dilatation strain rate map is shown in Figure 6.15. Positive and negative dilatation corresponds to elongation or extension and shortening or contraction, respectively. The background colored image is the dilatation strain rate. The lines indicate the orientation of the principal strain axis (see the legend for details). When the size of the minimum principal strain axis is larger than the size of the maximum principal strain axis, extension, or elongation occurs. On the contrary, when the maximum principal strain axes are larger than the minimum principal strain axes, compression dominates.

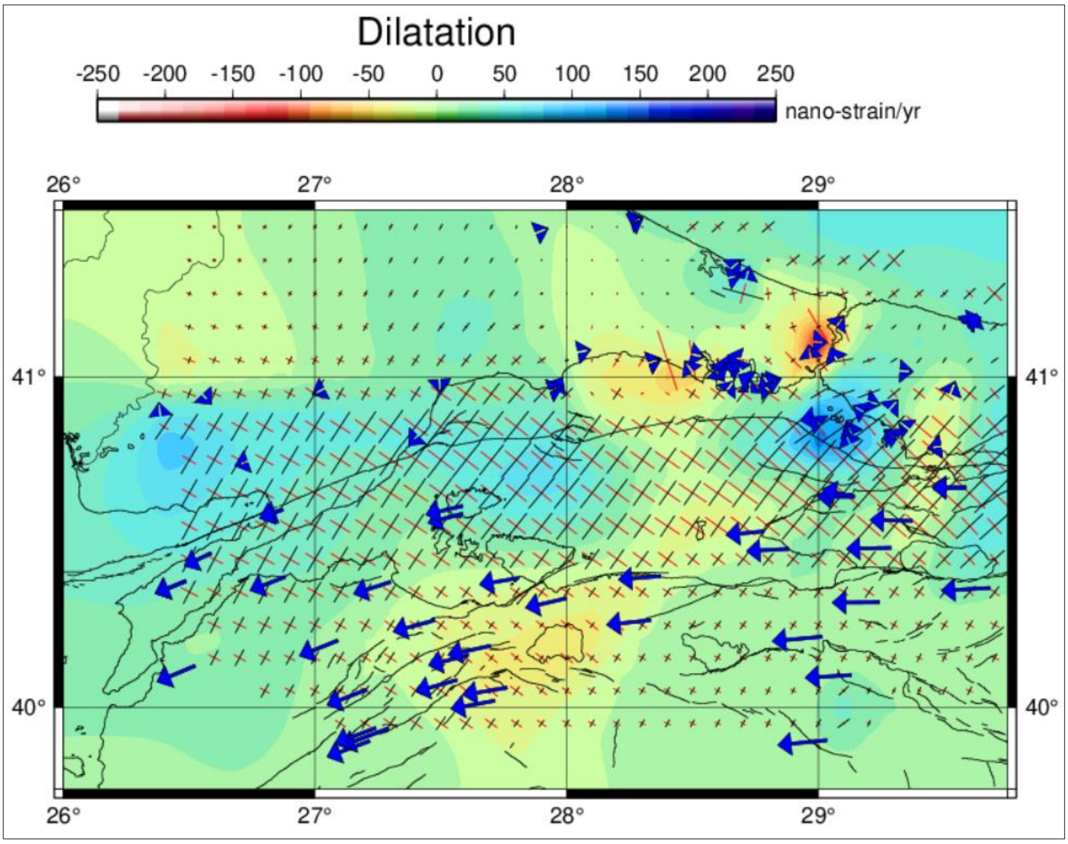

Figure 6.15. Dilatation Strain Rate Map (background). Positive Dilatation corresponds to Extension and Negative to Compression. The orientation of the minimum and maximum Principal Strain Rate Axis are shown with black and red lines, respectively.

<u>6.5.5.1. Extensional Features.</u> The dilation strain rates of positive and negative regions in Marmara Sea region are depicted, suggesting elongation and contraction of the crust coexist (see Figure 6.15). Significant elongation is observed in Çınarcık Basin and the area between Marmara Island and Central Basin. Moreover, the dilatation map depicts elongations in the area to the north of Saros Bay.

The background color in the dilatation map indicates the strainrate map. However, the maximum and minimum principal strain axes identify the direction of extension and compression. The minimum horizontal principal strain axes oriented NE-SW, but the maximum strain axes is NW-SE oriented in almost entire Marmara Sea (see Figure 6.15). Such features have been also derived from the stress tensor inversion of the focal mechanisms.

6.5.5.2. Compressional Features. Compressional or transpressional features is also derived for some locations in Marmara region (see Figure 6.15). The Central segment extending from Central Basin toward Çınarcık Basin eastward is an example of such contraction area. It should be noted that the 26 September 2019 event of Mw=5.7 took place in the area to the east of the Central Basin showing predominantly oblique reverse faulting mechanisms. Similarly, the area to the west of Marmara Island and Ganos also point out contraction where several reverse faulting mechanism have been obtained from the seismological data (Figure 6.15).

6.5.6. Shear Strain Rate Results

The directions of maximum shear strain give the possibility to define the directions of the strike-slip faults. The definitions for the maximum shear strain rate and its direction were previously introduced (Ashurkov et al., 2016). An assessment of the maximum shear strain rates is shown in Figure 6.16, where the background colors depict the size of the shear strain rate, and the axis orientations denote the strike of the right-lateral and left-lateral strike-slip faults. Also, shown are the optimally oriented right-lateral and left-lateral strike slip faults in Figure 6.16.

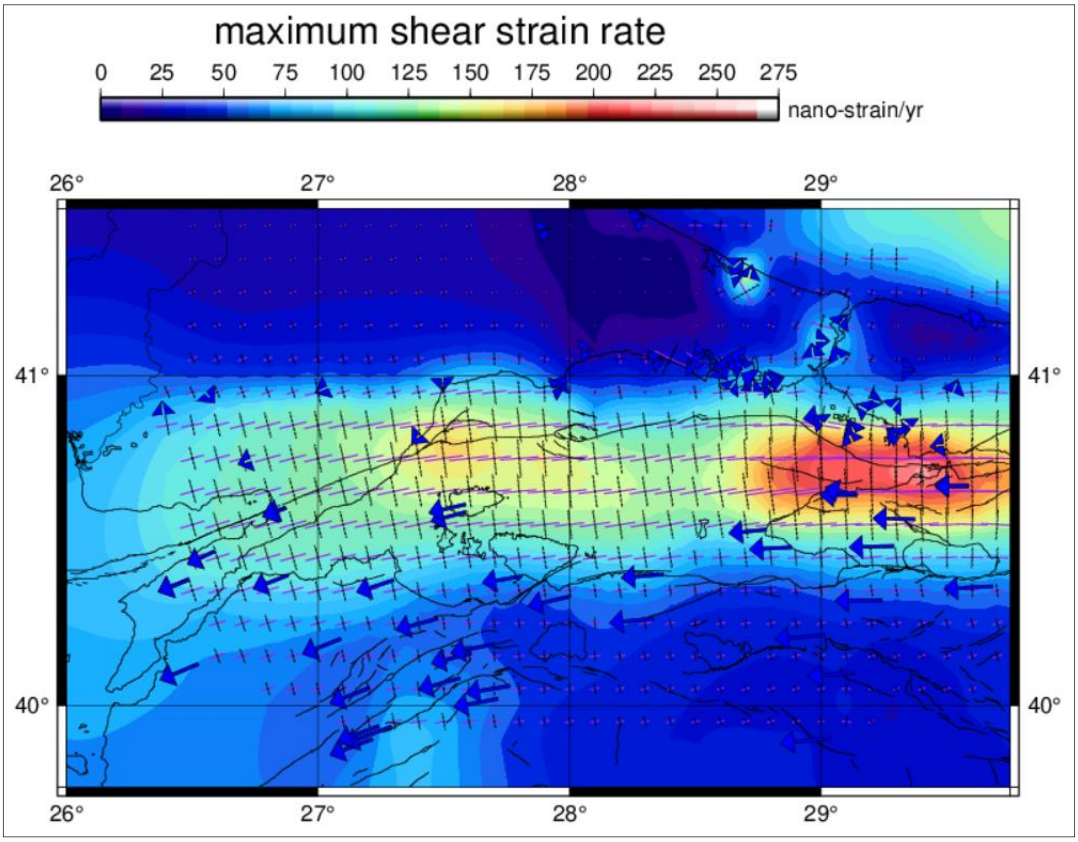

Figure 6.16. Shear Strain Rates (background) and the Strike Directions for optimally oriented Right Lateral (red) and Left Lateral (white) Strike Slip Faults.

6.5.7. Geodetic Moment Rate Results

As illustrated in Figure 6.5, Kostrov's (1974) formula is the tie between the summed moment tensors and geodetic strain rate within an area A. In order to evaluate geodetic moment rates in the study region, a scalar version of Eq (6.2) is used to as (Ward, 1998),

$$\dot{M}_{geodetic} = 2\mu A H_s \, \dot{\varepsilon}_{max} \tag{6.17}$$

where μ is the rigidity (3 x 10 ^{11} dyne/cm^2), A is the area (L x W) (see Chapter 6.3), H_s is the seismogenic thickness (see Chapter 6.3), and $\dot{\varepsilon}_{max}$ is the average maksimum geodetic strain (Figure 6.12). The results are shown in Table 6.7.

Table 6.7. Geodetic moment rate results in the region

Region	Area, km^2	H_s , km	$\dot{\varepsilon}_{max}$, 10^{-8}/y	$\dot{M}_{geod}$, 10^{24}dyne-cm/y
Ganos	1034	12	17.5	**1.2**
Western Marmara	2303	13	16.0	**2.9**
Central Marmara	2538	8	11.0	**1.3**
Çınarcık	1739	13	23.0	**3.1**

6.6. Geologic Strain Rate and Moment Rate

Kostrov's (1974) formula enable to translate the strain rates calculated for over an area A into potential moment release rates ($\dot{M}_s$) as,

$$\dot{M}_s = 2\mu A H_s \dot{\varepsilon} \quad (6.18)$$

The geological strain rate $\dot{\varepsilon}$ is calculated using geologically determined slip rate $\dot{s}_{geol}$ as

$$\dot{\varepsilon}_{geol} = \dot{s}_{geol} / 2W \quad (6.19)$$

Definitions (6.18) and (6.19) together produce (6.20) that line up with the conventional relation between fault surface area, fault slip velocity and moment rate (Ward, 1994),

$$\dot{M}_{geol} = 2\mu A H_s \dot{\varepsilon}_{geol} = 2\mu L W H_s [\dot{s}_{geol}/2W] = \mu L H_s \dot{s}_{geol} \quad (6.20)$$

6.6.1. Geologic Data

The geological slip rates ($\dot{s}_{geol}$) that are used to evalue the geological strain rates and moment rates along the segments of NAF in the Sea of Marmara are compiled from various palesoseismic investigations. The geological slip rates are shown in Table 6.8.

Table 6.8. Geological slip rates compiled from palesoseismic investigations

Region	Geological Slip Rate mm/yr	Timescale Span years	Technique	Source
Ganos	17±5	last 1000	Trenching	Meghraoui et al., 2012
Western Marmara	15.1-19.7	100.000-400.000	Offset buried morphology	Grall et al., 2013; Kurt et al., 2013
Central Marmara	9-10	since 12000	Offset seafloor morphology	Polonia et al., 2004; Gasperini et al., 2011; Grall et al., 2013
Çınarcık	12.6-29	100.000-400.000	Offset buried morphology	Grall et al., 2013; Kurt et al., 2013

6.6.2. Geologic Strain Rate and Moment Rate Results

Following equation (6.19) geologic strain rates are calculated using geologic slip rates given in Table 6.9.

Table 6.9. Geologic strain rate results in the region

Region	$\dot{s}_{geol}$, mm/yr	W, km	$\dot{\boldsymbol{\varepsilon}}_{geol}$, $\mathbf{10^{-8}/y}$
Ganos	17.0	47	**18.0**
Western Marmara	17.4	47	**18.5**
Central Marmara	9.5	47	**10.1**
Çınarcık	18.5	47	**19.7**

Geologic moment rates ($\dot{M}_{geol}$) are calculated following equation (6.20). The rigidity μ is taken as 3 x 10 ^{11} dyne/cm^2, L is the fault length, H_s is the seismogenic thickness. The results are shown in Table 6.10.

Table 6.10. Geologic moment rate results in the region

Region	L, km	H_s , km	$\dot{s}_{geol}$, mm/yr	**$\dot{M}_{geol}$, 10^{24}dyne-cm/y**
Ganos	20	12	17.0	**1.2**
Western Marmara	50	13	17.4	**3.4**
Central Marmara	54	8	9.5	**1.2**
Çınarcık	37	13	18.5	**2.7**

6.7. Seismic Moment Release and Moment Rate of Historical Earthquakes in the Segments of the NAF in the Sea of Marmara

The Marmara region has one of the longest and extensive historical records of large earthquakes in the world (Ambraseys and Finkel, 1987, Ambraseys and Finkel, 1991, Ambraseys and Finkel, 1995, Ambraseys, 2002). The historical earthquakes records provide invaluable information for understanding the behavior of fault over multiple earthquake cycle.

In this study the historical earthquake catalog covering the seismicity over the last 1500 years by Ambraseys, 2002 (Figure 6.17) is used in order to calculate the seismic moment rate in the sections of NAF in the Sea of Marmara.

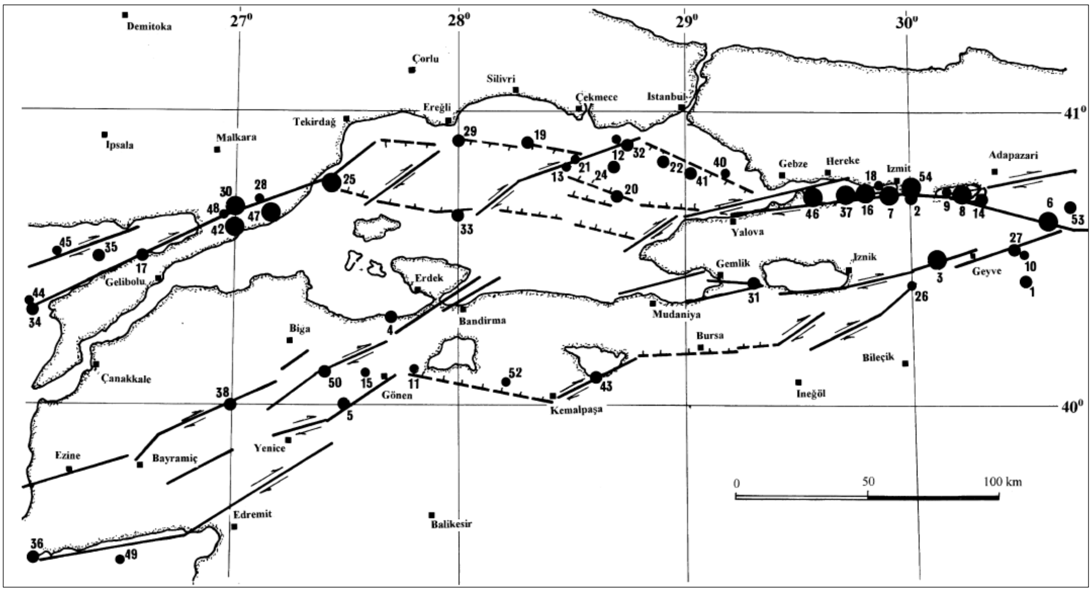

Figure 6.17. Epicentral regions of *Ms* ≥6.8 events occurred in historical period between 1-1899 and epicenters of earthquakes after instrumental period (Ambraseys, 2002).

Ganos Area

The historical events listed in Table 6.11 are used in order to calculate the total moment release and moment rate along the Ganos segment of the NAF. The cumulative seismic moment release over 1410 years is shown in Figure 6.18. The cumulative seismic moment release is calculated as 6.7 x 10^{27} dyne-cm and seismic moment rate as 4.7 x 10^{24} dyne-cm/yr.

Table 6.11. Historical large earthquakes in Ganos Area over the last 1500 years

No	Year	Date	Lat	Long	Ms	Mo, dyne-cm
17	484	0	40.50	26.60	7.2	7.07E+26
25	989	10	40.80	28.70	7.2	7.07E+26
28	1296	6	40.50	30.50	7.0	3.54E+26
30	1343	10	40.90	28.00	7.0	3.54E+26
34	1509	9	40.90	28.70	7.2	7.07E+26
35	1556	5	40.60	28.00	7.1	5.00E+26
42	1754	9	40.80	29.20	6.8	1.77E+26
44	1766	8	40.60	27.00	7.4	1.41E+27

45	1855	2	40.10	28.60	7.1	5.00E+26
47	1893	2	40.50	26.20	6.9	2.51E+26
48	1894	7	40.70	29.60	7.3	9.99E+26

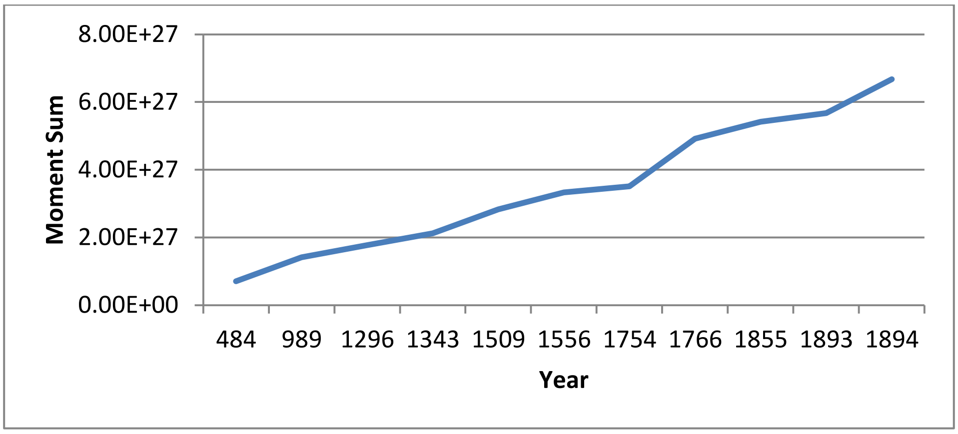

Figure 6.18. Cumulative seismic moment release in Ganos area versus time for the events listed in Table 6.11.

Western Marmara Segment

As shown in Figure 6.17 and Table 6.12, two historical earthquakes occurred in 1343 and 1489 are located in Western segment of NAF. Since the magnitude of 1489 event in Ambraseys 2002 catalogue is unestimated, Mw estimation for 1489 event is used in the SHARE European Earthquake Catalogue (SHEEC) and Mw-Ms conversion is done using the empirical magnitude conversion equation by Akkar et al., 2010.

The cumulative seismic moment release over 146 years is calculated as 2.8 x 10^{26} dyne-cm and seismic moment rate as 1.9 x 10^{24} dyne-cm/yr.

Table 6.12. Historical Large Earthquakes in Western Marmara Segment over the last 1500 years

No	Year	Date	Lat	Long	Ms	Mo, dyne-cm
29	1343	10	40.70	27.10	6.9	2.50E+26
33	1489	1	0.00	0.00	6.3	3.16E+26

Central Marmara Segment

The historical events listed in Table 6.13 are used in order to calculate the total moment release and moment rate along the Central Marmara segment of the NAF. The cumulative seismic moment release over 1012 years is shown in Figure 6.19. The cumulative seismic moment release is calculated as 1.3 x 10^{27} dyne-cm and seismic moment rate as 1.3 x 10^{24} dyne-cm/yr.

Table 6.13. Historical large earthquakes in Central Marmara Segment over the last 1500 years

No	Year	Date	Lat	Long	Ms	Mo, dyne-cm
12	407	4	40.90	28.70	6.8	1.78E+26
13	437	9	40.80	28.50	6.8	1.78E+26
19	557	12	40.90	28.30	6.9	2.51E+26
21	823	10	0.00	0.00	0.0	1.12E+16
32	1419	3	40.40	29.30	7.2	7.07E+26

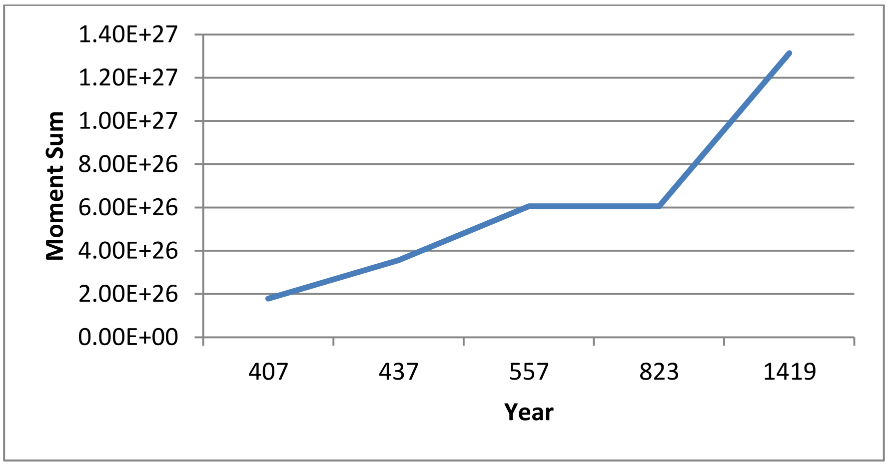

Figure 6.19. Cumulative seismic moment release in Central Marmara segment versus time for the events listed in Table 6.13.

Çınarcık Segment

The historical events listed in Table 6.14 are used in order to calculate the total moment release and moment rate along the Çınarcık segment of the NAF. The cumulative seismic moment release over 1012 years is shown in Figure 6.20. The cumulative seismic moment release is calculated as 1.9 x 10^{27} dyne-cm and seismic moment rate as 1.9 x 10^{24} dyne-cm/yr.

Table 6.14. Historical large earthquakes in Çınarcık Segment over the last 1500 years

No	Year	Date	Lat	Long	Ms	Mo, dyne-cm
20	740	10	40.70	28.70	7.1	5.01E+26
22	860	5	40.80	28.50	6.8	1.78E+26
24	967	9	40.70	31.50	7.2	7.07E+26
40	1737	3	40.00	27.00	7.0	3.54E+26
41	1752	7	41.50	26.70	6.8	1.78E+26

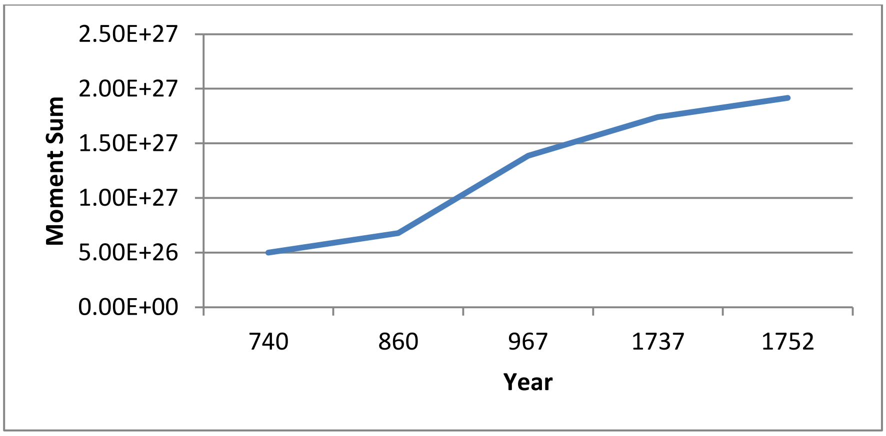

Figure 6.20. Cumulative seismic moment release in Çınarcık segment versus time for the events listed in Table 6.14.

6.8. Comparison of Seismic, Geodetic and Geologic Strain and Moment Rates

In each section above, strain rates and moment rates in each segment of NAF in the Marmara Sea are estimated from the seismological, geodetical and geological aspects. Since strain rates and moment rates are derived from different perspective of the earthquake engine, each of them illuminates different features.

$M_{seismic}$ takes into account only buried faults and presents just the seismic component of deformation. Besides it suffers from the completeness of the seismic catalogues. $M_{geodetic}$ takes into account all contributing sources of deformation in the region. However it cannot discriminate aseismic from seismic strain. $M_{geodetic}$ takes into account only known faults but since it provides thounds years of geological history data, it doesn't affected by the limitations of temporal sampling when compared to $M_{seismic}$ or $M_{geodetic}$ (Ward, 1998).

Table 6.15 shows the summary of calculated strain rate and moment rates using seismic, geodetic and geologic data. Moreover, Mw values are calculated for each segment corresponding to total moment rate in 250 years.

Table 6.15 Summary of seismic, geodetic and geologic strain and moment rates for each segment in the Sea of Marmara

Region	Seismic (Instrumental period)			Seismic (Historical period)		Geodetic			Geologic		
	$\acute{\varepsilon}$ 10^{-8}/y	M 10^{24} dyne-cm/yr	Mw	M 10^{24} dyne-cm/yr	Mw	$\acute{\varepsilon}$ 10^{-8}/y	M 10^{24} dyne-cm/yr	Mw	$\acute{\varepsilon}$ 10^{-8}/y	M 10^{24} dyne-cm/yr	Mw
Ganos	0.56	0.049	6.1	4.7	7.3	17.5	1.2	7.0	18.0	1.2	7.0
Western Marmara	0.45	0.088	6.2	1.9	7.1	16.0	2.9	7.2	18.5	3.4	7.3
Central Marmara	0.65	0.098	6.3	1.3	7.0	11.0	1.3	7.0	10.1	1.2	7.0
Çınarcık	2.77	0.57	6.8	1.9	7.1	23.0	3.1	7.3	19.7	2.7	7.2

7. DISCUSSIONS AND CONCLUSIONS

The compressional and extensional features together with the seismic activity beneath the Sea of Marmara and surroundings are examined using both seismological and geodetic data. Moreover, seismic, geodetic and geologic moment rates are estimated which provide valuable information about the seismic hazard of the regions.

The seismological data are gathered using two different data sets. Small to moderate size events are investigated using broadband stations operated by KOERI covering the period between 2002 and 2015. The microactivity in the Sea of Marmara is investigated by 15 OBS seismic stations deployed by JAMSTEC covering the period between September 2014 and June 2016. Focal mechanisms of small to moderate size events are determined using CMT inversion method. For the events recorded by OBS's, the P-wave polarity data is used for the simultaneous determination of stress tensor parameters and fault plane solutions for many earthquakes. For the events whose polarity data is not sufficient to constrain the focal mechanism by only OBS, the polarity data at land stations around the Marmara region are integrated. As a result of detailed analysis, a considerable amount of various types of focal mechanisms are observed which reveal the presence of a segmented fault system where restraining local stresses are developed. The results show that Tekirdag Basin, Western High and Central Basin are the most seismically active part in Marmara Sea when compared to eastern segments. The deepest events up to 20-24 km are also observed in Western High and Central Basin. The sparse seismicity beneath the Kumburgaz Basin, besides the high level of seismicity on both edges suggests that this section of the NAF is locked and so accumulating strain. The stress tensor acting on the NAF in the Sea of Marmara is determined by stress tensor inversion analysis. The results point out NW-SE oriented maximum compressive stress axis and NE-SW oriented minimum compressive stress axis in the study region.

The geodetic data is compiled from 112 GPS stations located around Marmara region. The observation period range from 1994 to 2013 station to station. The spatial variations in the style of strain rate tensor where distinct tectonic features can be easily noticed. Extensional and strike-slip style dominate Marmara region, while compression features are rare. Such features are also derived from the focal mechanism solutions obtained using seismological data. Significant elongation is observed in Çınarcık Basin and the area between Marmara Island and Central Basin. Moreover, the dilatation map depicts elongations in the area to the north of Saros Bay. The Central segment extending from Central Basin toward Çınarcık Basin eastward is an example of such contraction area. It should be noted that the 26 September 2019 event of Mw=5.7 took place in the area to the east of the Central Basin showing predominantly oblique reverse faulting mechanisms. Similarly, the area to the west of Marmara island and Ganos also point out contraction where several reverse faulting mechanism have been obtained from the seismological data.

The seismic strain rates for instrumental period are determined following Kostrov's (1974) formula, the GPS velocities are used to determine the geodetic strain rates, and the geologic slip rates determined from various paleoseismic studies are used to determine the geological strain rates in the region. Geodetic and geologic moment rates are determined using Kostrov's (1974) relation between geodetic strain rate and seismic moment rate, which was modified by Ward (1998), where seismic moment rates for instrumental period and historical period are extracted from earthquake catalogues.

According to the GPS strain rate results, the highest values, 24×10^{-8}/y, are observed in Çınarcık Basin, where the lowest values, 11×10^{-8}/y, are observed in Central Marmara. The highest values in both edges of the fault segment in Çınarcık Basin can be interpreted as this region is steadily creeping or alternatively tectonic loading is more effective. Vice versa lower strain rates in Central Marmara region suggest that this segment of NAF is locked.

The moment rate estimation results for each segment show that seismic moment rates, calculated for instrumental period, are greatly lower than geodetic and geologic moment rates. This can be interpreted in two ways: (1) action of aseismic strain release (creeping), (2) strain accumulation along fault segments. That is to say, the NAF in the Sea of Marmara is actively accumulating strain, but the only small portion of the accumulated seismic energy is relased by small magnitude events occuring in the region.

The moment rate results also show that the instrumental period data are not adequate enough to characterize the seismic hazard in the region. In other words, using seismic moment rate estimations calculated for only instrumental period events may lead unreliable results in seismic hazard studies. On the other hand, similar seismic moment rates obtained using historical period, geodetic and geologic data reveals that for regions where historical period data are sparse, geodetic and geologic data may also be used in seismic hazard analysis.

Seismic moment rates in the historical period for the last 1500 years shows that this region is capable of generating large magnitude events. Accordingly, the low seismic moment rates estimated in the instrumental period, when compared to geodetic and geologic moment rates, this shows us that seismic deformation accumulation is actively continues in Ganos, Western segment, Central segment and Çınarcık source zones.

The outcome of this study is based on 1 year OBS observations of microearthquakes, 13 years records of land seismic stations for small to moderate size events, and 1994-2013 GPS records around Marmara region. Longer term OBS and geodetic observations are needed in order to clarify the geometry of NAF in the Sea of Marmara, observe the behavior of sparse seismicity regions, and related moment rate deficit, which provides input for hazard and risk assessments of the region.

REFERENCES

Akartuna M., “Armutlu Yarımadasının Jeolojisi”, *İstanbul Üniv. Fen Fak. Monogr. (Tabii İlimler Kısmı)*, No. 20, 105 pp. +3 foldouts, 1968.

Aki, K., and P.G. Richards, 1980, *Quantitative Seismology Theory and Methods*, W.H.Freeman ve Co., 932 p. San Francisco, USA.

Akkar, S., Z. Çağnan, E. Yenier, Ö. Erdoğan, M.A. Sandıkkaya, P. Gülkan, “The recently compiled Turkish strong motion database: preliminary investigation for seismological parameters”, *Journal of Seismology*, 14, 457-479, 2010.

Aksu, A. E., T. J. Calon, R. N. Hiscott, D. Yaşar, “Anatomy of the North Anatolian fault zone in the Marmara Sea. Western Turkey: Extensional basins above a continental Transform”, *GSA Today,* 10, 1-2, 2000.

Ambraseys, N. N., “The seismic activity of the Marmara Sea region over the last 2000 years”, *Bull. Seism. Soc. Am*., 92, 1–18, 2002.

Ambraseys, N. N., and C. F. Finkel, “The Saros-Marmara earthquake of 9 August 1912”, *J. Earthq. Eng. Struct. Dyn*.,15, 189–211, 1987.

Ambraseys, N. N., and C. F. Finkel, “The Marmara Sea Earthquake of 1509”, *Terra Nova*, 2, pp. 167-174, 1990.

Ambraseys, N. N., and C. F. Finkel, “Long-term seismicity of Istanbul and the Marmara Sea region”, *Terra Nova,* 3, pp. 527-539, 1991.

Ambraseys, N. N., and C. F. Finkel, “The Seismicity of Turkey and Adjacent Areas”, *a Historical Review,* 1500-1800, 240 pp., Eren, İstanbul, 1995.

Ambraseys, N. N., and J. A. Jackson, “Seismicity of the Sea of Marmara (Turkey) since 1509”, *Geophys J. Int.*, 141, F1-F6, 2000.

Armijo, R., B. Meyer, A. Hubert-Ferrari, and A. Barka, “Westward propagation of North Anatolian Fault into the Northern Aegean: timing and kinematics” *Geology*, 27: 267–70, 1999.

Armijo, R., B. Meyer, S. Navarro, G. King, A. Barka, “Asymmetric slip partitioning in the Sea of Marmara pull apart: a clue to propagation processes of the North Anatolian fault”, *Terra Nova*, 14:80–86, 2002.

Armijo, R., et al., “Submarine fault scarps in the Sea of Marmara pull-apart (North Anatolian Fault): Implications for seismic hazard in Istanbul”, Geochem. Geophys. Geosyst., 6, Q06009, doi:10.1029/2004GC000896, 2005.

Ashurkov, S.V., V.A San’Kov, M.A. Serov, P.Y. Luk’Yanov, N.N. Grib, G.S. Bordonski, and M.G. Dembelov, “Evaluation of presentday deformations in the Amurian Plate and its surroundings, based on GPS data”, *Russian Geology and Geophysics*, 57, 1626–1634, 2016.

Barka, A. A., “The North Anatolian fault zone”, *Annales Tectonicae*, Special Issue, VI suppl., 164–195, 1992.

Barka, A. A., “Slip distribution along the North Anatolian fault associatedwith the large earthquakes of the period 1939 to 1967”, *Bull. Seismol. Soc.Am.*,86, 1238–1254, 1996.

Barka, A.A., and K. Kadinky-Cade, “Strike-slip fault geometry in Turkey and its influence on earthquake activity”, *Tectonics*, 7, 663-684, 1988.

Barka, A., H.S. Akyüz, H.A. Cohen, F. Watchorn, “Tectonic evolution of the Niksar and Tasova-Erbaa pull-apart basins, North Anatolian Fault Zone: their significance for the motion of the Anatolian Block”, *Tectonophysics*, 322:243–64, 2000.

Bath, M., and S. J. Duda, “Earthquake volume, fault plane area, seismic energy strain, deformation, and related quantities”, *Ann. Geofis. Rome*, 17, 353-368, 1964.

Bayrakci, G., M. Laigle, A. Bécel, A. Hirn, T. Taymaz, S. Yolsal-Cevikbilen, SEISMARMARA team, “3-D sediment-basement tomography of the Northern Marmara trough by a dense OBS network at the nodes of a grid of controlled source profiles along the North Anatolian fault”, *Geophys. J. Int.*, 194:1335-1357, 2013.

Becel, A., et al., “Moho, crustal architecture and deep deformation under the North Marmara Trough, from the SEISMARMARA Leg 1 offshore–onshore reflection–refraction survey”, *Tectonophyics*, 467:1–21, 2009.

Bellier, O., S. Över, A. Poisson, J. Andrieux, “Recent temporal change in the stress state and modern stress field along the North AnatolianFault Zone (Turkey)”, *Geophys. J. Int.*, 131:61–86, 1997.

Berberian, M., “Master Blind Thrust Faults Hidden under the Zagros Folds: Active Basement Tectonics and Surface Morphotectonics”, *Tectonophysics Journal*, 241, 193-224, 1995.

Bock, G., *Source parameters and moment-tensor solutions. - In: Bormann, P. (Ed.), New Manual of Seismological Observatory Practice 2 (NMSOP-2*), Potsdam: GFZ, pp. 1-14, doi: http://doi.org/10.2312/GFZ.NMSOP-2_IS_3.8, 2012.

Bohnhoff, M., F. Bulut, G. Dresen, P.E. Malin, T. Eken, M. Aktar, “An earthquake gap south of Istanbul”, *Nature Communications*, 4, 1999, doi:10.1038/ncomms2999, 2013.

Bohnhoff, M., P. Martínez-Garzón, F. Bulut, E. Stierle, and Y. Ben-Zion, “Maximum earthquake magnitudes along different sections of the North Anatolian Fault zone”, *Tectonophysics*, 674, 147–165, doi:10.1016/j.tecto.2016.02.028, 2016.

Bozkurt, E., and A. Kocyigit, “Almus Fault zone: its age, total offset and relation to the North Anatolian Fault Zone”, *Turkish Journal of Earth Sciences*, 4:93-104, 1995.

Bozkurt, E., and A. Kocyigit, “The Kazova basin: An active negative flower structure on the Almus fault zone, a splay fault system of the NorthAnatolian Fault Zone, Turkey”, *Tectonophysics*, 265, 239–254, 1996.

Bulut, F., M. Bohnhoff, W. Ellsworth, M. Aktar, and G. Dresen, “Microseismicity at the North Anatolian fault in the Sea of Marmara offshore Istanbul, NW Turkey”, *J Res Geophys*., doi:10.1029/2008JB00624, 2009.

Carton, H., *Etudes tectonics en Mediterranee orientale par analyse dedonnées de sismique reflexion: Mer de Marmara Bassin de Çinarcik et merge du Liban*, PhD thesis, Institute De Physique Du Globe De Paris, 2005.

Carton, H., et al., “Seismic imaging of the three-dimensional architecture of the Çinarcik Basin along the North Anatolian fault” J Geophys Res 112:B06101. doi:10.1029/2006JB004548, 2007.

Christie-Blick, N., and K.T Biddle, “*Deformation and basin formation along strike-slip faults. In: Biddle, K.T. & Christieblick, N. (eds), Strike-Slip Faulting and Basin Formation*”, Society of Economic Paleontologists and Mineralogists, Special Publications 37, 1–34, 1985.

Cros, E., and L. Géli, “Characterisation of microseismicity in the Western Sea of Marmara: Implications in terms of seismic monitoring”, http://doi.org/10.13155/38916, 2013.

Cunningham, W.D., and P. Mann, “Tectonics of strike-slip restraining and releasing bends”, Geological Society, London, Special Publications, 290, 1-12, 2007.

D'Agostino, N., “Complete seismic release of tectonic strain and earthquake recurrence in the Apennines (Italy)”, *Geophysical Research Letters*, 41 (4), 1155-1162, 2014.

Demirbağ, E., C. Rangin, X. Le Pichon, A.M.C. Şengör, “Investigation of the tectonics of the Main Marmara Fault by means of deeptowed seismic data”, *Tectonophysics*, 361:1–19, 2003.

Devoti, R., G. Pietrantonio, A.R. Pisani, F. Riguzzi, “GNSS networks for geodynamicsin Italy”, *Fisica de la Tierra 26. Universidad Complutense de Madrid*, pp. 11–24 (http://revistas.ucm.es/index.php/FITE/article/view/46968), 2014.

Dewey, J. F., and A. M. C. Şengör, “Aegean and surrounding regions complex multiplate and continuum tectonics in a convergent zone”, *GSA Bull*., 90, 84–92, 1979.

Drab, L., A. Hubert-Ferrari., S. Schmidt, P. Martinez, J. Carlut and M. E. Ouahabi, “Sub-marine plaeo-earthquake record of the Cinarcik segment of the North Anatolian Fault in the Marmara Sea (Turkey)”, *Bull. Seismol. Soc. Am*., 105, 622-645, doi:10.785/0120130083, 2015.

Emre, Ö., T. Erkal, A. Tchepalyga, N. Kazanc, M. Keçer, and E. Ünay, “Neogene-Quaternary evolution of the eastern Marmara region, Northwest Turkey”, *Bull. Mineral Res. Explor. Inst. Turkey*, 120, 119–145, 1998.

England, P., and P. Molnar, “Active deformation of Asia: From kinematics to dynamics”, *Science*, 278, 647–650, 1997.

Erdik, M., “Report on 1999 Kocaeli and Duzce (Turkey) Earthquakes”, http://www.koeri.boun.edu.tr/depremmuh/eqspecials/kocaeli/Kocaelireport.pdf, 2000.

Ergintav, S., U. Doğan, C. Gerstenecker, R. Çakmak, A. Belgen, H. Demirel, C. Aydın, and R. Reilinger, “A snapshot (2003-2005) of the 3D postseismic deformation for the 1999, Mw=7.4 Izmit earthquake in the Marmara Region, Turkey, by first results of joint gravity and GPS monitoring”, *Journal of Geodynamics*, Vol. 44, pp. 1-18, 2007.

Ergintav, S., R. E. Reilinger, R. Çakmak, M. Floyd, Z. Cakir, U. Doğan, R. W. King, S. McClusky, and H. Özener, “Istanbul's earthquake hot spots: Geodetic constraints on strain accumulation along faults in the Marmara seismic gap", *Geophysical Research Letters*, 41, 5783–5788, https://doi.org/10.1002/2014GL060985, 2014.

ETHZ Lecture Notes, jbp 2017, Tectonics – Strike-slip faults: Strike-Slip and Oblique-SlipTectonics, http://www.files.ethz.ch/structuralgeology/JPB/files/English/5wrench.pdf, 2017.

Eyre, T. S., M. van der Baan, "Overview of moment-tensor inversion of microseismic events", *The Leading Edge*, 34(8):882–888, 2015.

Fraser, J., K. Vanneste, and A. Hubert-Ferrari, "Recent behavior of the North Anatolian Fault: Insights from an integrated paleoseismological data set", *J. Geopyhs. Res.*, 115, B09316, doi: 10.1029/2009JB006982, 2010.

Galadini, F., and P. Galli, "The Holocene paleoearthquakes on the 1915 Avezzano earthquake faults (central Italy): Implications for active tectonics in central Apennines", *Tectonophysics*, 308, 143–170, 1999.

Gephart, J.W., "FMSI: a Fortran program for inverting fault/slickenside and earthquake focal mechanism data to obtain the regional stress tensor", *Comput Geosci*, 16:953–989, 1990.

Gökten, E., R. Demirtaş, V. Özaksoy, E. Herece, B. Varol, and U. Temiz, "Faulting and Stress Distribution in the Bolu Pull-apart Basin (North Anatolian Fault Zone, Turkey): The Significance of New Dates Obtained from the Basin Fill", *Turkish J. Earth Sci.*, Vol.20, pp 1-26, 2011.

Görür, N., M.N. Çağatay, M. Sakınç, M. Sümengen, K. Şentürk, C. Yaltırak, A. Tchapalyga, "Origin of sea of Marmara as deduced from Neogene to Quaternary paleogeographic evolution of its frame", *International Geology Review*, 39, 342–352, 1997.

Gudmundsdottir, M. H., K. Blisniuk, Y. Ebert, N. M. Levine, D. H. Rood, A. Wilson, and G. E. Hilley, “Restraining Bend Tectonics in the Santa Cruz Mountains, California, Imaged Using 10Be Concentrations in River Sands” *Geology*, 41(8), 843-846, 2013.

Gürbüz C, M. Aktar, H. Eyidoğan, A. Cisternas, H. Haessler et al., “The seismotectonics of the Marmara region (Turkey): results from a macroseismic experiment”, *Tectonophysics*, 316:1–17, 2000.

Hackl, M., R. Malservisi, and S. Wdowinski, “Strain rate patterns from dense GPS networks”, *Natural Hazards and Earth System Sciences*, 9, 1177-1187, doi:10.5194/nhess-9-1177, 2009.

Harding, T. P., “Divergent wrench fault and negative flower structure, Andaman Sea, in Seismic expression of structural styles”, a picture and work atlas, *AAPG Studies in Geology 15*, v. 3, p. 4.2-1 to 4.2-8, 1983.

Harding T. P., “Seismic characteristics and identification of negative flower structures, positive flower structures, and positive structural inversion”, *AAPG Bulletin* 69:582–600, 1985.

Hartzell, S. H., and T. H. Heaton, “Inversion of strong ground motion and teleseismic waveform data for the fault rupture history of the 1979 Imperial Valley, California earthquake”, *Bulletin of the Seismological Society of America*, 73, 1553–1583., 1983.

Havskov, J., and L. Ottemoller, *Routine Data Processing in Earthquake Seismology: Wih Sample Data, Exercises and Software*, Springer, 219-220, 2010.

Hergert, T., O. Heidbach, A. Becel, and M. Laigle, “Geomechanical model of the Marmara Sea region -1. 3-D contemporary kinematics”, *Geophys. J. Int.*, 185, 1073–1089, 2011.

Herrmann, R. B., “SH-wave generation by dislocation sources – a numerical study”, *Bulletin of the Seismological Society of America*, 69, 1-15, 1979.

Horiuchi, S., G. Rocco, and A. Hasegawa, “Discrimination of fault planes from auxiliary planes based on simultaneous determination of stress tensor and a large number of fault plane solutions”, *J. Geophys. Res*., 100(5), 8327–8338, 1995.

Hubert-Ferrari, A., A. Barka, E. Jacques, S. Nalbant, B. Meyer, R. Armijo, P. Tapponnier, and G. P. King, “Seismic hazard in the Marmara sea region following the 17 August 1999 Izmit earthquake”, *Nature*, 404, 269-273, 2000.

Hubert-Ferrari, A., R. Armijo, G. King, B. Meyer, and A. Barka, “Morphology, displacement, and slip rates along the North Anatolian Fault, Turkey”, *J. Geophys. Res*., 107(B10), 2235, doi:10.1029/2001JB000393, 2002.

İmren, C., X. Le Pichon, X, C. Rangin, E. Demirbağ, B. Ecevitoğlu, and N. Görür, “The North Anatolian Fault within the Sea of Marmara: a new interpretation based on multi-channel seismic and multi-beam bathymetry data”, *Earth Planet. Sci. Lett.*, 186:143–58, 2001.

Kalafat, D., *Study of the tectonic structures in Anatolian based on fault mechanism 681 solutions*, PhD thesis, University of Istanbul, 217 pp. (in Turkish), 1995.

Kalafat, D., C. Gürbüz, S.B. Üçer, “Batı Türkiye’de Kabuk ve Üst Manto YapısınınAraştırılması”, *Deprem Araştırma Bülteni*, Sayı59: 43–64 (in Turkish), 1987.

Ketin İ., “Relations between general tectonic features and the main earthquake regions in Turkey”, *Bull. Miner. Res. Explor. Inst. Turk.* 71:63–67, 1968.

Kikuchi M, H. Kanamori, “Inversion of complex body waves-III”, *Bull. Seismol. Soc. Am.*, 81, 2335-2350, 1991.

Kohketsu, K., “The extended reflectivity method for synthetic near-field seismograms”, *J Phys Earth*, 33:121–131, 1985.

Kostrov, V. V., “Seismic Moment and Energy of Earthquakes, and Seismic Flow of Rocks”, Izv Acad. Sci. USSR, *Phys. Solid Earth English Trans.* 1: 23-44, 1974.

Kreemer, C., G. Blewitt, E.C. Klein, “A geodetic plate motion and Global Strain Rate Model”, *Geochemistry, Geophysics, Geosystems*, 15 (10): 3849-3889, 2014.

Kuge, K., “Source modeling using strong-motion waveforms: toward automated determination of earthquake fault planes and moment-release distributions”, *Bull Seismol Soc Am*., 93:639–654, 2003.

Kuge, K., H. Kawakatsu, “Significance of non-double couple components of deep and intermediate-depth earthquakes: implications from moment tensor inversions of long-period seismic waves”, *Phys. Earth Planet. Interior*, 75:243–266, 1993.

Kurt, H., et al., “Steady late quaternary slip rate on the Cinarcik section of the North Anatolian fault near Istanbul, Turkey”, *Geophys. Res. Lett*., 40, 4555–4559, doi:10.1002/grl.50882, 2013.

Laigle, M., A. Bécel, B. de Voogd, A. Hirn, T. Taymaz, S. Ozalaybey, the Members of the SEISMARMARA Leg1., “A first deep seismic survey in the Sea of Marmara: whole crust and deep basins”, *Earth Planet Sci Lett,* 270:168–179, 2008.

Lange, D., H. Kopp, J.Y. Royer, P. Henry, Z. Cakir, F. Petersen, L. Geli, “Interseismic strain build-up on the submarine North Anatolian fault offshore Istanbul”, *Nat Commun*, 10(1):9, 2019.

Lawson, C. L., and R. J. Hanson, *Solving Least Squares Problems*, SIAM, Philadelphia, 1974.

Lee, WHK., and J.C. Lahr, *HYPO71 : a computer program fordetermining hypocenter, magnitude and first-motion patternof local earthquakes*, U.S. Geological survey open-file report,pp. 100, 1972.

Le Pichon, X., T. Taymaz, A.M.C. Şengör, “The Marmara Fault and the Future Istanbul Earthquake”, *Proceedings of ITU-IAHS, International Conference on the Kocaeli Earthquake 17 August 1999, İstanbul, Turkey, 1999* December 2–5, pp.41–54, 1999.

Le Pichon, X., T. Taymaz, A.M.C. Şengör, “Important problems to be solved in the Sea of Marmara (NW-Turkey)”, *NATO Advanced Research Seminar: Integration of Earth Sciences Research on the 1999 Turkish and Greek Earthquakes and Needs for Future Cooperative Research, Istanbul, Turkey, May 14–17, 2000*. Abstract Book: pp. 66–67, 2000.

Le Pichon, X., A.M.C. Sengör, E. Demirbag, C. Rangin, C. Imren et al., “The active main Marmara Fault”, *Earth Planet Sci Lett*, 192:595–616, 2001.

Le Pichon, X., N. Chamot-Rooke, C. Rangin, A. M. C. Sengör., “The North Anatolian fault in the Sea of Marmara”, *J. Geophys. Res*., 108(B4), 2179, doi:10.1029/2002JB001862, 2003.

Le Pichon, X., C. Imren, C. Rangin, A. C., Şengör, and M. Siyako, “The South Marmara Fault”, *International Journal of Earth Sciences*, 103(1), 219-231, 2014.

Lida, K., “Earthquake magnitude, earthquake fault and source dimensions”, Nagoya Univ., *Jour. Earth. Sci*., v.13, no.2, p. 115-132, 1965.

Maeda, N., “A method for reading and checking phase time in autoprocessing system of seismic wave data”, *Zisin*, 38, 365–379, 1985.

McKenzie, D. P., “Active tectonics of the Mediterranean region”, *Geophys. J. R. Astron. Soc.*, 30:109–85, 1972.

Meade, B.J., B.H. Hager, S.C. McClusky, R.E. Reilinger, S. Ergintav, O. Lenk, A. Barka, and H. Ozener, “Estimates of seismic potential in the Marmara region from block models of secular deformation constrained by GPS measurements”, *Bull. Seismol. Soc. Am.*, 92, 208– 215, 2002.

Meghraoui, M., M. E. Aksoy, H. S. Akyüz, M. Ferry, A. Dikbaş, and E. Altunel, “Paleoseismology of the North Anatolian Fault at Güzelköy (Ganos segment, Turkey): Size and recurrence time of earthquake ruptures west of the Sea of Marmara”, *Geochem. Geophys. Geosyst.*, 13, Q04005, doi:10.1029/2011GC003960, 2012.

Middleton, T. A., B. Parsons, and R. T. Walker, “Comparison of seismic and geodetic strain rates at the margins of the Ordos Plateau, northern China”, *Geophys. J. Int.*, 212, 988-1009, 2018.

MIT Structural Geology Lecture Notes,12.113 Structural Geology, Part 5: Strike-slip faulting, Fall 2005, https://ocw.mit.edu/courses/earth-atmospheric-and-planetary-sciences/12-113-structural-geology-fall-2005/lecture-notes/part5_str_slp_fl.pdf, 2005.

Mount, V.S., and J. Suppe, “State of stress near the San Andreas fault: Implications for wrench tectonics”, *Geology*, 15, 1143-1146, 1987.

Mulargia, F., R. J. Geller, *Earthquake Science and Seismic Risk Reduction*, Kluwer Academic Publishers, Dordrecht, 2003.

Nelson, J. O., and H. F. Krausse, “The Cottage Grove fault system in southern Illinois”, *Illinois Geological Survey Circular*, 522,65 p, 1981.

Okay, A. İ., E. Demirbağ, H. Kurt, N. Okay, İ. Kuşcu, “An active, deep marine strike–slip basin along the North Anatolian Fault in Turkey”, *Tectonics*, 18, 129–148, 1999.

Okay, A., A. Kaslilar-Özcan, C. Imren, A. Boztepe-Güney, E. Demirbag, İ. Kusçu, “Active faults and evolving strike-slip basins in the Marmara Sea, northwest Turkey: a multichannel seismic reflection study”, *Tectonophysics*, 321:189–218, 2000.

Okay, A., O. Tüysüz, and S. Kaya, “From transpression to transtension: changes in morphology and structure around a bend on the North Anatolian Fault in the Marmara region”, *Tectonophysics*, 391, 259–282, 2004.

Öztürk A., “Ladik-Destek yöresinin tektoniği”, *Türk. Jeol. Kurumu Bül*., 23:31–38, 1980.

Palumbo, L., L. Benedetti, D. Bourle, A. Cinque, R. Finkel, “Slip history of the Magnola fault (Apennines, Central Italy) from 36Cl surface exposure dating: evidence for strong earthquakes over the Holocene”, *Earth Planet. Sci. Lett*., 225, 163–176, 2004.

Pantosti, D., D.P. Schwartz, G. Valensise, “Paleoseismology along the 1980 surface rupture of the Irpinia fault: implications for earthquake recurrence in the southern Apennines, Italy”, *Journal of Geophysical Research*, 98 (B4): 6561-6577, 1993.

Parke, J. R., T. A. Minshull, G. Anderson, R.S. White, D. McKenzie, I. Kuscu, J. M. Bull, N. Gorur and C. Sengor, “Active faults in the Sea of Marmara, Western Turkey, imaged by seismic reflection profiles”, *Terra Nova*, 11, 223-227, 1999.

Parke, J. R., R. S. White, D. McKenzie, T. A. Minshull, J. M. Bull, I. Kuscu, N. Gorur and C. Sengor, “Interaction between faulting and sedimentation in the Sea of Marmara, western Turkey”, *Journal of Geophysical Research*, 107(B11), 2286, doi:10.1029/2001JB000450, 2002.

Pinar, N., *Marmara Denizi Havzasının Sismik Jeoloji ve Meteorolojisi/Géologie et Météorologie Sismique du Bassin de Mer Marmara*, PhD Thesis, Inst. Géol., Inst. Phys. Gén. Univ. İstanbul, Kenan Matbaası. 63 pp.+1 foldout map, 1943.

Pinar, A., K. Kuge, and Y. Honkura, “Moment tensor inversion of recent small to moderate sized earthquakes: Implications for seismic hazard and active tectonics beneath the Sea of Marmara”, *Geophys. J. Int.*, 153, 133– 145, doi:10.1046/j.1365-246X.2003.01897.x, 2003.

Pinar, A., Z. Coşkun, A. Mert, and D. Kalafat, “Frictional strength of North Anatolian fault in eastern Marmara region”, *Earth Planet Space*, 68-62, https://doi.org/10.1186/s40623-016-0435-z, 2016.

Polat, A., O. Tatar, H. Gürsoy, C. Ç. Yalçiner, and A. Büyüksaraç, “Two-phased evolution of the Suşehri Basin on the North Anatolian Fault Zone, Turkey”, *Geodinamica Acta*, 25:3-4, 132-145, DOI: 10.1080/09853111.2013.861997, 2012.

Rangin, C., E. Demirbag, C. Imren, A. Crusson, *Marine Atlas of the Sea of Marmara (Turkey)*, Ifremer, Plouzan´e, France, 2001.

Rangin, C., X. Le Pichon, E. Demirbağ, C. Imren, “Strain localization in the Sea of Marmara: propagation of the North Anatolian Fault in a now inactive pull-apart”, *Tectonics*, 23, doi:10.1029/2002TC001437, 2004.

Reilinger, R., S. McClusky, P. Vernant, S. Lawrence, S. Ergintav, R. Cakmak, F. Kadirov, I. Guliev, et al., “GPS constraints on continental deformation in the Africa-Arabia-Eurasia continental collision zone and implications for the dynamics of plate interactions”, *J. Geophys. Res*., 111, B05411, doi:10.1029/2005JB004051, 2006.

Roberts, M. T., “Seismic example of complex faulting from northwest shelf of Palawan, Philippines, in Seismic expression of structural styles”, a picture and work atlas, *AAPG Studies in Geology 15*, v. 3, p. 4.2-18 to 4.2-24, 1983.

Sakic, P., H. Piété, V. Ballu, J.-Y. Royer, H. Kopp, D. Lange, F. Petersen, M. S. Özeren, S. Ergintav, L. Geli, P. Henry, and A. Deschamps, “No significant steady state surface creep along the North Anatolian Fault offshore Istanbul: Results of 6 months of seafloor acoustic ranging", *Geophysical Research Letters*, 43 (13), 6817–6825, https://doi.org/10.1002/2016GL069600, 2016.

Sato, T., J. Kasahara, T. Taymaz, M. Ito, A. Kamimura, T. Hayakawa, and O. Tan, "A study of microearthquake seismicity and focal mechanisms within the Sea of Marmara (NW Turkey) using ocean bottom seismometers (OBSs)", *Tectonophysics*, 391, 303– 314, doi:10.1016/j.tecto.2004.07.018, 2004.

Schmittbuhl, J., H. Karabulut, O. Lengliné, M. Bouchon, "Seismicity distribution and locking depth along the Main Marmara Fault, Turkey", *Geochem. Geophys. Geosyst*., 17, 954–965, doi:10.1002/2015GC006120, 2015.

Seeber, L., O. Emre, M. H. Cormier, C. C. Sorlien, C. M. G. McHugh, A. Polonia, N. Ozer, and N. Cagatay "Uplift and subsidence from oblique slip: the Ganos-Marmara bend of the North Anatolian Transform, Western Turkey", *Tectonophysics*, 391, 239–258, 2004.

Seeber, L., M. H. Cormier, C. McHugh, O. Emre, A. Polonia, and C. Sorlien, "Rapid subsidence and sedimentation from oblique slip near a bend on the North Anatolian transform fault in the Marmara Sea, Turkey", *Geology*, 34(11), 933-936, 2006.

Seeber, L., C. Sorlien, M. Steckler, and M. H. Cormier, "Continental transform basins: Why are they asymmetric?" *Eos, Transactions American Geophysical Union*, 91(4), 29-30, 2010.

Shamir, G., M.D. Zoback, and C.A. Barton, "In site stress orientation near the San Andreas fault; Preliminary results to 2.1 km depth from the Cajon Pass scientific drill hole, California", *Geophys. Res. Lett*., 15, 989-992, 1988.

Shen Zheng- Kang, M. Wang, Y. Zeng, and F. Wang, "Optimal Interpolation of Spatially Discretized Geodetic Data", *Bulletin of the Seismological Society of America*, 105(4):2117, 2015.

Siyako, M., T. Tanış, F. Şaroğlu, “Marmara Denizi aktif fay geometrisi”, *TÜBİTAK Bilim Tek. Derg.*, 388, 66-71, 2000.

Smith, A.D., T. Taymaz, F.Y. Oktay, H. Yüce, B. Alpar, H. Başaran, J.A. Jackson, S. Kara, M. Şimşek, “High-resolution seismic profiling in the Sea of Marmara (northwest Turkey): late Quaternary sedimentation and sea-level changes”, *Geol. Soc. Am. Bull.*, 107, 923-936, 1995.

Stein, S., and M. Wysession, *An Introduction to Sesimology, Earthquakes, and Earth Structure*, Blackwell Publishing, Malden, Mass, 2003.

Sylvester, A. G., and R. R. Smith, “Tectonic transpression and basement-controlled deformation in San Andreas fauh zone, Salton trough, California”, *AAPG Bulletin*, v. 60, p. 2081-2102, 1976.

Şengör, A. M. C., N. Görür, F. Şaroğlu, “Strike-slip faulting and related basin formation in zones of tectonic escape: Turkey as a case study. In: Biddle, K.T., Christie-Blick, N. (Eds.), Strike-slip Faulting and Basin Formation, *Soc. Econ. Paleontol. Mineral. Spec. Publ.*, 37, 227-264. 1985.

Şengör, A. M. C., and A. A. Barka, “Evolution of escape-related strike-slipsystems: Implication for distributions of collisional orogens (abstract)”, *Proc. Int. Geol. Congr*,.,29, 232, 1992.

Şengör, A. M. C., O. Tüysüz, C. İmren, M. Sakinç, H. Eyidoğan, N. Görür, X. Le Pichon, and C. Rangin, “The North Anatolian Fault: A new look,” *Annu. Rev. Earth Planet. Sci*. 33, 37–112, 2005.

Şengör, A. C., C. Grall, C. İmren, X. Le Pichon, N. Görür, P. Henry, H. Karabulut, and M. Siyako, “The geometry of the North Anatolian transform fault in the Sea of Marmara and its temporal evolution: implications for the development of intracontinental transform faults”, *Canadian Journal of Earth Sciences*, 51(3), 222-242, 2014.

Rod, E., “Strike-slip faults of northern Venezuela”, *AAPG Bulletin*, v. 40, p. 457-476, 1956.

Takahashi, N., S. Shimizu, T. Maekawa, D. Kalafat, A. Pinar, S. Citak, Y. Kaneda, “OBS development for long term observation in the Marmara Sea, NW Turkey”, *Paper presented at 2015 Annual Meeting. EGU, Vienna*, 2015.

Tatar, O., J. D. A. Piper, R. G. Park, and H. Gürsoy, “Paleomagnetic study of block rotations in the Niksar overlap region of the North Anatolian FaultZone, central Turkey”, *Tectonophysics*, 244, 251–266, 1995.

Tary, J. B., L. Geli, P. Henry, B. Natalin, L. Gasperini, M. Comoglu, N. Cagatay, T. Bardainne, “Sea-bottom observations from the western escarpment of the Sea of Marmara”, *Bull. Seismol. Soc. Am*., 101, 2, doi:10.1785/012000014, 2011.

Tüysüz, O., A.A. Barka, E. Yiğitbaş, “Geology of the saros graben: its implications on the evolution of the North Anatolian Fault in the Ganos-Saros region, NW Turkey”, *Tectonophysics*, 293, 105–126, 1998.

Utsu, T., *Seismology, Second ed*., Kyoritsu Publication, Tokyo (in Japanese), 310 pp., 1984.

Vannucci, G., P. Gasperini, “A database of revised fault plane solutions for Italy and surrounding regions”, *Computers & Geosciences*, 29, 903-909, 2003.

Ward, S.N., “A multidisciplinary approach to seismic hazard in Southern California”, *Bull. Seis. Soc. Am*., 84, 1293-1309, 1994.

Ward, S.N., “On the consistency of earthquake moment rates, geological fault data, andspace geodetic strain: the United Statesa”, *Geophysical Journal International*., 134, 172-186, 1998.

Wells, D. L., and K. J. Coppersmith, “New empirical relationships among magnitude, rupture length, rupture width, rupture area, and surface displacement”, *Bulletin of the seismological Society of America*, 84(4), 974-1002, 1994.

Wilson, J. T., “A new class of faults and their bearing on continental drift”, *Nature*, 207:343–347, 1965.

Wong, H. K., T. Lüdmann, A. Ulug, N. Görür, “The Sea of Marmara: a plate boundary sea in an escape tectonic regime”, *Tectonophysics*, 244:231–250, 1995.

Yaltırak, C., M. Sakınç, F.Y. Oktay, “Kinematics and evolution of the northern segment of the North Anatolian Fault Zone (Ganos Fault) in the area between Marmara and Gulf of Saroz”, Tatar, O., Kavak, K.S., Özden, S. (Eds.), *Tektonik Araştırma Grubu 3. Toplantısı, ATAG-3, Proceedings*, 77–89. in Turkish with English abstract, 2000.

Yaltırak, C., “Tectonic evolution of the Marmara Sea and its surroundings”, *Marine Geology*, 190(1-2), 493-529, 2002.

Yamamoto, Y., N. Takahashi, S. Citak, D. Kalafat, A. Pinar, C. Gurbuz and Y. Kaneda, “Offshore seismicity in the western Marmara Sea, Turkey, revealed by ocean bottom observation”, *Earth, Planets and Space*, 67:147, DOI: 10.1186/s40623-015-0325-9, 2015.

Yamamoto, Y., N. Takahashi, A. Pinar, D. Kalafat, S. Citak, M. Comoglu, R. Polat, and Y. Kaneda, “Geometry and segmentation of the North Anatolian Fault beneath the Marmara Sea, Turkey, deduced from long-term ocean bottom seismographic observations”, *J. Geophys. Res. Solid Earth*, 122, 2069–2084, doi:10.1002/2016JB013608, 2017.

Yamamoto, Y., D. Kalafat, A. Pinar, N. Takahashi, Z. Coskun, R. Polat, Y. Kaneda, and H. Ozener, “Fault geometry beneath the western and Central Marmara Sea, Turkey, based on ocean bottom seismographic observations: Implications for future large earthquakes”, *Tectonophysics*, 791, 228568, 2020.

Zoback, M .D., and J.H. Healy, "In site stress measurement to 3.5 km depth in the Cajon Pass scientific research borehole; Implications for the mechanics of crustal faulting", *J . Geophys. Res*., 97, 5039-5057, 1992.

Zoback, M.D. et al., "New evidence on the state of the San Andreas fault system", *Science,* 238, 1105-1111, 1987.

APPENDIX: CMT SOLUTIONS OF SELECTED EARTHQUAKES

The CMT inversion results of selected earthquakes out of 99 are given below as examples. In the figures, the beachball at the upper left corner represents the focal mechanism diagram for the event, the source parameters and variance reduction are shown at the right of the focal mechanism, the synthetics (upper) and observed (lower) seismograms for three components at each station showing the ratio between synthetic and observed ratio, the variance reduction versus depth plot are given at the bottom of the figure.

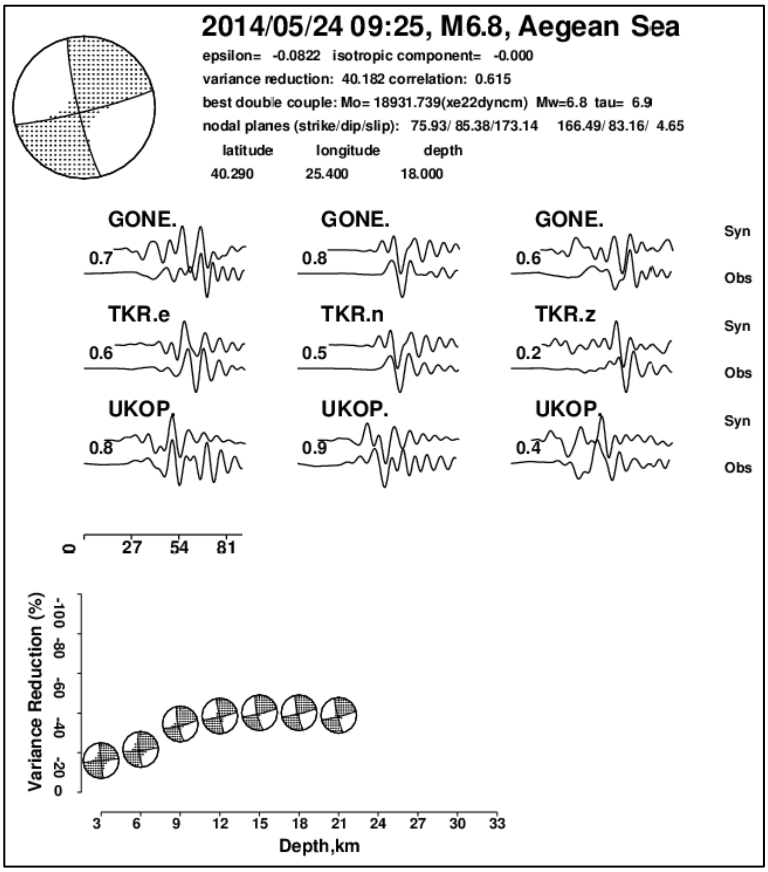

Figure 1. The moment tensor inversion result for the 24/05/2014 earthquake (Mw=6.8). The stations used to retreive the source parameters are all accelerometers, since all the broadband records in Marmara region were clipped during this event.

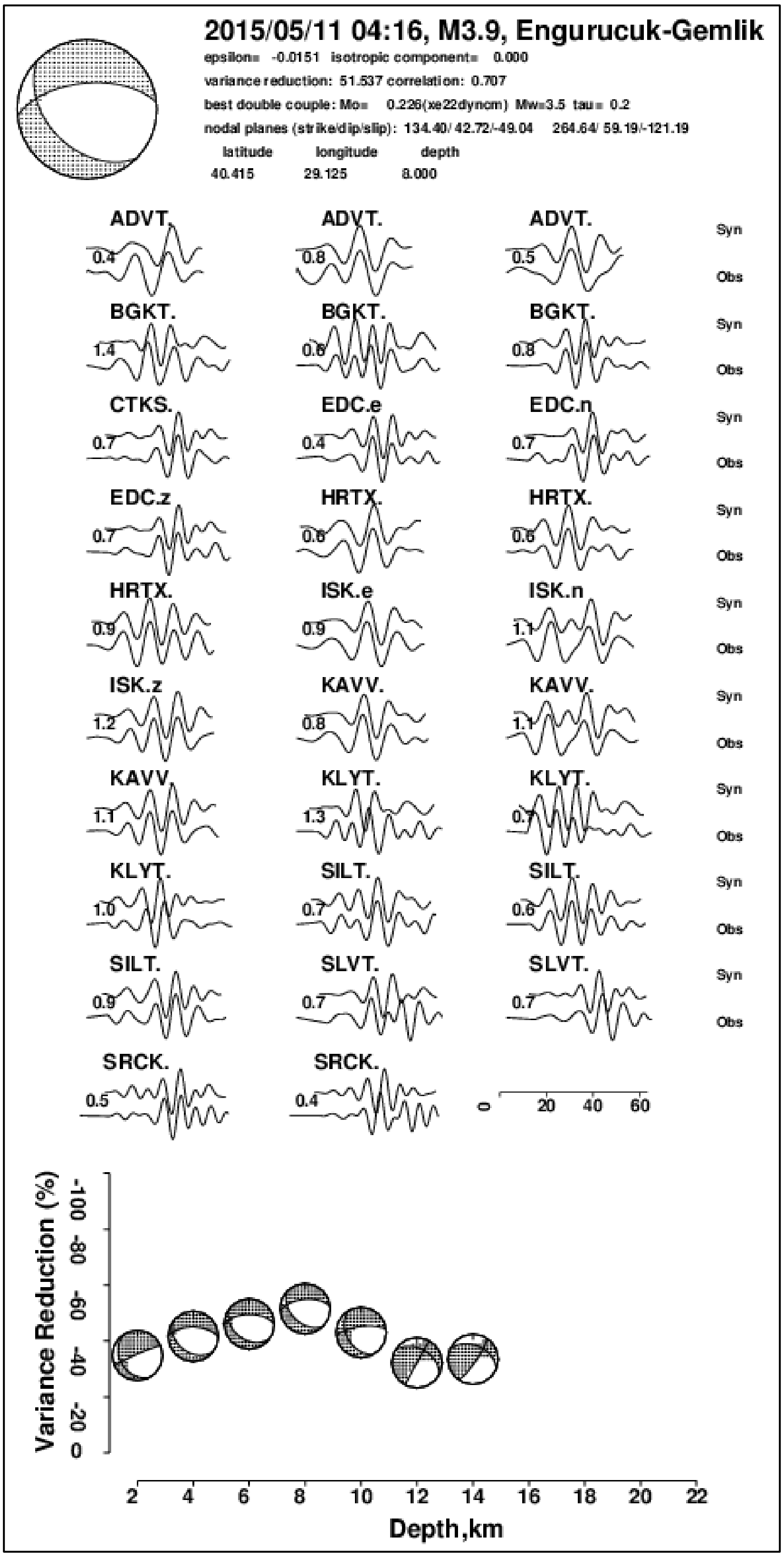

Figure 2. The moment tensor inversion result for the 11/05/2015 earthquake (Mw=3.5).

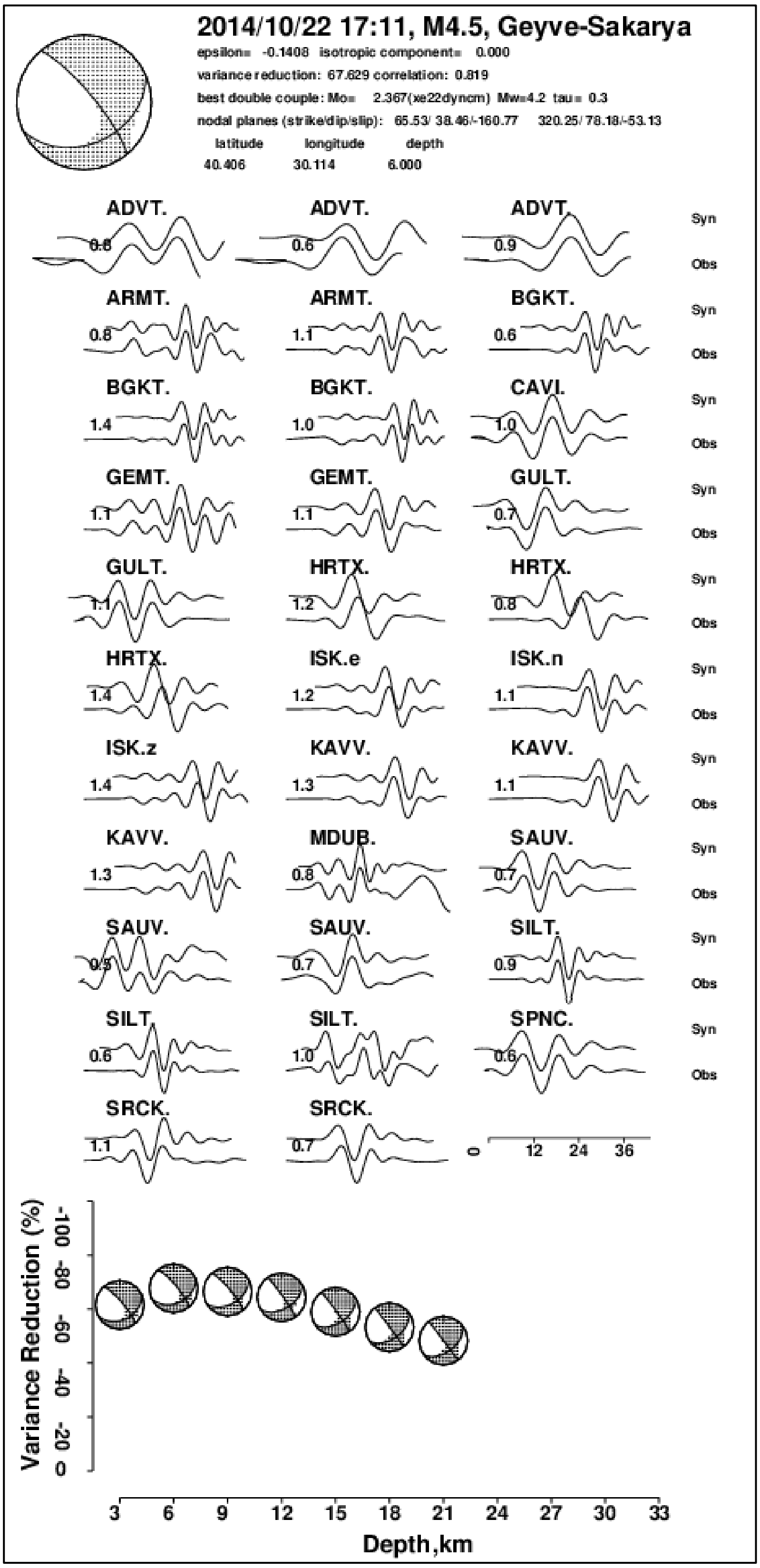

Figure 3. The moment tensor inversion result for the 22/10/2014 earthquake (Mw=4.2).

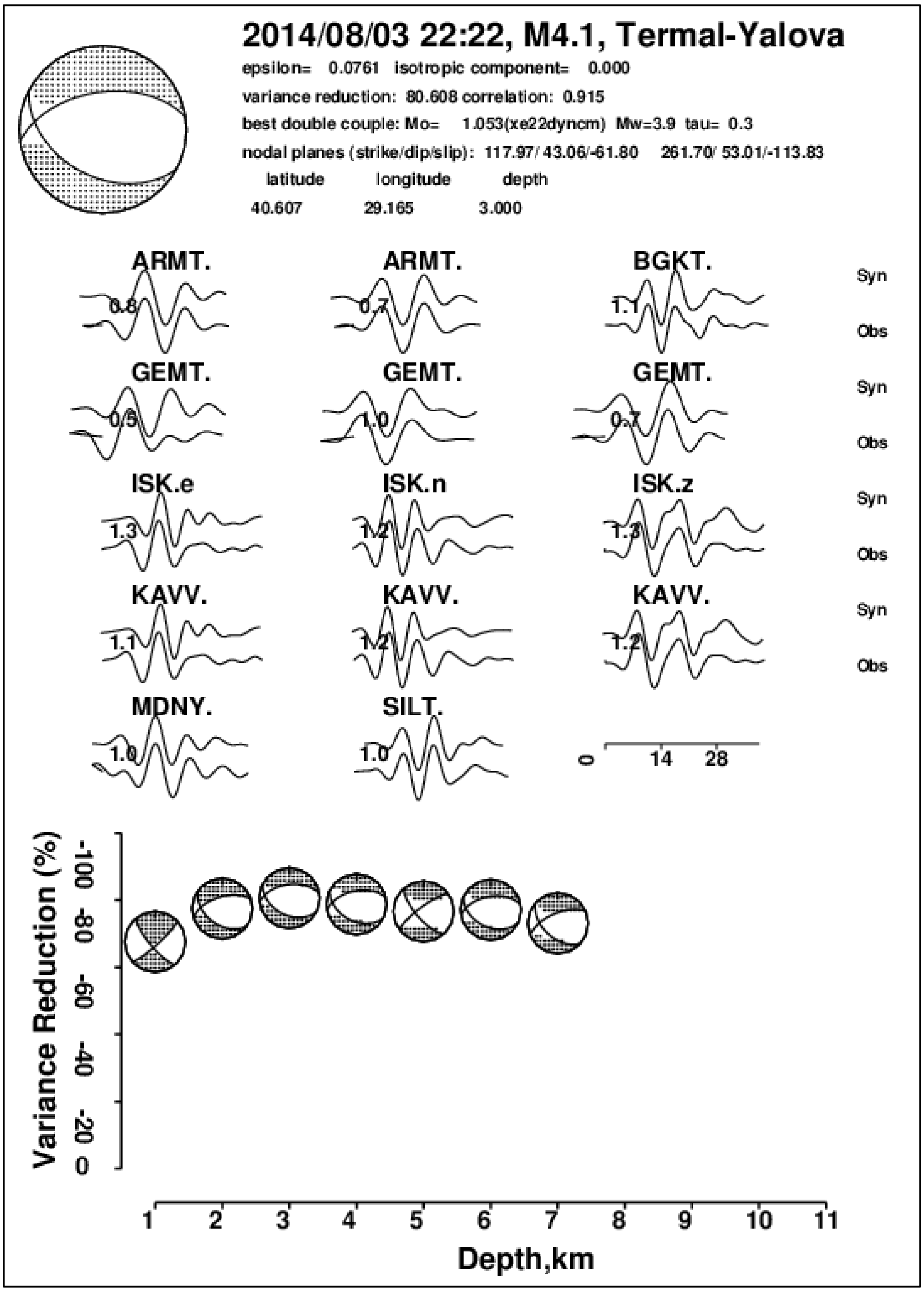

Figure 4. The moment tensor inversion result for the 03/08/2014 earthquake (Mw=3.9).

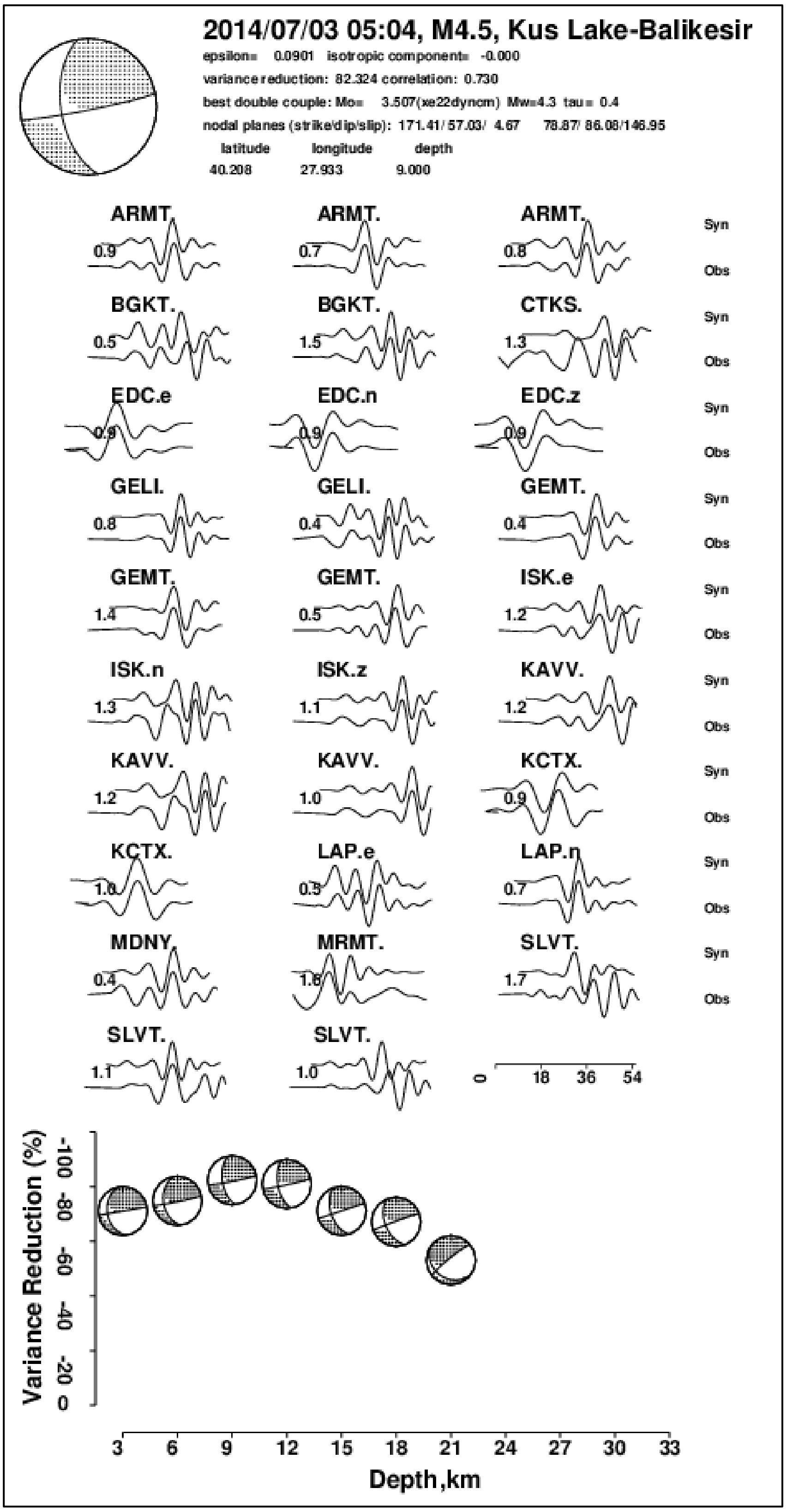

Figure 5. The moment tensor inversion result for the 03/07/2014 earthquake (Mw=4.3).

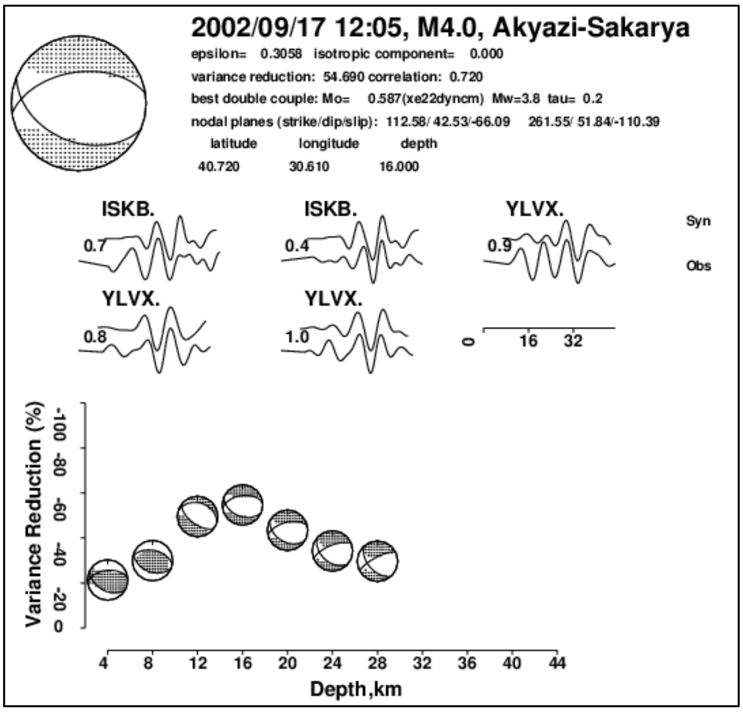

Figure 6. The moment tensor inversion result for the 17/09/2002 earthquake (Mw=3.8).

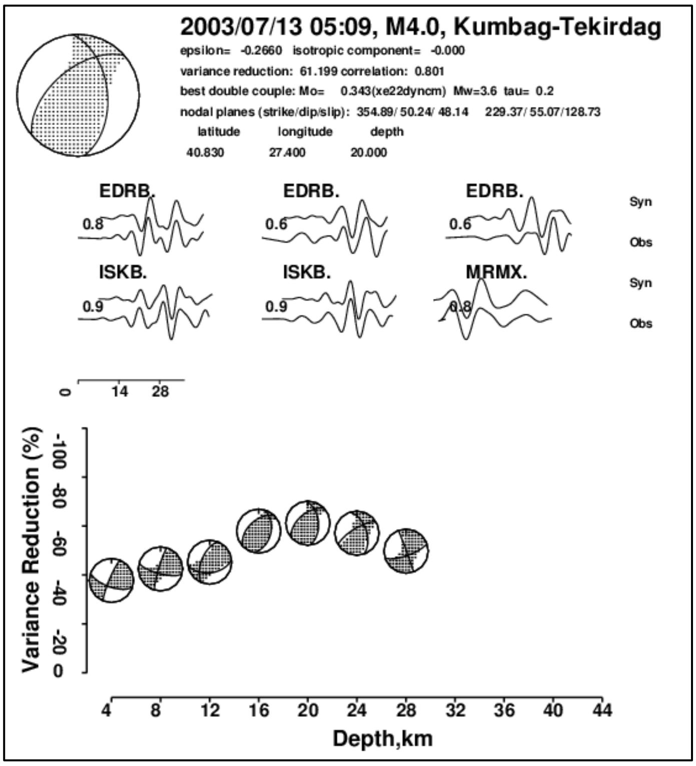

Figure 7. The moment tensor inversion result for the 13/07/2003 earthquake (Mw=3.6).

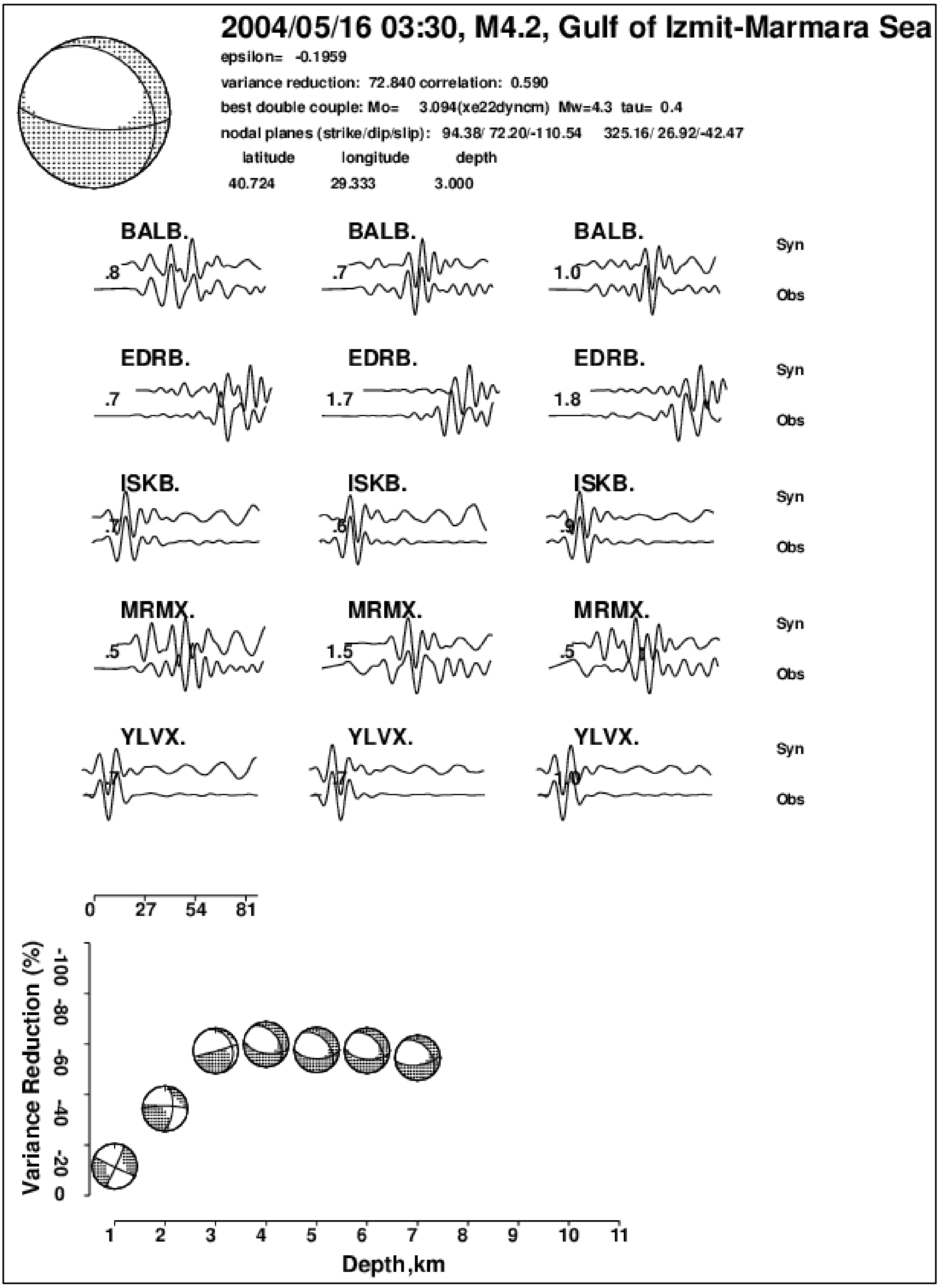

Figure 8. The moment tensor inversion result for the 16/05/2004 earthquake (Mw=4.3).

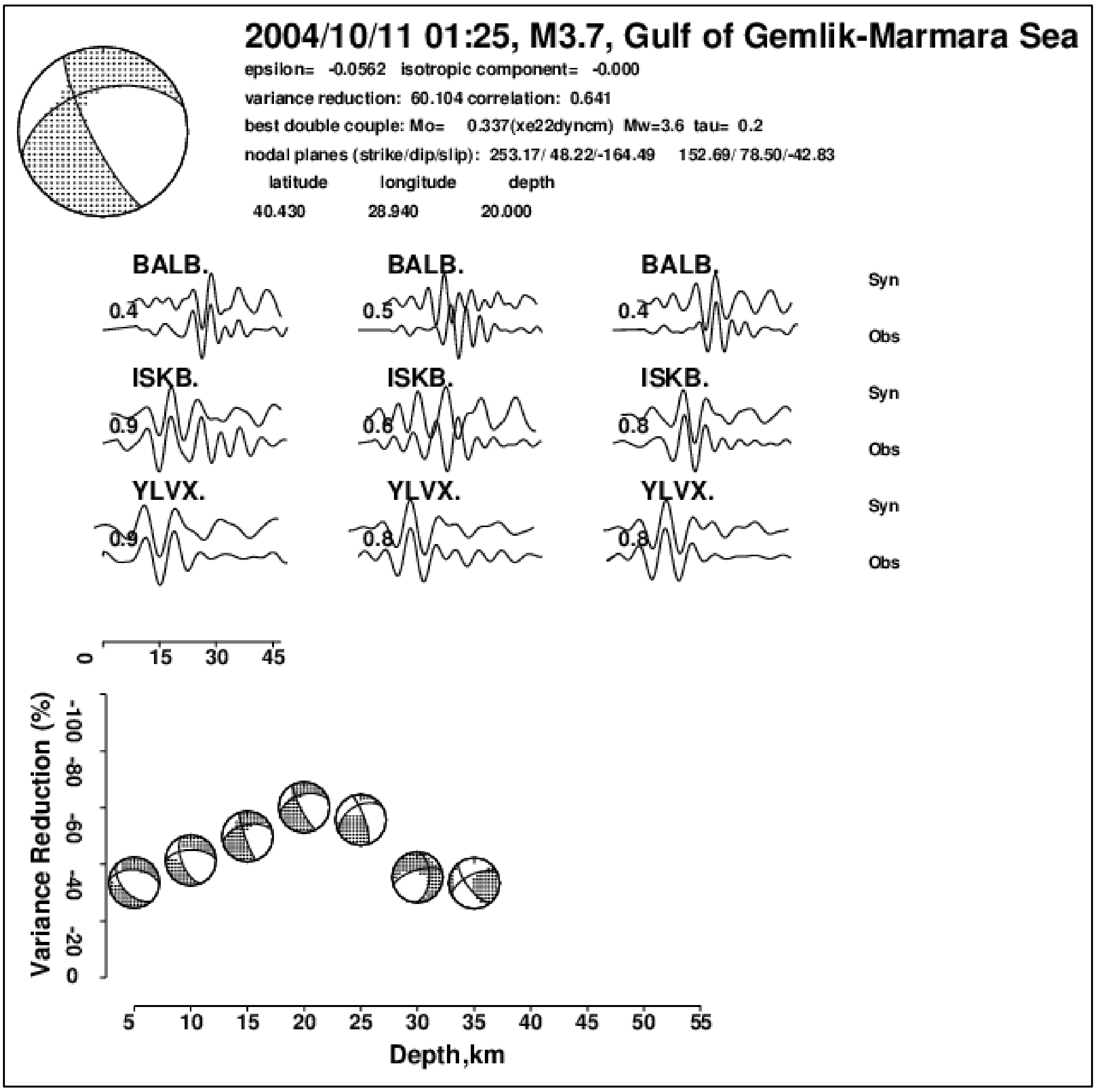

Figure 9. The moment tensor inversion result for the 11/10/2004 earthquake (Mw=3.6).

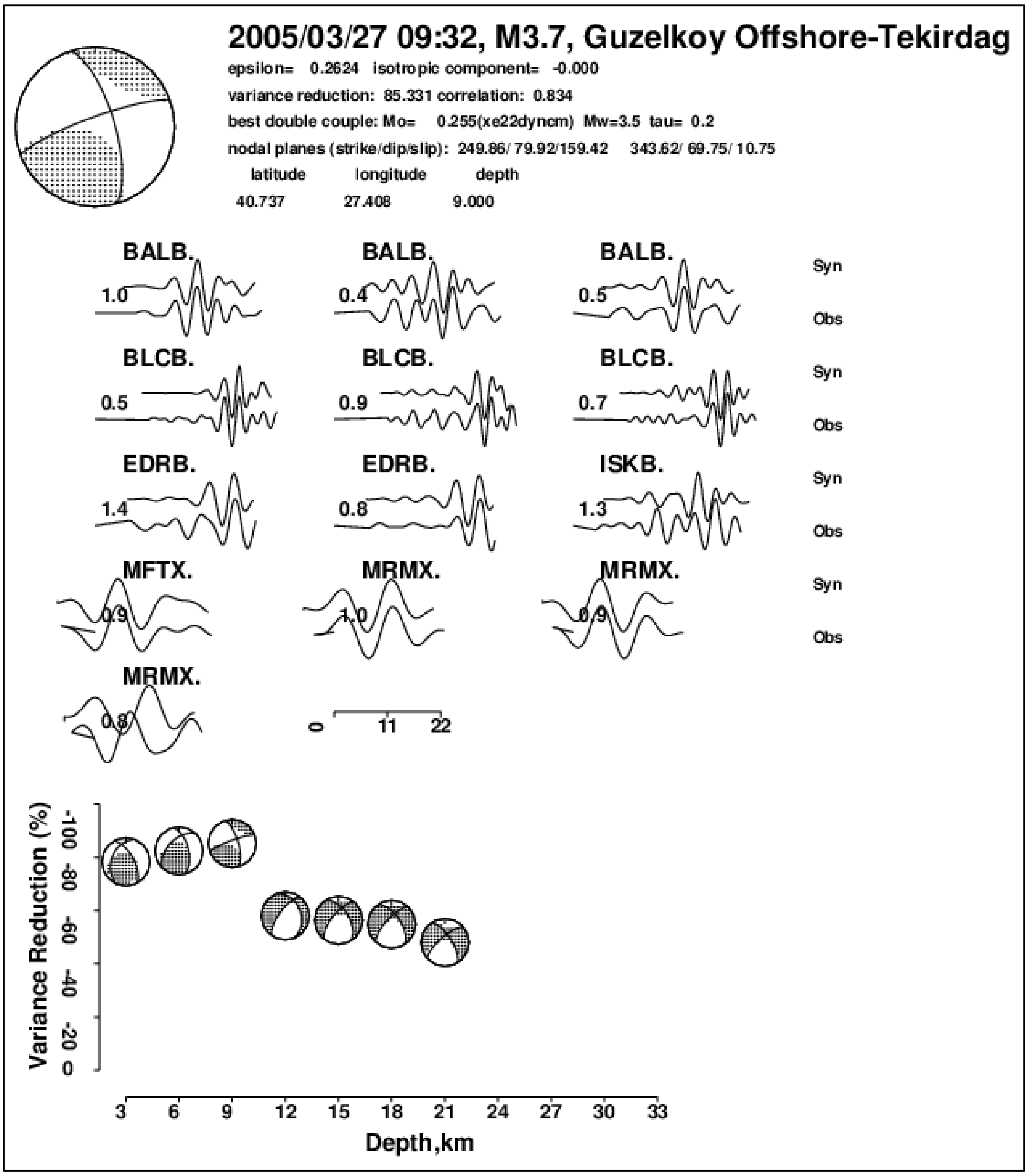

Figure 10. The moment tensor inversion result for the 27/03/2005 earthquake (Mw=3.5).

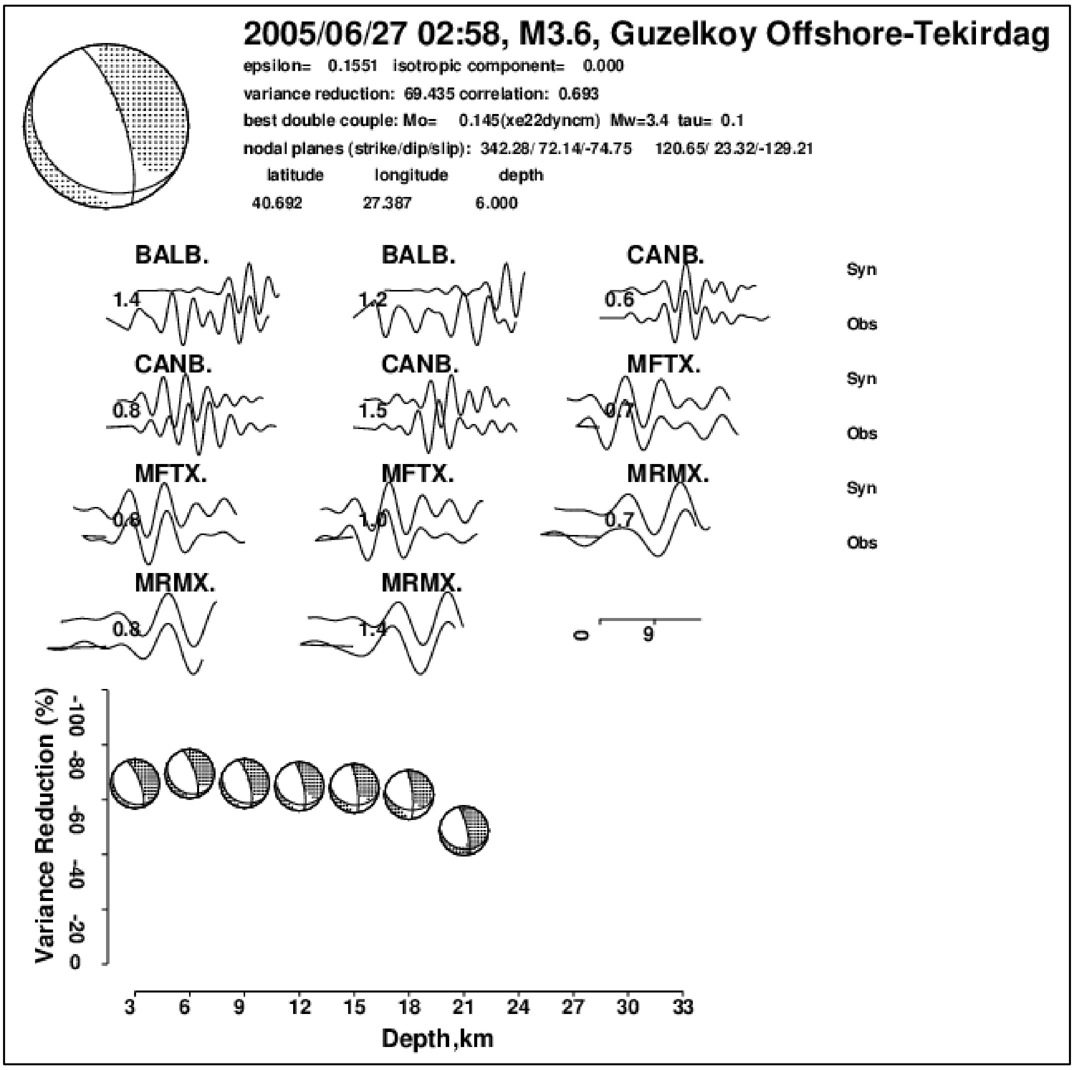

Figure 11. The moment tensor inversion result for the 27/06/2005 earthquake (Mw=3.4).

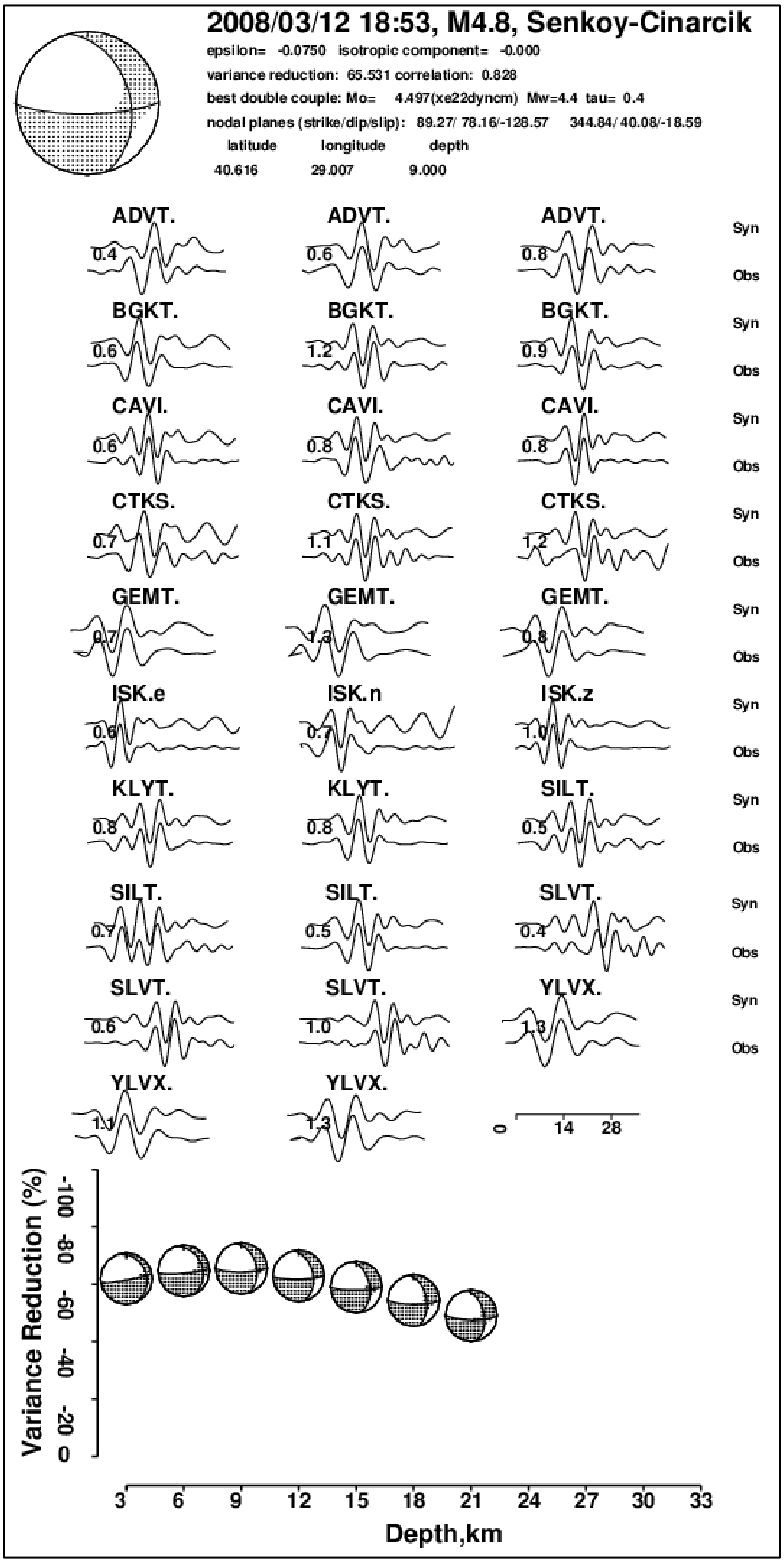

Figure 12. The moment tensor inversion result for the 12/03/2008 earthquake (Mw=4.4).

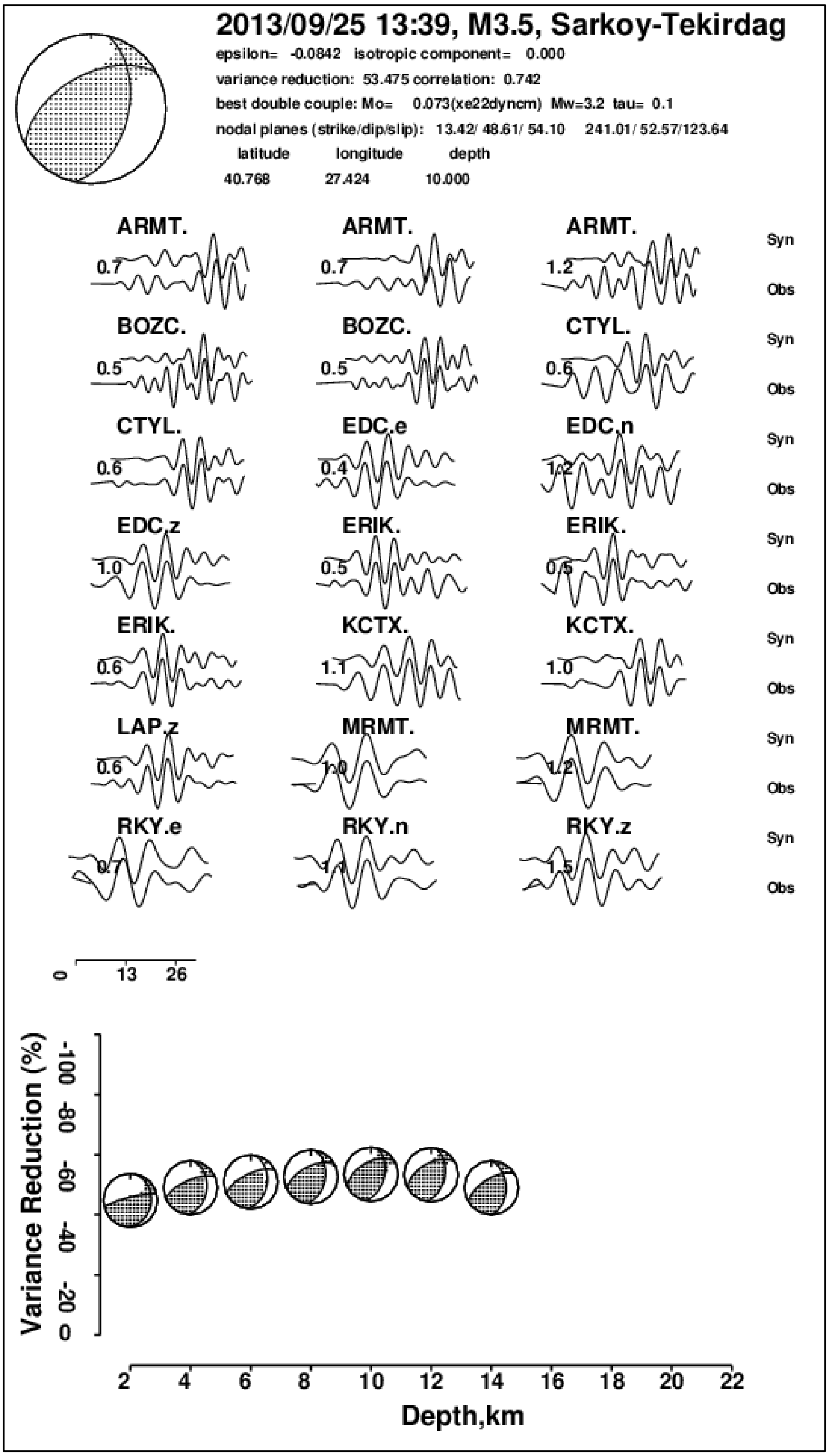

Figure 13. The moment tensor inversion result for the 25/09/2013 earthquake (Mw=3.2).

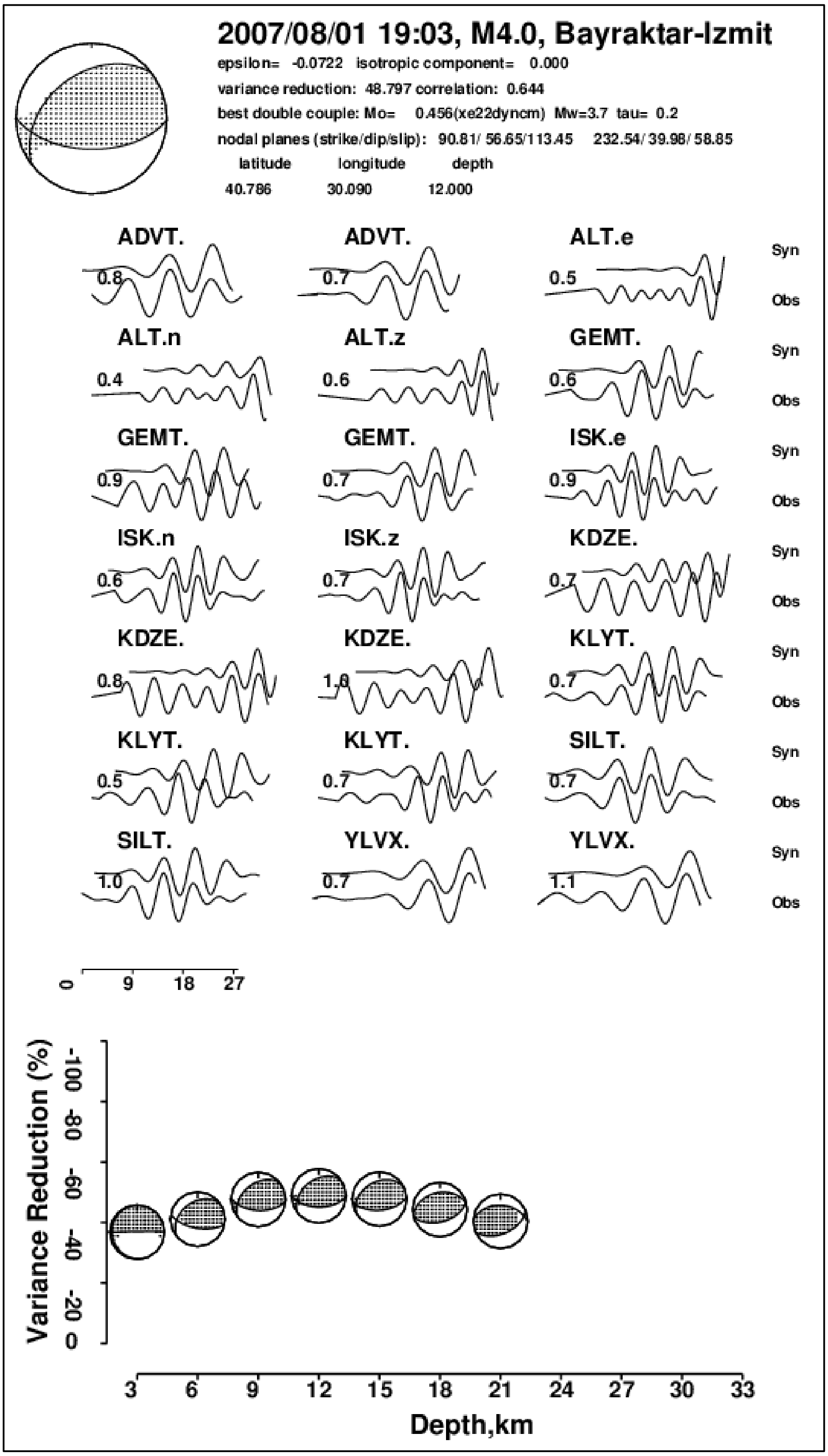

Figure 14. The moment tensor inversion result for the 01/08/2007 earthquake (Mw=3.7).

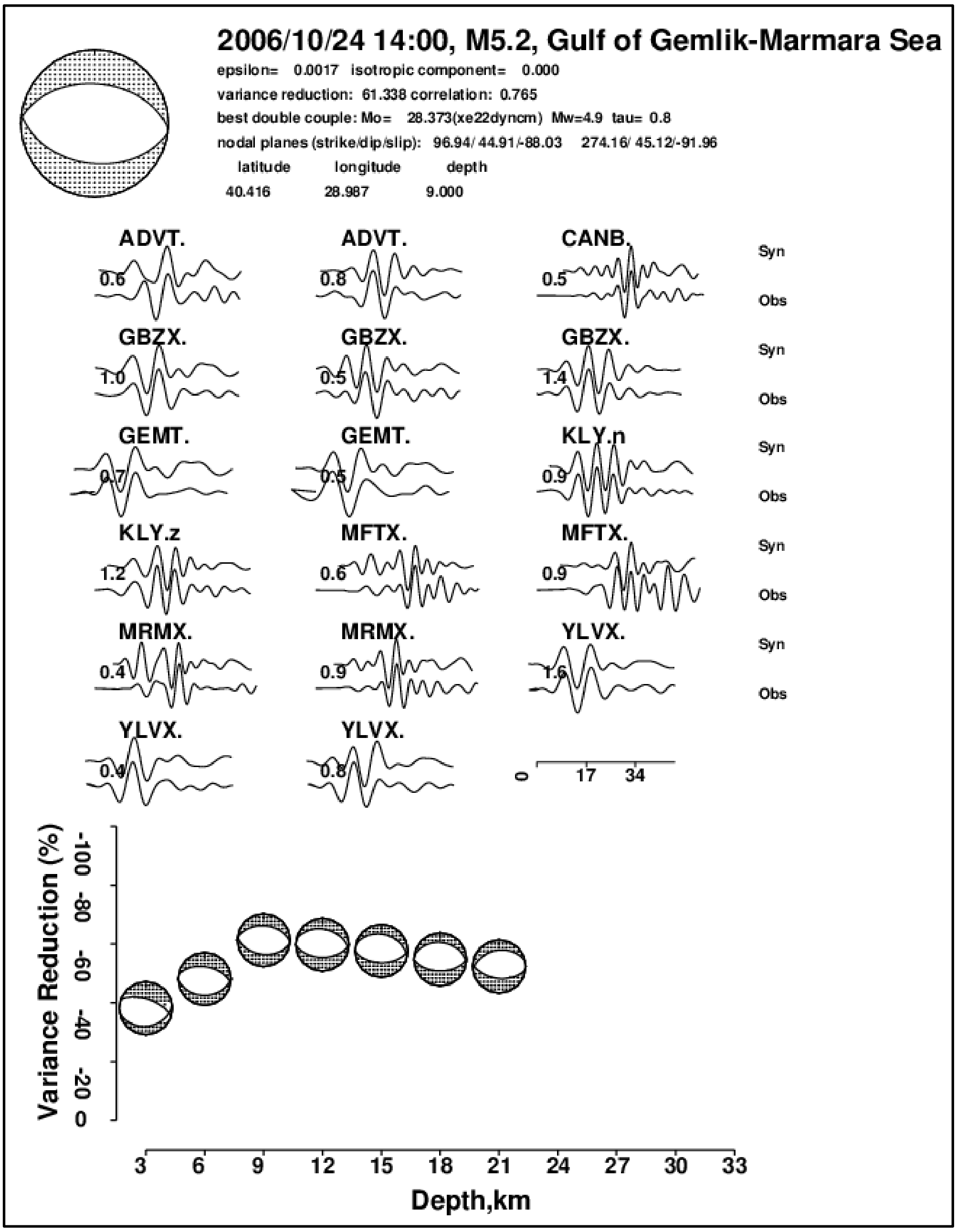

Figure 15. The moment tensor inversion result for the 24/10/2006 earthquake (Mw=4.9).